

Integrated Electrochemical Solar Energy Harvesting and Storage Devices

by

Mohammad Ali Mahmoudzadeh Ahmadi Nejad

M.A.Sc., The University of British Columbia, 2009

B.Sc., Sharif University of Technology, 2006

A THESIS SUBMITTED IN PARTIAL FULFILLMENT
OF THE REQUIREMENTS FOR THE DEGREE OF

Doctor of Philosophy

in

THE FACULTY OF GRADUATE AND POSTDOCTORAL STUDIES

(Electrical and Computer Engineering)

The University of British Columbia

(Vancouver)

April 2015

© Mohammad Ali Mahmoudzadeh Ahmadi Nejad, 2015

Abstract

Large scale storage of electricity is a vital requirement for the realization of a carbon-neutral electricity grid. This thesis provides a study of integrated solar energy conversion and storage systems in order to increase the efficiency and reduce the utilization cost of solar energy. The efficient performance of photogalvanic cells relies on high dye solubility and selective electrodes with fast electron transfer kinetics. A new configuration is proposed for photogalvanic cells that removes these impractical requirements. Instead of illuminating the device through the electrode a new vertical configuration is employed with light coming between the two electrodes. This way, the light absorption and hence electron generation is spread through the depth of the device which can be adjusted according to the concentration of the dyes to absorb all the incoming photons even with low solubility dyes and slow electrode kinetics. The proposed configuration is mathematically studied and a numerical model is built for detailed analysis that gives practical guidelines for working towards device parameters with high power conversion efficiency. The analysis suggests that upon the realization of highly selective electrodes and an improved dye/mediator couple, an efficiency higher than 13% should be achievable from the new configuration compared to 3.7% at best using the conventional approach. Storage however in this system will be challenging due to the characteristic recombination times of dyes and mediators in the same phase.

For significant and long-lived storage we designed and demonstrated an integrated solar-battery structure based on two relatively well established technologies of the redox flow battery and the dye-sensitized solar cell. The cell consists of a sensitized electrode in a redox flow bat-

tery structure. The design enables independent scaling of power and energy rating of the system thus it is applicable for large scale storage purposes. An areal energy capacity of $52 \mu\text{Whcm}^{-2}$, charge capacity of 1.2mAh L^{-1} , energy efficiency of 78% and almost perfect Coulombic efficiency are observed for the integrated cell. These values show a 35 times increase in charge capacity and 13 times improvement in areal energy density compared to similar devices.

Preface

The author is the main researcher of all of the work presented in this dissertation. All the work is conducted in UBC Molecular Mechatronics Lab under the supervision of Prof. John D.W. Madden.

Chapter 2. A version of this material has been published in journal of *Electrochimica Acta* (Mahmoudzadeh M.A., Madden J.D., "A Vertical Architecture for Increasing Photogalvanic Solar Cell Efficiency: Theory and Modeling", *Electrochimica Acta*, Volume 143, 2014, Pages 98-105). All the theoretical analysis and numerical modeling are performed by the author with supervision of Prof. John D.W. Madden.

Chapter 3. The author was the lead investigator on the concept formation with contributions from Prof. John D.W. Madden and Dr. Ashwin R. Usagaocar. All the design, fabrication and characterization are the original, independent work of the author. The author also received valuable feedback on this work from Professor Gordon Wallace at the University of Wollongong, who met approximately monthly with him by phone.

The concept and supporting theory of the work in Appendix B is provided by the author. The experimental work and data analysis are performed by Dr. Ashwin R. Usagaocar and Dr. Lisheng Wang. Prof Dan Bizotto provided valuable feedback on the electrochemical analysis. The results are presented in the Electrochemical Society (ECS) Meeting. (Usgaocar A.R., Wang L., Mahmoudzadeh M.A., Mirvakili S.M., Slota-Newson J.E., Madden J.D., Beatty J.T., Takshi A. "Semiconductors as Selective Electrodes for Bio-Photovoltaic Cells", Meet Abstr. MA2013-01(4), 282., 2013)

Table of Contents

Abstract	ii
Preface	iv
Table of Contents	v
List of Tables	viii
List of Figures	ix
List of Abbreviations	xi
Acknowledgments	xiii
Dedication	xiv
1 Introduction	1
1.1 Energy Storage and Renewables	1
1.2 Photogalvanic Cells	6
1.3 Redox Flow Batteries	11
1.4 Dye Sensitized Solar Cells	13
1.5 Research Objective	17
1.6 Thesis Overview	17

2	A Vertical Architecture for Increasing Photogalvanic Solar Cell Efficiency: Theory and Modeling	19
2.1	Introduction	20
2.2	Analysis of the Conventional Photogalvanic Cell	21
2.3	Analytical Analysis of the Vertical Photogalvanic Cell	24
2.3.1	Geometry Optimization	28
2.3.2	Load Optimization	30
2.3.3	Estimation of Maximum Efficiency	30
2.4	Simulation of the Photogalvanic Cell	31
2.4.1	Equation Set	32
2.4.2	Results	34
2.5	Conclusion	38
3	Solar Redox Battery	41
3.1	Introduction	41
3.2	Design	46
3.3	Results	54
3.4	Conclusion	60
3.5	Experimental	62
4	Conclusions and Future Work	66
4.1	Conclusions	66
4.2	Contributions	68
4.3	Future Work	69
	Bibliography	73
A	Publications Not Included in the Thesis	81

B Semiconductors as Selective Electrodes	83
B.1 Introduction	83
B.2 The Gerischer Model	84
B.3 Experimental Measurement of the Selectivity	87
C Solar Redox Battery Cost Analysis	90

List of Tables

Table 1.1	A list of commercial RFB energy storage facilities.	13
Table 2.1	Characteristic lengths of photogalvanic devices.	23
Table 2.2	Albery’s recipe for the optimal cell	24
Table 2.3	Device parameters and performance of electrode illuminated photogalvanic devices. Efficiencies, η , are as computed using COMSOL.	35
Table 2.4	Device parameters and performance of vertical photogalvanic devices. Efficiencies, η , are as computed using COMSOL.	38
Table 3.1	Polarization of Ni foam electrodes in polysulfide electrolyte.	52
Table 3.2	List of materials for an efficient, high energy density solar redox battery. . .	53
Table 3.3	Performance comparison of DSSC-based solar batteries.	60
Table B.1	Standard heterogeneous rate constants of redox couples on FTO.	89
Table C.1	Comparison of energy conversion and storage costs for combined and separated systems.	91

List of Figures

Figure 1.1	Human Development Index (HDI) vs. per capita electricity consumption.	2
Figure 1.2	Charactristic discharge time of energy storage technologies.	4
Figure 1.3	Schematic of a biological solar cell with dissolved reaction centers.	7
Figure 1.4	(a)Open circuit voltage and (b)short circuit current of the reaction center -based solar cell.	7
Figure 1.5	Schematic of a traditional photogalvanic cell.	8
Figure 1.6	Schematic of the vertical photogalvanic cell.	10
Figure 1.7	Schematic of a RFB system.	12
Figure 1.8	Energy diagram and the working principle of a dye sensitized solar cell.	15
Figure 1.9	Schematic of the solar redox battery.	16
Figure 2.1	Schematic of a vertical photogalvanic cell.	22
Figure 2.2	Load independent efficiency vs $l\sqrt{\frac{k_r[M^+]}{D}}$ in a vertical PGC.	29
Figure 2.3	The variation of ψ with respect to u_0 in a vertical PGC.	31
Figure 2.4	Simulation results of the target vertical PGC.	37
Figure 2.5	Effect of device length and electrode selectivity on cell efficiency for both top and side illuminated cells.	40
Figure 3.1	Schematic of different approaches towards the integrated solar battery.	44
Figure 3.2	Schematic of a solar chargeable redox battery.	47
Figure 3.3	Energy diagram of Redox couples for the solar redox battery.	49

Figure 3.4	Tafel plots of several electrodes towards the polysulfide redox couples. . . .	50
Figure 3.5	Tafel plots of several electrodes towards the polysulfide redox couples. . . .	51
Figure 3.6	Charge/discharge characteristics of the iodide-polysulfide redox battery. . .	55
Figure 3.7	(a)Complete discharge and (b) energy efficiency of the iodide-polysulfide redox battery.	56
Figure 3.8	IV characteristics and short circuit current of DSSC using the solar-battery electrolyte.	58
Figure 3.9	Solar redox battery sandwich structure	59
Figure 3.10	(a)Photocharge/ Discharge of the solar redox battery. (b)Energy efficiency during charge/discharge cycles.	61
Figure 3.11	Color change of sodium sulfide as it changes from colorless Na_2S (a) to dark red Na_2S_4 (e).	63
Figure 3.12	SEM images of the nickel foam before (a), and after treatment with acid and polysulfide (b).	63
Figure 3.13	Schematic and the image of the H-type cell used for the battery test.	65
Figure 3.14	Images of the (a) light source and (b) the potentiostat setup.	65
Figure 4.1	Utilization if thermal convection for electrolyte circulation in solar redox batteries.	71
Figure B.1	Distribution of energy states in semiconductor (left) and metal (right)-electrolyte interface. The overlap between filled and empty states on two sides determines the reaction rate.	84
Figure B.2	Cyclic voltammetry of (a) methyl viologen (b) ferri/ferrocyanide and (c) ferric/ferrous on FTO electrode. (d) Sampled current voltammetry data measured at 12 s after the voltage application.	88

List of Abbreviations

A-CAES Adiabatic Compressed Air Energy Storage

ACN Acetonitrile

CAES Compressed Air Energy Storage

DI Deionized

DSSC Dye Sensitized Solar Cell

EES Electrochemical Energy Storage

FES Flywheel Energy Storage

HDI Human Development Index

FTO Fluorine Doped Tin Oxide

HOMO Highest Occupied Molecular Orbital

LUMO Lowest Unoccupied Molecular Orbital

PB-A Lead Acid

PGC Photogalvanic Cell

PHES Pumped Hydro Energy Storage

PS Polysulfide

PTG Power to Gas

RFB Redox Flow Battery

SRB Solar Redox Battery

TES Thermal Energy Storage

THF Tetrahydrofuran

VPGC Vertical Photogalvanic Cell

Acknowledgments

First and foremost I offer my sincerest gratitude to my supervisor, Prof. John Madden, who has supported me throughout my research with his excellent knowledge and unmatched patience and has given me with an exceptional atmosphere for doing research. I was extremely fortunate to have him as my mentor and advisor and cannot imagine any better person for that role.

I would like to express my gratitude to the members of my thesis committee who guided me with their thoughtful feedback.

I am also grateful to Prof. Curtis Berlinguette and Dr. Phil Schauer, for being generous with their time and knowledge. I thank Prof. Jeff Young for kindly giving me access to his laboratory.

I gratefully acknowledge the financial support of this work through Discovery and Strategic Grants from the Natural Sciences and Engineering Research Council (NSERC) of Canada and The Peter Wall Institute for Advanced Studies at UBC.

I want to thank all my current and previous co-researchers during this work: Dr. Ashwin Usgaocar, Dr. Arash Takshi, Dr. Rafael Saer, Dr. Jo Slota-Newson, Daniel Jun, Seyed Mohammad Mirvakili and Bahar Iranpour for helping me advance this work and also thank all my colleagues at the Molecular Mechatronics lab for creating such a productive work place.

Most importantly, I want to express my gratitude to my wife, my parents and my three sisters, whose love, guidance and sacrifice are always beyond what could be asked.

To my grandparents, whose love follows me to Vancouver and drives me forward in life.

Chapter 1

Introduction

A goal of this thesis is to investigate and propose means of harvesting solar energy, and to find a solution to one of the challenges hindering the widespread use of clean energy - the storage problem. We first set the stage by estimating the energy demand in the near future and discuss the importance of energy storage. Then the candidate storage technologies will be examined and the advantages of an electrochemical energy storage solution will be discussed. By the end of this chapter, the proposed electrochemical harvesting and storage methods and the component technologies will be presented. The motivation for combining a redox flow cell with a dye-sensitized solar cell is discussed, as is the justification of its feasibility for solving the solar energy storage challenge.

1.1 Energy Storage and Renewables

Annual global electrical energy demand surpassed 20×10^3 TWh in 2013 and is increasing at a rate of 3 % per year. The importance of electricity in today's life is clear. Figure 1.1 shows the human development index (HDI) for many countries with respect to their average electricity consumption. In general a higher HDI is observed as a result of higher electricity use. This graph can be used to estimate the global electrical energy demand in the following decades. Neglecting the off-trend values for countries such as Iceland and Norway and the hope for a

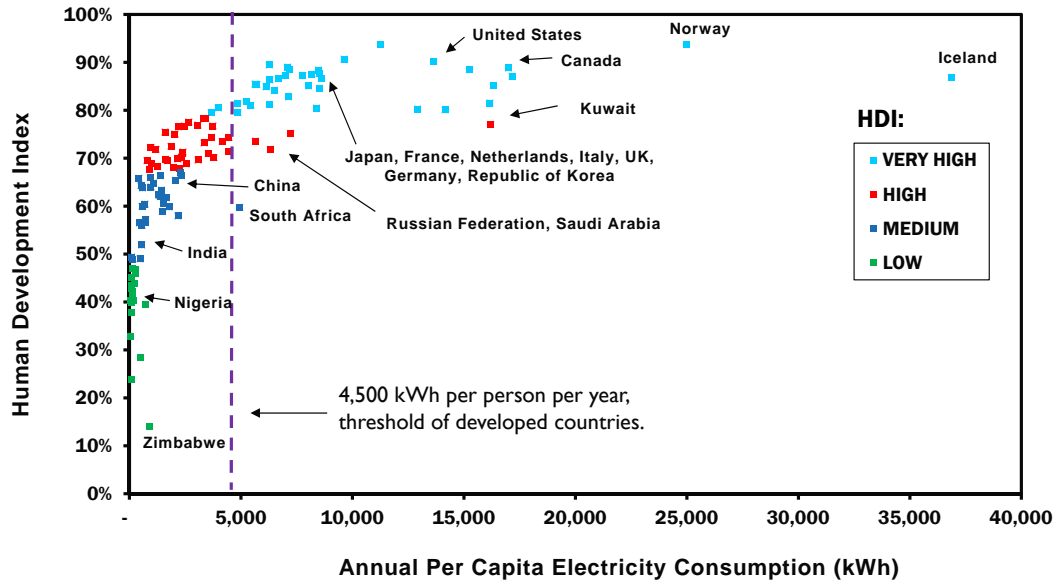


Figure 1.1: Human Development Index (HDI) vs. per capita electricity consumption. Data from United Nations Human Development Reports [2] and International Energy Agency [3]. 4500 kWh/year/person is the onset of acceptable standard of living.

more efficient use of electrical energy in future, one can expect that a minimum consumption of 4500 kWh/year/person is required for an acceptable standard of living for the 9 billion population in 2050. Therefore, we will need a global electricity supply of 40×10^3 TWh/year by mid century, twice the amount of today's global generation. More detailed analysis by the International Energy Agency estimates the mid century electricity demand to be in the range from 33 to 42×10^3 TWh/year depending on energy policy choices made between now and then [1].

The realization of this amount of electrical energy with current resources will lead to an increase of atmospheric greenhouse gas concentrations to three times the current day value [4]. A perturbation on this scale has never been experienced on the planet and the outcome could severely endanger our ecosystem. Carbon-neutral energy sources are the logical method of choice. Nuclear, biomass, hydroelectric and wind power each has their own limitations that make them unattractive as the ultimate solution for energy generation. Nuclear power plants need very complicated site fabrication and given demand the installation rate needed to catch up

with the global demand is likely impossible. Biomass is not effective because of its low power conversion efficiency and its competition with the food supply. Hydroelectricity, although clean and inexpensive, is already utilized close to its maximum capacity and can not significantly contribute further to global electricity generation. Wind energy capacity can supply part of the upcoming demand but is not an adequate solution for the problem [5].

Solar energy is the only carbon-neutral source that can supply all the energy demand [5]. Variability during the daytime and intermittency as a result of atmospheric conditions are the major drawbacks of this energy source. An effective energy storage system is required for the global utilization of solar energy.

Our current electric grid does not have much storage capacity. To properly function, the grid has to always balance the energy supply and demand by tuning the power plant output. Otherwise it produces voltage fluctuations which are not acceptable, particularly for many industry users. Germany, with a storage capacity greater than 8% of its electrical generation capacity, has already run into grid instability problems as the share of renewables exceeded 20% [6]. A report from U.S. National Renewable Energy Laboratory (NREL) has calculated the maximum manageable share of renewables in a grid without storage to be 20% [7]. They conclude that at least 24 h of energy storage is required to balance an electricity grid with 80 % generation by variable sources.

Storage solutions should have suitable capacity and response time for the specific application. Power quality applications require only sub-second storage capacity while energy management applications such as load leveling and peak shaving need discharge times of 1 to 20 hours. Centralized grid connected storage typically has a 100 MW power rating while a distributed system can consist of several 100 kW power plants. Figure 1.2 shows the discharge time and capacity of several energy storage technologies that have been tested for addressing this issue. From the technologies listed in that figure, pumped hydro is the only mature technology and accounts for 99% of total available storage capacity. It stores energy in the form of potential energy by using the electrical energy surplus to pump water into a reservoir of

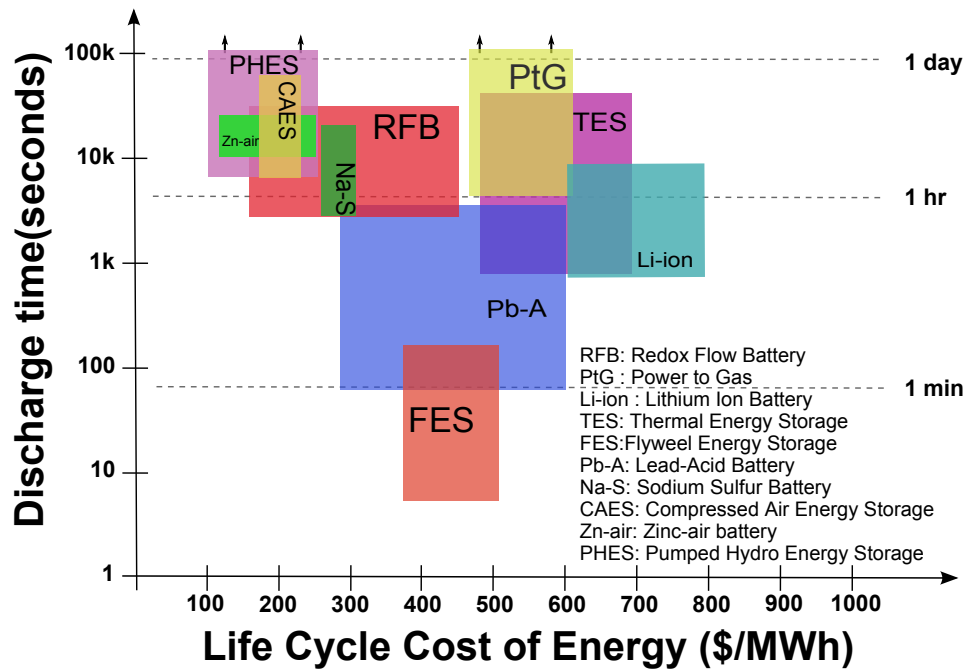


Figure 1.2: Characteristic discharge time of energy storage technologies. The horizontal axis represents the typical life cycle cost (Levelized Cost of Energy) estimates of each technology. The values are adopted from [8]. The upward arrows indicate that PHEs and PtG have the potential for longer (even seasonal) energy storage.

higher elevation. However, its wide use relies heavily on geographical availability of a water reservoir in an elevated location and therefore it can not be a global solution. Furthermore, it is not suitable for distribution storage solutions, which is what is needed in today's Germany for example, since hydroelectric's overall efficiency drops to $\sim 50\%$ for micro (≤ 100 kW) applications. Additionally, their slow response time makes them impractical for solar energy storage where seconds to minutes response time is required for unpredictable sunlight variations during the daytime.

The second largely utilized method is compressed air energy storage (CAES) which has a global capacity of 440 MW [9]. Off-peak low cost electricity is used to compress air, which is later released to recover the energy. Temperature changes during compression and expansion are the main loss mechanisms, limiting widespread use. Research towards an adiabatic CAES

system is currently trying to bring cyclic efficiency of CAES up to 50 % but those systems are not economically attractive yet [10].

Another approach for energy storage is flywheel energy storage (FES), which is very attractive because of its scalability, fast response time and high round-trip efficiency. However, its efficiency drops significantly at low discharge rates. Also, FES systems have high self-discharge rates, which make them suitable only for short term storage.

The limited energy storage capacity of supercapacitors together with their high power and cycle life make them ideal only as short term power quality applications - before the main energy supply kicks in [9].

Power to gas (PtG) energy storage systems use electrolysis of water to produce hydrogen which is then stored in the form of H_2 gas or is converted to synthetic methane after reaction with CO_2 . Having storage capacity in the scale of terawatt-hours makes this method even suitable for seasonal storage applications. The fact that the current natural gas network can be employed for storage and transfer of synthetic gas together with its high energy density and insignificant long-term storage loss make this a very attractive energy storage solution. In fact, a 6 MW (industrial scale) power-to-methane pilot plant is already demonstrated in Germany [11]. Despite these technical advantages, this technology still suffers from relatively low efficiency and very high cost. Therefore, significant reduction in the cost and improvement in performance are required before it can compete with conventional energy storage techniques [12].

Electrochemical energy storage (EES) in several forms such as lithium-ion, sodium-sulfur and lead-acid batteries are studied for renewable energy storage. The typical main drawback of all types is high capital cost even for the cheapest technology (lead acid battery) [13].

Integration of energy conversion and storage is one method to reduce the cost of solar energy systems. A method for achieving such integration is described in this thesis. Such devices could significantly reduce the fabrication and installation cost of utilization of the renewables. Further improvement is expected from reduction in cost of balance of system and energy con-

version losses. In the next sections, we present the electrochemical energy storage systems that promise the possibility of such integration. The main body of this thesis describes the modification and enhancement of the devices that are now discussed.

1.2 Photogalvanic Cells ¹

Combined solar cell- battery behavior is observed in prior work on biological solar cells in which the author took part. In that work, reaction center (RC) proteins from photosynthetic bacteria were used as light absorbers in a variety of solar cell architectures [14–16]. In one configuration, RCs are dissolved in a solvent together with two redox couples. After the light absorption, a positive and a negative charge pair are separated in the RC, as indicated in the figure by the red and blue dots. The role of the redox couples, called mediators m_1 and m_2 , is to react with the RC and extract the charges before their recombination. The charges are then transferred to the electrodes and external circuitry. A schematic of this device is depicted in Figure 1.3. Despite the perfect quantum efficiency of RCs and their long self-discharge time [17], less than 0.1% photo-conversion efficiency is observed from this device. However, it showed an unexpected charge storage behavior. Figure 1.4 shows the response of a dissolved RC-based solar cell after cell illumination ends. The open circuit voltage of the cell drops on a time scale of hours which reflects a slow self discharge and the photocurrent of the cell vanishes after tens of minutes. This apparent storage over minutes to hours is the motivation behind studying similar configurations in this work as the starting point for solar-battery integration. The dissolved RC solar cell belongs to a family of solar cells called photogalvanic cells (PGCs). The first architecture investigated is a modified photogalvanic cell, described in Chapter 2.

Photogalvanic cells consist of an electrolyte containing a dissolved light absorbing dye and a redox system called a mediator in contact with two charge extraction electrodes. In addition to solar energy conversion, PGCs naturally inherit energy storage capability from their

¹This section is part of a publication in a peer-reviewed journal (Reused with permission from "Mohammad Ali Mahmoudzadeh, John D.W. Madden, 'A Vertical Architecture for Increasing Photogalvanic Solar Cell Efficiency: Theory and Modeling', *Electrochimica Acta*, Volume 143, 2014, Pages 98-105", Copyright 2014, Elsevier Ltd.).

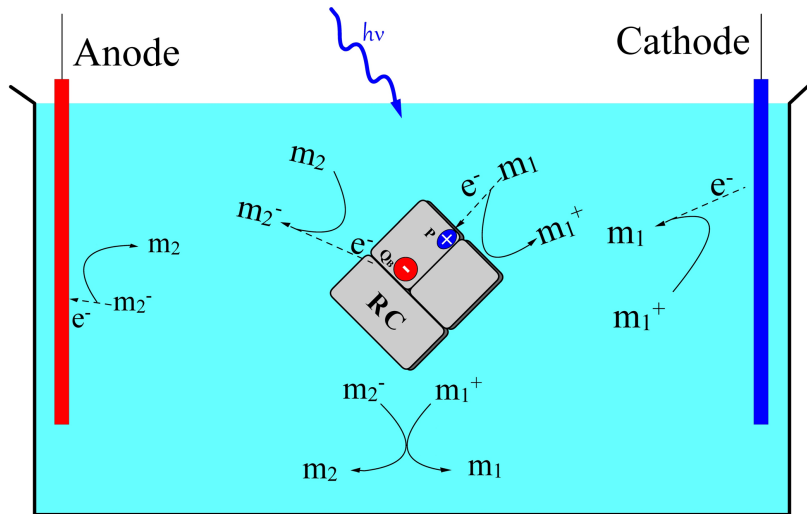


Figure 1.3: Schematic of a biological solar cell with dissolved RCs. m_1 and m_2 are two redox mediators. After the light absorption and the photo-excitation of the RC, positive and negative charges are separated by the mediators and then transferred to the electrodes.

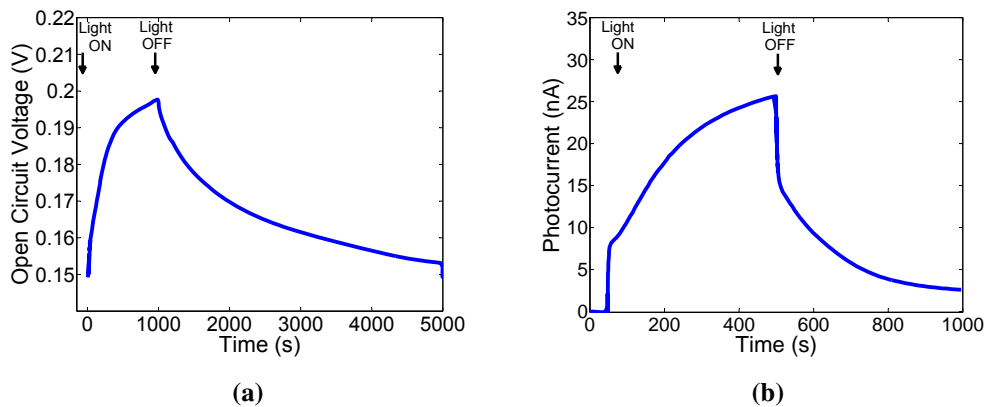


Figure 1.4: (a) Open circuit voltage and (b) short circuit current of the reaction center-based solar cell. The RC of the photosynthetic bacterium *Rhodobacter sphaeroides* is used at a $15 \mu\text{M}$ concentration in water. The mediators are 0.75 mM ferrocene and 0.75 mM methyl viologen in Tris-HCl buffer (pH 8). The light intensity is 2.8 mW cm^{-2} .

battery counterpart, galvanic cells. The power generation mechanism of photogalvanic cells is shown in Figure 1.5. It starts with the photo-excitation of the dye followed by dye-mediator reaction. The excited dye can be reduced or oxidized by the mediator depending on the dye

and mediator combination selected. The redox couple and the stabilized dye then can react on the electrodes to generate current. In this work, the classic process of a dye-electron donor will be explored. Chapter 2 explores the limits on power conversion efficiency, and a new cell geometry introduced to overcome shortcomings of the traditional cell.

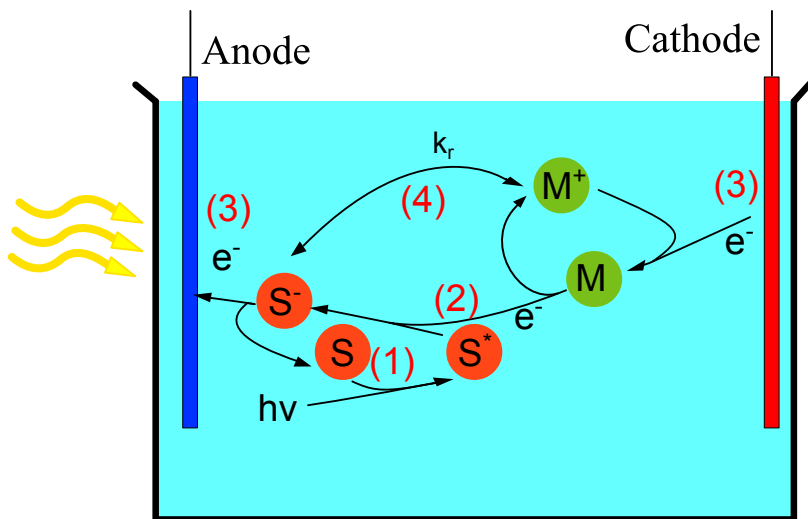


Figure 1.5: Schematic of a traditional photogalvanic cell. The work flow is (1) light absorption and dye excitation.(2) Quenching of the excited dye and production of reduced dye and oxidized mediator.(3) Each redox couple interacts with one electrode and produces a current. (4) The bulk recombination tends to push the cell back to the equilibrium with rate constant k_r .

In the photogalvanic cell, excitation occurs almost instantly after the absorption of a photon. The relaxation process happens at a rate of k_{Relax} and takes $10^{-12} \sim 10^{-9}s$ (reaction (1.1), in parentheses),



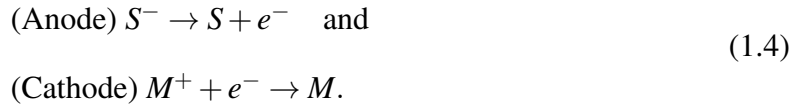
If the excited dye lives long enough to diffuse in the electrolyte and interact with a charge mediator, the excited dye will be quenched which results in two charged species;



where S , S^* and S^- are relaxed, excited and reduced states of the sensitizing dyes and M/M^+ is the mediating redox couple. Since the products are at high energy levels, they will recombine in the bulk with the rate constant of k_r which is the main loss mechanism of the cell,



In order to extract the absorbed energy, the products of reaction (1.2) need to diffuse to the electrodes before their recombination through reaction (1.3). It is also desired that each redox couple only interact with one of the electrodes in order to avoid electrode mediated recombination of the species *i.e.* electrodes should behave selectively towards the couples. In this case,



In the case of fast kinetics of these reactions, the electrode potentials will follow the potential of the redox couples, therefore, an open circuit potential difference of $\Delta E \approx |E_{S^-/S} - E_{M^+/M}|$ is expected from this cell. The analytical analysis of photogalvanic cells proposed by Albery and Archor [18] showed the possibility of high performance PGCs given certain conditions of device geometry and chemistry. To date the highest efficiency of a PGC is claimed by Bhimwal and Gangotri to be 1.62% with methyl orange as photosensitizer dye [19], which expresses how far these devices are from practical use. On the storage side, Genwa's group reported energy storage for up to 2 hrs from their devices [20, 21] while 1 hr storage was observed by Gangotri's [22]. Selective electrodes, fast electrode kinetics and high solubility of the dyes are the main unsatisfied properties needed to produce a good PGC. In Chapter 2 a change in the configuration of the PGC is proposed that eases some of the hard to achieve requirements. The proposed new structure is justified using analytical and numerical analysis.

Instead of illuminating the device through the electrode as was done in the previous work,

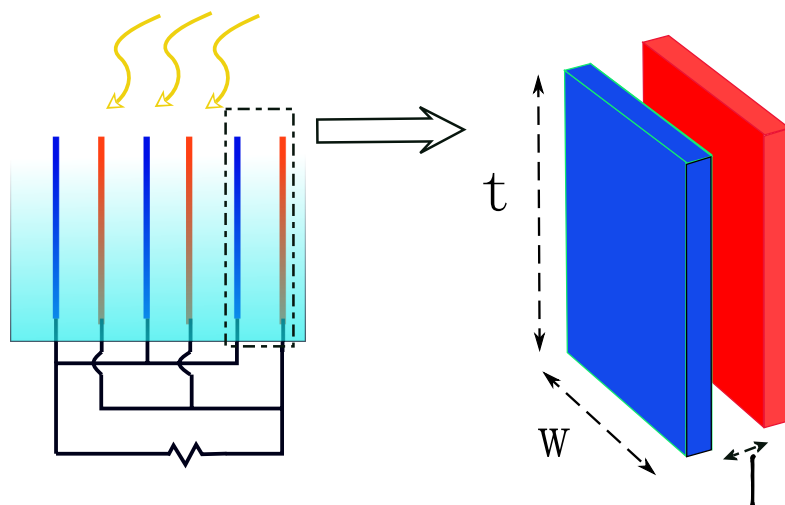


Figure 1.6: Schematic of the vertical photogalvanic cell. The left figure shows several aligned vertical cells to cover a large area. Each cell consists of two parallel electrodes, with small spacing, l . Each electrode should be selective to one of the redox couples.

a vertical alignment of PGCs is suggested so that the light comes in from the gap between the two electrodes as shown in Figure 1.6. This way, the light absorption and hence electron generation is spread through the depth of the device. A larger absorption length can be used. As a result smaller current densities are expected and fast electrode kinetics are no longer required. The depth can be adjusted according to the concentration of the dyes, and thus deeper cells enable low solubility dyes - that are often more appropriate in other respects - to be employed. Multiple devices stack next to each other to cover surfaces. The investigation of this structure is suggested due to more relaxed requirements and higher possible efficiency. However, there are some drawbacks to this approach, including the difficulty of achieving highly selective electrodes needed for efficient operation and the limited storage capability of this method. For significant and relatively long-lived storage another approach is investigated that marries two relatively well established technologies: the redox flow cell and the dye-sensitized solar cell.

1.3 Redox Flow Batteries

Redox flow batteries (RFBs) are electrochemical cells with active materials stored separately from the power conversion electrodes as shown in Figure 1.7. This segmentation results in an energy capacity independent of the power generator size, which gives more freedom with the selection of electrocatalyst and active materials. In conventional batteries, the electrodes simultaneously act as the energy storage and power conversion media. This aggregation eliminates any significant scale-up advantage. The dissolved redox electrochemistry additionally allows for higher tolerance to over-charge and over-discharge compared to conventional batteries. Under these conditions, the ratio of oxidized and reduced species in the electrolyte is modified to follow the applied overpotential, meanwhile, the flow mechanism prohibits heat accumulation, whereas in Li-ion batteries as an example, an overcharge results in an internal metal plating and rapid temperature elevation which make the battery unsafe and unstable. Increasing the size of reservoirs relative to the electrodes can lead the device to approach the theoretical capacity of its active material as the mass and volume of other parts becomes insignificant compared to that of active material. Because of the isolation of the two tanks, no self-discharge is expected from the RFBs.

Redox flow batteries have two half-cells, separated by a membrane. The active material that is stored separately in the form of an electrolyte, flows to these half-cells for charge and discharge. One half-cell consists of the electrode and part of electrolyte for the negative electrode reactions and the other for the positive reactions. It is standard to name the electrodes for their discharging behavior, therefore the negative electrode during discharge is called the anode and the positive electrode during discharge is named the cathode (although their reaction types are opposite during the charging). The electrolytes in contact with the anode and cathode electrodes are called negative and positive electrolytes respectively, according to the same convention. In order to have high power output and smooth flow of the electrolyte, a pair of porous electrodes is required to increase the electrodes' effective surface area and their permeability to the active materials.

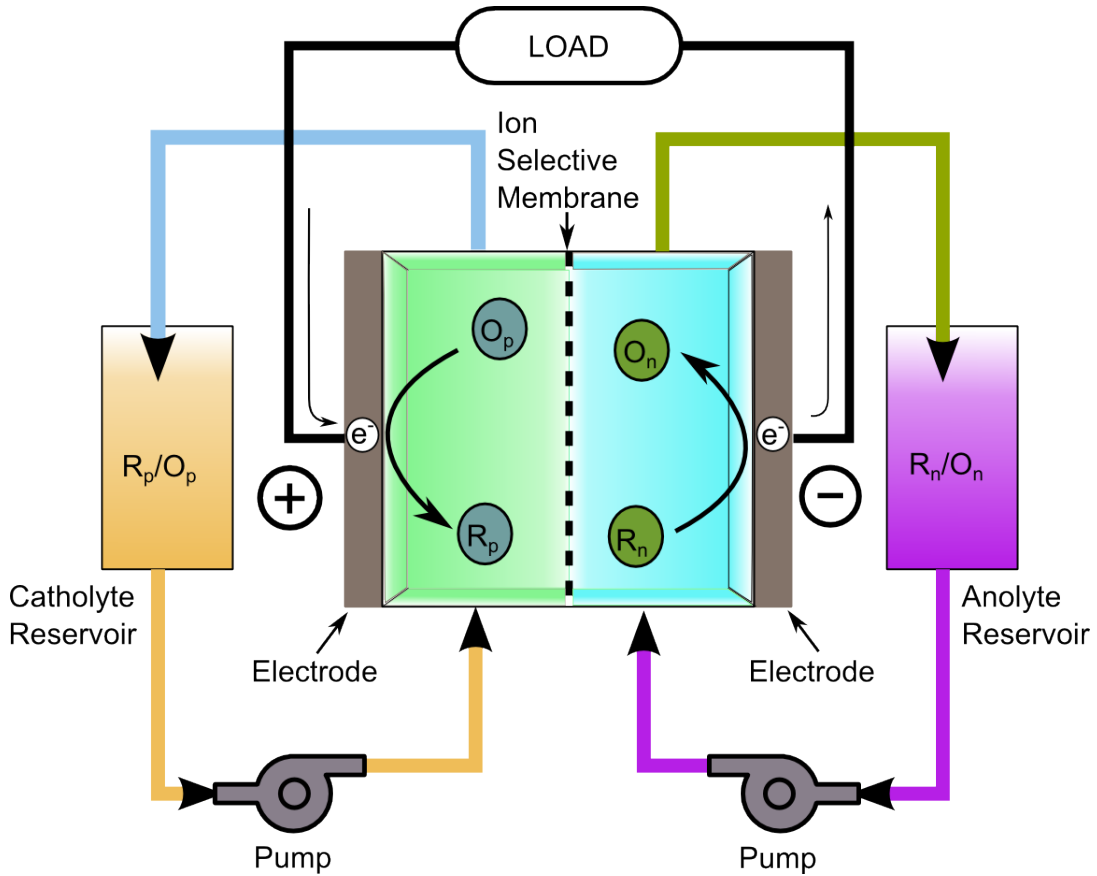
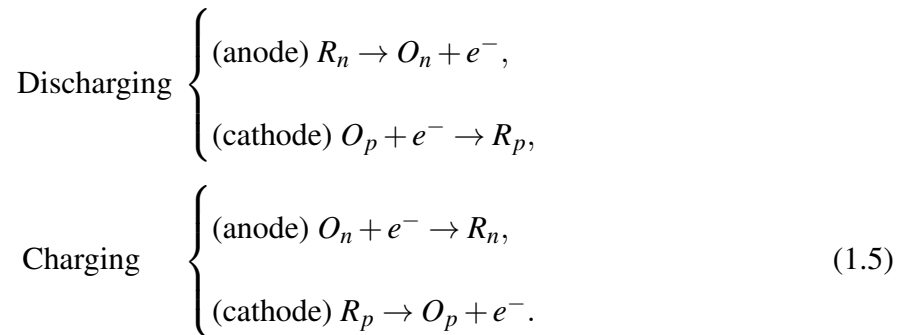


Figure 1.7: Schematic of a RFB system. Energy is stored in active species O_n/R_n and O_p/R_p which are the oxidized and reduces species of redox couples in negative and positive electrolytes respectively. The electrolytes are stored in external tanks and are fed to the cell during charge and discharge.



It can be seen in Figure 1.2 that the RFB has the highest discharge time among the battery energy storage technologies. Current RFB systems range from 10^2 to 10^8 Wh capacity -

the latter being one order of magnitude larger than large scale electrochemical energy storage systems [13]. Table 1.1 lists some of the commercial RFB energy storage plants across the globe. The RFB's capital cost is estimated to be less than 500 \$/kWh for an industrial scale

Table 1.1: A list of commercial RFB energy storage facilities.²There are also several smaller (sub-MWh) installations in Spain and Denmark.

Technology	Power rating	Storage capacity	country
Polysulfide-Bromide	15 MW	120 MWh	UK
All Vanadium	15 MW	60 MWh	Japan
All Vanadium	5 MW	10 MWh	China
All Vanadium	4 MW	6 MWh	Japan
All Vanadium	500 kW	2 MWh	Japan
All Vanadium	500 MW	2 MWh	US
Iron-Chromium	250 MW	1 MWh	US

1 MWh storage facility, which is less than the 800 \$/kWh minimum cost of Li-ion batteries in the same scale [23]. Further increase in size would emphasize the price gap even more. The average capital costs of RFBs and Li-ion batteries are estimated to be 300 \$/kWh and 540 \$/kWh respectively for grid-scale storage [12]. The cycle life of RFBs are shown to be larger than 13×10^3 cycles, double the value for the best Li-ion batteries. This give RFBs further price advantages in cost per cycle analysis [13].

An RFB structure is used in this work to build a solar-battery by integrating it with a solar cell. Such integration requires design compatibility and availability of the materials that satisfy the requirements of both devices. Dye sensitized solar cell technology is chosen to be paired with RFBs as it is a relatively efficient solar cell and employs a redox process that can be shared with the RFB system.

1.4 Dye Sensitized Solar Cells

Dye sensitized solar cells (DSSCs) have shown great potential for sunlight harvesting, with their low fabrication costs (4-10 years payback time), high efficiency even in low light condi-

²From US department of energy global energy database. (<http://www.energystorageexchange.org>)

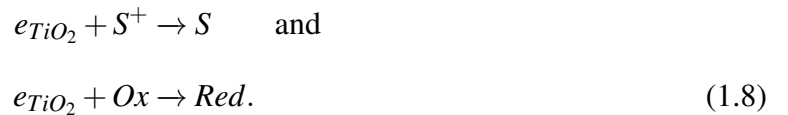
tions and environmentally compatible precursors [24]. In 1991, Gratzel *et al.* expanded the previous work on photocurrent generation from sensitized semiconductors in photo-electrochemical cells (PEC) [25] and suggested the structure of a solar cell loosely based on photosynthesis in nature [26]. DSSCs are made of a nanoporous wide band gap semiconducting electrode (e.g., TiO_2) which is coated with a monolayer of light absorbing dye molecules. This electrode is immersed in an electrolyte containing an energetically appropriate redox couple (Red/Ox) and a platinum counter electrode. Light absorption in the sensitizing dyes (S) results in an exciton (S^*) whose electron jumps rapidly to the semiconductor,



As depicted in Figure 1.8, the mediator then reduces the positively charged dye, reaction 1.7, making the dye ready to absorb another photon,



Charge recombination is an interfacial process in DSSCs. The high surface area of this device makes it critical to minimize energy waste through recombination. Separated electrons in the conduction band of TiO_2 might recombine with the positive side of dye or the oxidants,



Design restrictions should be applied to minimize these leakage currents. Reducing the resistance between the TiO_2 nanoparticles normally suppresses the first reaction and coulombic screening of photo-electrons by the surrounding electrolyte is used to limit the second loss mechanism [27].

The very limited life time of photo-excited electrons in TiO_2 before either flowing to the

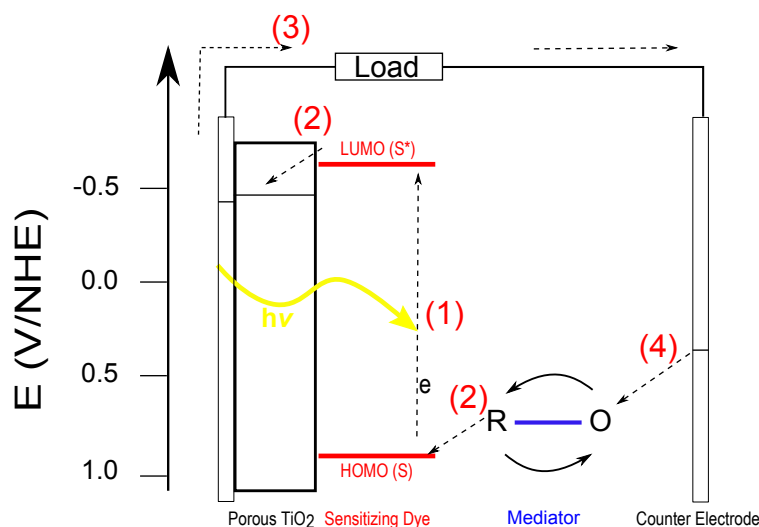


Figure 1.8: Energy diagram and the working principle of a DSSC. Upon the absorption of a photon, an electron is pumped to the LUMO level of the dye (1) and then injected into the titanium oxide conduction band. The dye is then neutralized by the electrolyte (2). The high energy electron then travels to the external circuitry via the conductive glass substrate (3). Finally the mediator is reduced at the counter electrode (4). Dashed lines show the flow of electrons.

external circuitry or recombining through reaction 1.8, does not allow for any storage effect in DSSCs in their current form. However, DSSC's common nature with batteries motivated us to store solar energy directly in the form of chemical energy without the electrical conversation medium. This is unique compared to solar cell battery systems proposed in the literature, and has the potential to decrease the cost and increase the efficiency of the whole system. Redox flow batteries are used as the battery technology of choice because of cost, mobility and safety, which make them an important candidate for large scale energy storage [28].

A solar chargeable redox battery is designed by adding a porous dye-sensitized electrode to the redox battery structure. This results in a DSSC-like half cell in a battery, as depicted in Figure 1.9. During illumination and charging, the sensitized electrode is connected to the reduction electrode in the other half cell via a switch, causing the oxidation of ions in the DSSC and reduction in the second half cell. A charge balancing ion (shown as \oplus) will balance the charge across the two half cells by transport through the membrane. The stored energy can later

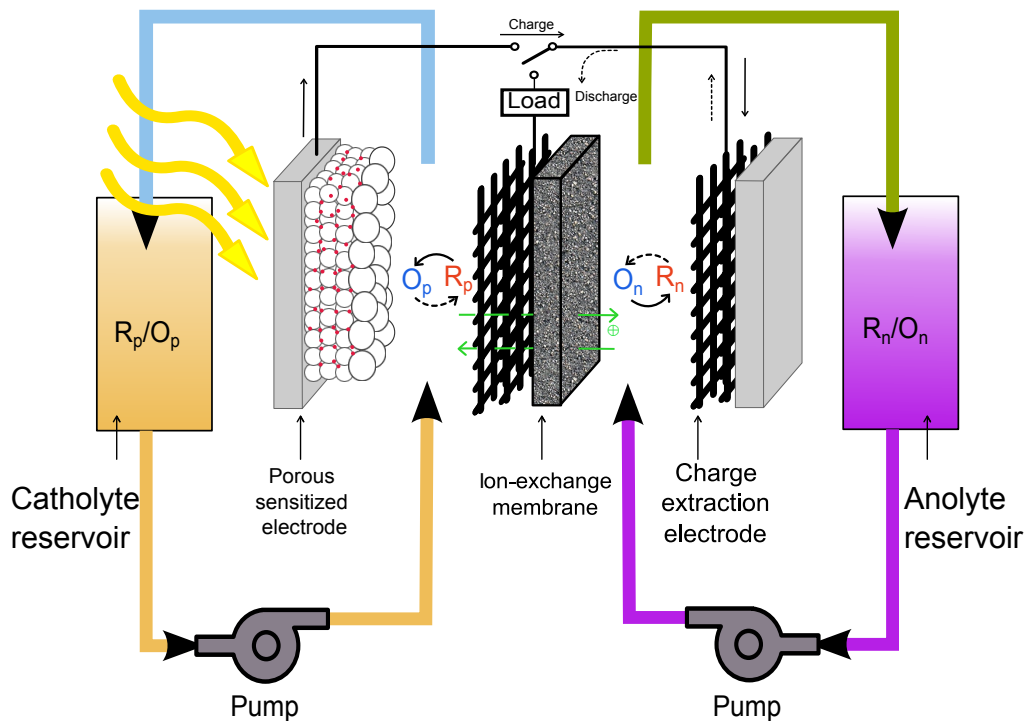


Figure 1.9: Schematic of the solar redox battery. The device working mode is selected by connecting the switch to the photocharging or charge extracting electrodes. Energy capacity is defined by the size of external reservoirs.

be extracted through the two non-sensitized electrodes after changing the switch to discharge mode (middle and right in Figure 1.9). A more detailed working mechanism is presented in Chapter 3.

The demonstration of a working device first involved the identification of proper redox couples that satisfy the requirements of both a DSSC and a redox battery. Secondly, highly catalytic electrodes were selected to interact with the redox couples. These electrodes should minimize polarization losses in the device and should be permeable to the electrolyte so as not to cause significant mass transport losses. Then a membrane was selected to have maximum selectivity over the two redox pairs in order to minimize recombination losses, and have minimum ohmic loss in the system. Finally, the efficiency, capacity and lifetime of the device was studied, and feasibility of the device for the proposed applications should be analyzed.

1.5 Research Objective

An engineering approach towards new structures for combined energy harvesting and storage is presented. The main objective of this work is to integrate both energy conversion and storage capabilities in a single device. Such a device could significantly reduce the fabrication and installation costs of utilization of renewables by reducing the number of parts and seals in the combined harvesting and storage system. Further improvement is expected in balance of system and cuts in energy conversion losses. The candidate technologies for such a purpose are selected and design modifications are investigated to achieve the device. An appropriate materials set (*e.g.* redox couples, electrodes, solvents and membrane) is chosen to work in the designed system. The results are verified through modeling and experiments.

1.6 Thesis Overview

In this chapter, the need is justified for economical large scale storage systems in a carbon neutral electricity grid. Potential benefits of such a storage system is explained and technologies suitable for this purpose are presented. The working mechanism of photogalvanic cells, redox flow batteries and dye sensitized solar cells were reviewed. These approaches are to be used in the next chapters as the building blocks of an integrated solar energy conversion and storage device.

In Chapter 2 an analysis of conventional photogalvanic cells is presented. The requirements for such cells to work efficiently is derived from analytical modeling and their viability is discussed. Most demanding factors are identified and a novel architecture is proposed to overcome the challenging factors. The optimization of the cell is performed with both analytical and numerical modeling.

Steps towards the realization of a commercial photogalvanic cell are taken by looking for a means to achieve selectivity of the electrodes. Semiconducting electrodes are investigated for this purpose. Energy storage capability is discussed and analyzed, and the drawbacks of this system are discussed. In general it is found that even in the optimized configuration suggested,

efficient operation requires the discovery of new materials and techniques, and thus are still not practical.

DSSC-RFB integration is presented in Chapter 3. A solar rechargeable battery is designed and fabricated to address both storage and energy harvesting demands. The methodology is explained and several cell parts are characterized. Experimental results for demonstration of the proposed cell are presented.

Finally, the dissertation concludes in Chapter 4 with guides towards the next steps to be followed for practical solar-battery systems.

Chapter 2

A Vertical Architecture for Increasing Photogalvanic Solar Cell Efficiency: Theory and Modeling ¹

Photogalvanic solar cells, the original dye based solar cells, have yet to fulfill their promise as a low fabrication cost, scalable energy conversion system. The efficient performance of photogalvanic cells relies on high dye solubility and selective electrodes with fast electron transfer kinetics. A new configuration is proposed for photogalvanic cells that removes these impractical requirements. Instead of illuminating the device through the electrode, as is the conventional approach, a new vertical configuration is employed with light coming between the two electrodes. This way, the light absorption and hence electron generation is spread through the depth of the device. The depth therefore can be adjusted according to the concentration of the dyes to absorb all the incoming photons even with low solubility dyes. As a result of distributed electron generation, unreasonably fast electrode kinetics are no longer required. The proposed configuration is mathematically modeled and the advantages over the conven-

¹A version of this chapter has been published in a peer-reviewed journal (Reused with permission from "Mohammad Ali Mahmoudzadeh, John D.W. Madden, 'A Vertical Architecture for Increasing Photogalvanic Solar Cell Efficiency: Theory and Modeling', *Electrochimica Acta*, Volume 143, 2014, Pages 98-105", Copyright 2014, Elsevier Ltd.).

tional cell are shown. A numerical model is built for more detailed analysis that gives practical guidelines for working towards device parameters with high power conversion efficiency. The readily available thionine-iron dye-mediator couple could achieve 6 % efficiency if highly selective electrodes are used, compared to 0.45 % at best using the conventional approach. The analysis suggests that upon the realization of highly selective electrodes and an improved dye/mediator couple, an efficiency of 13 %, and potentially higher, should be achievable from the new configuration.

2.1 Introduction

Solar energy is the most abundant of the readily available renewable energy sources. So far, the cost of conventional solar power relative to fossil fuel alternatives and the absence of supporting energy storage facilities in the electricity grid, have impeded its widespread use in grid-tied locations. Many approaches are being taken to reduce the cost of the solar power. Photogalvanic cells (PGC) were studied immensely in 1980s as a cheap solar energy harvesting system. The photogalvanic effect was first observed in 1925 by Rideal and Williams [29], and it was Rabinowitch that initially investigated the much studied iron-thionine photogalvanic system [30]. Several other groups pursued the work both to understand the mechanism and to find the optimum device configuration for PGCs [31–35]. These studies together with the work on semiconductor electrochemistry by Gerischer [25, 36], Nozik [37] and Gratzel [38] led the design of dye sensitized solar cells (DSSC) [26]. The analytical analysis of PGCs proposed by Albery and Anchor [18] showed the possibility of high performance PGCs given certain conditions of device geometry and chemistry. Use of micelles in photogalvanic cell have been suggested by Groenen *et al.* [39] in order to increase dye solubility and suppress back-reactions. Recently, a set of empirical studies examined a variety of dye/mediator couples, including the study of several dyes by Gangorti *et al.* [22, 40–42], the effect of surfactants by Genwa [21, 43] and even the use of mixed dyes by Lal *et al.* [44]. The highest efficiency of a PGC is claimed by Bhimwal and Gangotri to be 1.62 % with methyl orange as photosensitizer dye [19], which

expresses how far these devices are from practical use. Selective electrodes, fast electrode kinetics and high solubility of the dyes are the main unsatisfied properties of a good PGC. We propose a change in the configuration of the PGC that lightens up some of the hard to achieve requirements and we justify our proposed structure by analytical and numerical analysis.

Instead of illuminating the device through the electrode as was done in the previous work, we suggest vertical alignment of PGCs so that the light comes in from the gap between the two electrodes as shown in Figure 2.1. This way, the light absorption and hence electron generation is spread through the depth of the device. As a result of larger absorption length, smaller current densities are expected and fast electrode kinetics are no longer required. The depth can be adjusted according to the concentration of the dyes, and thus deeper cells enable low solubility dyes to be employed. Multiple devices stack next to each other to cover surfaces. We suggest the investigation of this structure due to more relaxed requirements and higher possible efficiency.

In this chapter, the design guideline for an efficient cell will be presented as was published by Albery *et al.* [32]. The analysis of vertical cells is then presented and the requirements for high efficiencies will be derived from mathematical modeling. Several design factors will be discussed and compared to the conventional cell and the advantages of the new configuration are shown. In the simulation sections the framework of a 2D computer model for PGCs is explained. Both cells are then modeled and optimized, assuming in one case known properties of dyes and mediators, and in the second case given dyes and mediators that should be physically realizable which gives a target configuration for PGCs. The expected efficiencies are compared. The benefits of the vertical cell are demonstrated and the target device parameters are shown to make the cell more viable than the conventional cell.

2.2 Analysis of the Conventional Photogalvanic Cell

The working principles of PGCs are explored in section 1.2. The main reactions governing their performance can be summarized as,

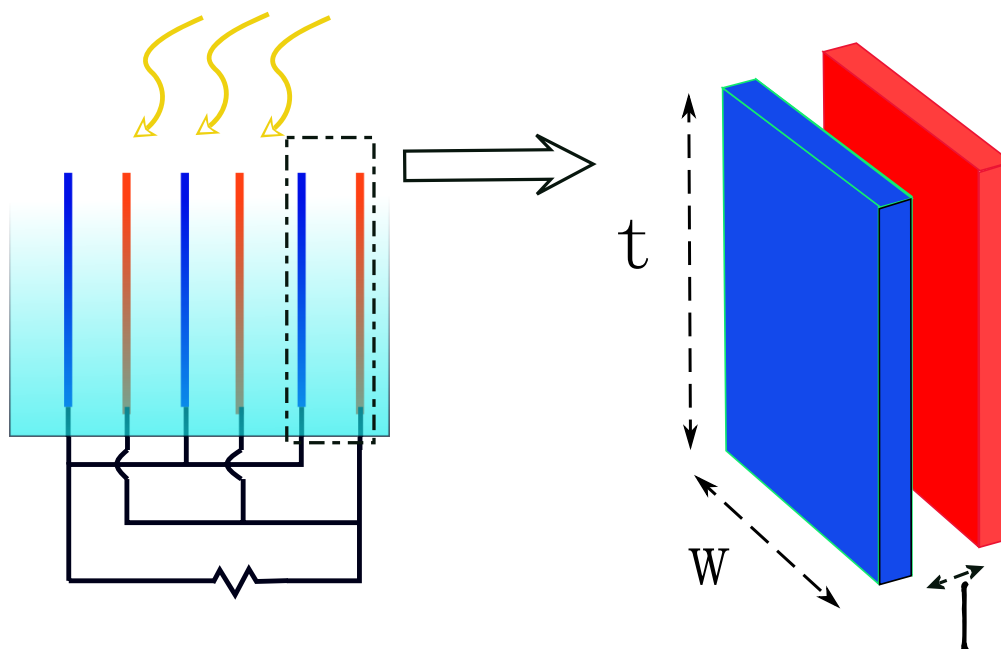
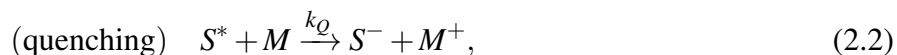


Figure 2.1: Schematic of a vertical photogalvanic cell. The left figure shows several aligned vertical cells to cover a large area. Each cell consists of two parallel electrodes, with small spacing, l . Each electrode should be selective to one of the redox couples.



Albery examined the electrode-illuminated cell of Figure 1.5 analytically and derived some design criteria for photogalvanic cells [18]. The differential equation governing the photo-absorption by dye molecules, the reaction of excited dyes and mediators, and the transport of species were solved simultaneously. The output of the analysis were four characteristic lengths

Table 2.1: Characteristic lengths of photogalvanic devices. ϵ is the extinction coefficient of the dye. $[S]$ is the concentration of the light absorbing dye and $[M^+]$ is the concentration of the oxidized mediator. D is the diffusion coefficient. ϕ_0 is the solar photon flux in units of $[\text{mol cm}^{-2} \text{s}^{-1}]$.

X_l	l	Distance between electrodes
X_ϵ	$(\epsilon[S])^{-1}$	Light absorption length
X_k	$(D/k_r[M^+])^{1/2}$	Typical diffusion length before recombination
X_g	$(D/\phi_0\epsilon)^{1/2}$	Typical distance dye diffuses between photon absorption events

of Table 2.1, which should be balanced according to the cell requirement to achieve a high power efficiency.

The complete absorption of the incoming light requires that the device be deep enough that most of the light be absorbed, or $X_\epsilon \ll X_l$. In order to extract the separated charge, generated M^+ ions need to travel to the illuminated electrode before their recombination, therefore, the distance over which generation is occurring should be less than the length over which it will likely diffuse before recombining through (2.3), and hence $X_\epsilon \ll X_k$. Additionally, the excited dyes should be replaced by fresh ones before the arrival of the next photon in order to avoid solution bleaching, and hence, $X_\epsilon \ll X_g$.

The requirement of a net positive bulk generation requires that generation rate be faster than recombination rate therefore $X_g \leq X_k$. Finally, the maximum travel length is the distance between the electrodes, therefore the other three length constants should be smaller than X_l . The following formula was suggested for these values:

$$10X_\epsilon \approx X_g \approx \frac{1}{2}X_k < X_l. \quad (2.5)$$

These relations define the approximate conditions for the optimized cell. Using the typical values of D , ϵ and I_0 , a set of parameters were derived by Albery *et al.* [32] to make an efficient cell as shown in Table 2.2.

One last requirement is that electrode kinetics be fast compared to the mass transport and

Table 2.2: Albery’s recipe for the optimal cell [32].

$X_g = 10\ \mu\text{m}$	$D = 10^{-5}\ \text{cm}^2\ \text{s}^{-1}$, $\varepsilon = 100\ \text{mM}^{-1}\ \text{cm}^{-1}$, $I_0 = 1.6 \times 10^{-7}\ \text{mol}\ \text{cm}^{-2}\ \text{s}^{-1}$
$X_\varepsilon = 1\ \mu\text{m}$	$\Rightarrow [S] = 0.1\ \text{M}$
$X_k = 20\ \mu\text{m}$	$\Rightarrow k_r[M^+] = 2.5\ \text{s}^{-1}$
$X_l > 20\ \mu\text{m}$	

recombination rates, and thus satisfy the following conditions:

$$k^0 \gg \frac{D}{X_\varepsilon} \quad \text{and} \quad (2.6a)$$

$$k^0 > \frac{D}{X_k}, \quad (2.6b)$$

where k^0 is the standard heterogeneous rate constant. The first condition ensures that the product species are generated close enough to the electrode to be able to interact with it and the second condition provides for a higher chance of electron extraction than bulk recombination.

As explained briefly in the introduction section, the latter condition of electrode kinetics is hard to satisfy, particularly in case of selective electrodes as any surface modification impedes the electron transfer between M ions and the electrode. Additionally, fast electrode kinetics is incompatible with slow bulk reactions according to Marcus theory [45]. In other words, no dye/mediator/electrode combination is likely to be found that offers both fast electrode kinetics and slow bulk recombination. Finally, the solubility of the dyes are much lower than the requirements of Table 2.2 [46], as a result, photogalvanic cells show poor efficiencies. Arranging the light path to be parallel to the electrode surfaces, as shown in Figure 2.1, is now shown to alleviate a number of constraints. We investigate the requirements of target vertical cell in the next section and show that the proposed cell is less demanding in these two areas, i.e., moderate electrode kinetics and dyes with low solubility can still be utilized in an efficient vertical cell.

2.3 Analytical Analysis of the Vertical Photogalvanic Cell

The vertical photogalvanic cell of Figure 1.6 with the reactions shown in Figure 1.5, is modeled in order to estimate the feasibility of the requirements for such a cell to work efficiently. First,

an analytical model is presented that allows defining guidelines for design of efficient target vertical cells. This is followed by a numerical simulation, allowing the cell efficiency to be estimated.

A comparison of maximum generation rate, which happens at the illuminated electrolyte surface, and the quenching rate constants shows that even at small concentrations of mediator, the charge separation of reaction (2.2) happens much faster than the initial photo-excitation of the dyes, reaction (2.1) (as has been previously assumed by Albery [18]). Therefore, the two stages of light absorption and charge separation can be simplified into a single reaction of :



where S/S^- represent the two states of the dye and M/M^+ those of the mediator. G_{op} , k_f and k_r are bulk reaction rates for optical generation, dark forward reaction and bulk recombination, respectively. M/M^+ concentrations are assumed constant in the analysis by adding a condition that mediator concentration is much larger than that of the dye, following Albery [18], in order to enable an analytical solution. As a result of illumination to the gap, the optical generation, G_{op} , varies through the depth. This generation is averaged over the cell depth in our one dimensional analysis and therefore is independent of dye concentration as long as the cell is built deep enough to absorb all the incoming light. The assumptions of uniform generation and constant mediator concentration are removed in numerical analysis provided in the next section.

A diffusion-recombination reaction mechanism is considered for the transport in the bulk at steady-state,

$$D \frac{\partial^2 [S^-]}{\partial x^2} + G_{op} - k_r [S^-] [M^+] = 0. \quad (2.8)$$

In order to simplify the expressions, it is useful to rewrite the equations in dimensionless form. The length is normalized to the cell length, l , and the concentrations to the dark dye concentra-

tion, $[S_d]$. The unitless bulk reaction will be as follows,

$$\frac{\partial^2 u}{\partial \chi^2} + \alpha^2 - \beta^2 u = 0, \quad \text{where}$$

$$\chi = x/l, \quad u = [S^-]/[S_d], \quad \alpha^2 = \frac{G_{op} l^2}{D [S_d]} \quad \text{and} \quad \beta^2 = \frac{l^2 k_r [M^+]}{D}. \quad (2.9)$$

Parameter α compares the cell length to generation length, the distance dye diffuses before being hit by a photon. A large α guarantees dye excitation before traveling the length of the cell. β represents the cell length compared to recombination length, which is the diffusion distance of the charged states before recombination in the bulk. A small β is desired in order to increase the chance of charge extraction. For the analytical analysis section, completely selective electrodes with fast kinetics are assumed to be employed, where each electrode interacts only with one redox couple. The optimum cell performance conditions, which we are looking for, happen under this condition which guarantees minimum recombination. (The effect of the non-perfect mediator discrimination will be explored in the numerical analysis). This assumption allows us to assign all the current from the left electrode to the interaction with the S/S^- couple, therefore,

$$D \frac{d[S^-]}{dx} \Big|_{x=0} = \frac{J}{F} \quad \text{which translates to} \quad (2.10)$$

$$\frac{du}{d\chi} \Big|_{\chi=0} = m, \quad m = \frac{J \cdot l}{FD[S_d]}, \quad (2.11)$$

where J is the cathodic current density, F is the Faraday constant, D is the diffusion coefficient and m is the normalized current density. On the right electrode, no electron transfer happens with dyes due to the complete selectivity assumption. The boundary condition is then

$$\frac{du}{d\chi} \Big|_{\chi=1} = 0. \quad (2.12)$$

Solving equation (2.9) with boundary conditions of (2.11) and (2.12) results in a normalized

concentration profile as follows

$$u = \frac{\alpha^2 - m\beta \cosh(\beta - \beta\chi) \operatorname{csch}(\beta)}{\beta^2}. \quad (2.13)$$

All device characteristics can be derived from equation 2.13- most importantly, the current density, m , which relates to u through (2.11). We can define the cell efficiency in terms of concentration to be able to calculate cell parameters, l , $[S_d]$, $[M^+]$ and k_r , for the optimized cell. The concentration at the surface of the electrode can be written as

$$u_0 = u|_{\chi=0} = \frac{\alpha^2 - m\beta \coth(\beta)}{\beta^2} \Rightarrow m = \frac{\alpha^2 - \beta^2 u_0}{\beta \coth(\beta)}. \quad (2.14)$$

The output voltage of the cell, the difference in electrode's electrochemical potential, is also normalized. The unitless potential difference, ΔP can be calculated as equation (2.17)

$$P = \frac{F}{RT} E \quad (2.15)$$

$$\Delta E = E_2 - E_1 = E_{M/M^+}^0 + \frac{RT}{F} \ln \frac{[M^+]}{[M]} - E_{S/S^-}^0 - \frac{RT}{F} \ln \frac{[S]}{[S^-]} \quad (2.16)$$

$$[M^+], [M] \approx \text{constant} \Rightarrow \Delta P = \Delta P^0 + \ln(u_0^{-1} - 1) \quad (2.17)$$

$$\Delta P^0 = \frac{F}{RT} (E_{M/M^+}^0 - E_{S/S^-}^0) \quad (2.18)$$

The efficiency of the cell can then be calculated by dividing the product of the output current and voltage by the incoming light power. Using equations (2.17) and (2.14), the efficiency can be written in the following form,

$$\begin{aligned} \eta &= \frac{(t \cdot w \cdot J) \cdot \Delta E}{l \cdot w \cdot I_0} \times 100\% = \frac{FD[S_d]RT}{FI_0} \frac{t}{l^2} m \cdot \Delta P \times 100\% \\ &= \underbrace{\frac{D[S_d]RT\Delta P^0}{I_0} \frac{t}{l^2}}_{\theta, \text{ max efficiency}} \underbrace{\frac{\alpha^2}{\beta \coth(\beta)} \left(1 - \frac{\beta^2 u_0}{\alpha^2}\right) \left(1 - \frac{\ln(u_0^{-1} - 1)}{\Delta P^0}\right)}_{\psi, \text{ load dependent}} 100\%. \end{aligned} \quad (2.19)$$

The two right hand side terms are functions of u_0 and therefore m , the current density,

which is dependent on the load connected to cell. In order to deliver the maximum efficiency, one should maximize this part, ψ , by adjusting the load and make those terms as close to unity as possible. The part that mainly governs the magnitude of the efficiency is the leftmost product in (2.19), called θ , that needs to be maximized by adjusting the cell parameters. We first look for the cell conditions that optimize this term, then adjust the load, and therefore u_0 , to maximize the two RHS terms.

2.3.1 Geometry Optimization

Inserting the values of α and β into θ , one can write this efficiency term in the form of

$$\begin{aligned}\theta &= \frac{D[S_d]RT\Delta P^0}{I_0} \frac{t}{l^2} \frac{\alpha^2}{\beta \coth(\beta)} = \frac{D[S_d]RT\Delta P^0}{I_0} \frac{tG_{tot}l^2/(tD[S_d])}{l^2 l \sqrt{\frac{k_r[M^+]}{D}} \coth\left(l \sqrt{\frac{k_r[M^+]}{D}}\right)} \\ &= \frac{RT\Delta P^0 G_{tot}}{I_0} \frac{1}{l \sqrt{\frac{k_r[M^+]}{D}} \coth\left(l \sqrt{\frac{k_r[M^+]}{D}}\right)}.\end{aligned}\quad (2.20)$$

All the variable parameters of equation (2.20) are collected in the second term which represents a half-bell shaped function of β whose maximum occurs at zero, as depicted in Figure 2.2. Charge extraction at the electrodes always competes with bulk recombination, therefore a larger β (faster bulk recombination or wider device) consistently reduces the efficiency. Consequently, the cell length should be decreased to the extent that is allowed by the manufacturing limitations to have an efficient cell. One can see that θ still has 76% of its maximum value when $l \sqrt{\frac{k_r[M^+]}{D}} \simeq 1$, which gives some room to deviate from the maximum point without a huge efficiency loss.

Assuming a slow - but feasible - bulk recombination rate of $k_r = 0.5 \times 10^3 \text{ M}^{-1} \text{ s}^{-1}$, a typical diffusion constant $D = 10^{-5} \text{ cm}^2 \text{ s}^{-1}$, and a cell length of $l = 100 \mu\text{m}$, the mediator concentration should be smaller than $200 \mu\text{M}$ in order to enable reasonable efficiency. Dye concentration should be at least 2 times smaller than that of the mediator so that its change does not disturb the mediator concentration profile, therefore $[S_d] \simeq 100 \mu\text{M}$.

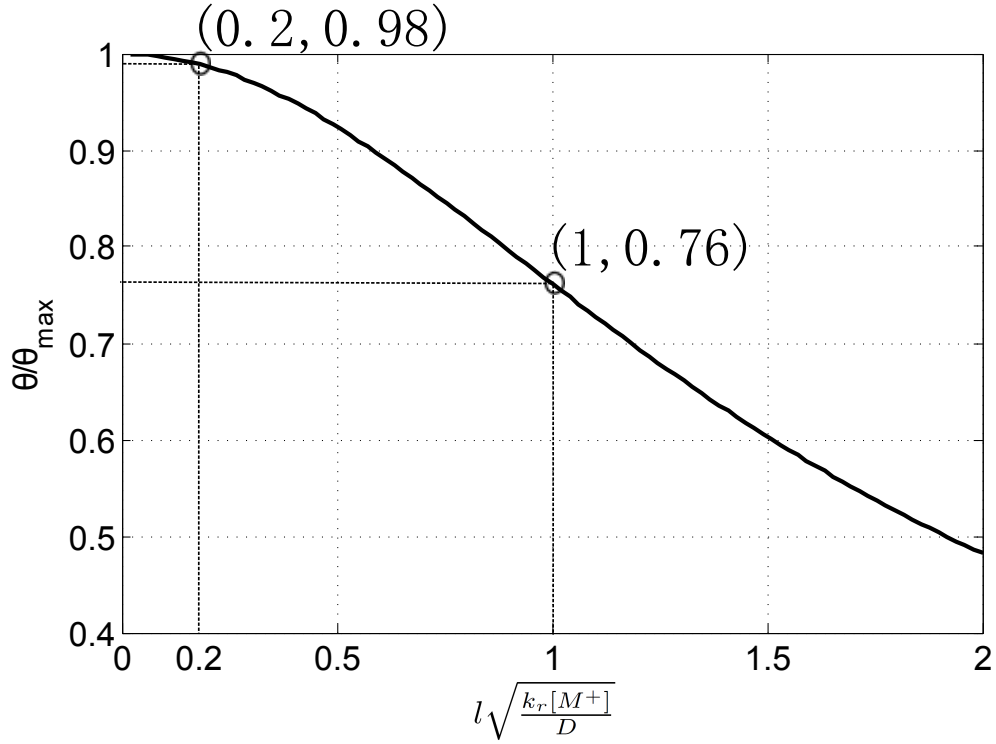


Figure 2.2: Load independent efficiency vs $l\sqrt{\frac{k_r[M^+]}{D}}$. θ_{max} happens at very small device lengths, however, the device length should be balanced between performance and fabrication limitation.

The depth of the cell has no direct influence on θ output power as long as all the incoming light is absorbed in the cell, so the depth should be kept greater than $4\epsilon[S]$. The next term that should be maximized is the $\Delta P^0 G_{tot}$ product in the numerator. ΔP^0 reflects the difference in the electrochemical potentials of two redox couples which should ideally match the HOMO-LUMO levels of the dye minus the required overpotential to drive the electron transfer. Therefore, the larger the difference is, the more significant the output voltage achievable. However, that would result in a smaller portion of incident photons to be absorbed and the G_{tot} to drop since lower energy photons cannot excite the dyes. Balancing the trade-off between G_{tot} and ΔP^0 leads to an optimum HOMO-LUMO level difference of $1.4 eV$, which in turn leads to $\theta_{max} = 24 \%$. This is the maximum efficiency regardless of the effect of the load, *i.e.* $I_{SC} \times V_{OC}/I_0$. Smaller separation between electrodes leads to higher efficiency - for example

with 20 μm separation, θ_{max} can be expected to reach 31 % as the bulk recombination loss drops significantly.

2.3.2 Load Optimization

Both bracketed terms in the load dependent part of equation 2.19 , ψ , should approach unity in order to achieve maximum efficiency. For this section, this condition is assumed to be satisfied and an optimum load condition is calculated. The assumption is subsequently shown to be valid. Keeping that in mind, and neglecting the product of the small terms, ψ can be approximated as :

$$\psi(u_0) = \left(1 - \frac{\beta^2 u_0}{\alpha^2}\right) \left(1 - \frac{\ln(u_0^{-1} - 1)}{\Delta P^0}\right) \simeq 1 - \frac{\beta^2 u_0}{\alpha^2} - \frac{\ln(u_0^{-1} - 1)}{\Delta P^0}. \quad (2.21)$$

Differentiating with respect to u_0 shows a maximum at $u_{0,m} = \frac{\beta^2 - \sqrt{\beta^2 - 4\alpha^2/\Delta P^0}}{2\beta^2}$ and $\psi_m \simeq 0.91$. Figure 2.3 shows the variation of ψ with respect to u_0 for some typical cell parameters, where $u_{0,m}$ is located very close to zero. The maximum efficiency load for this case happens close to the short circuit conditions which happens at $u_0 = 0$ according to equation (2.14).

2.3.3 Estimation of Maximum Efficiency

Altogether, the total efficiency of the vertical photogalvanic cells would appear to go as high as 28 and 22 % for 20 and 100 μm device lengths, respectively. The conditions for such performance are given above. In terms of device length constants, one can conclude the recombination length X_k should be larger than the device length X_l as shown in Figure 2.2. The light absorption in the vertical configuration is not limited to the electrode separation, however, since all the light needs to be captured, the cell thickness must be much larger than X_ϵ , i.e. $d \gg X_\epsilon$. As calculated above, the $l\sqrt{\frac{k_r[M^+]}{D}}$ should be smaller than unity, which puts limits on bulk recombination rate, mediator concentration and device length. In practice not all the given device parameters are readily achievable, but, as will be discussed later, they are more practical than those of traditional PGCs. In the next section these parameters will be fine tuned

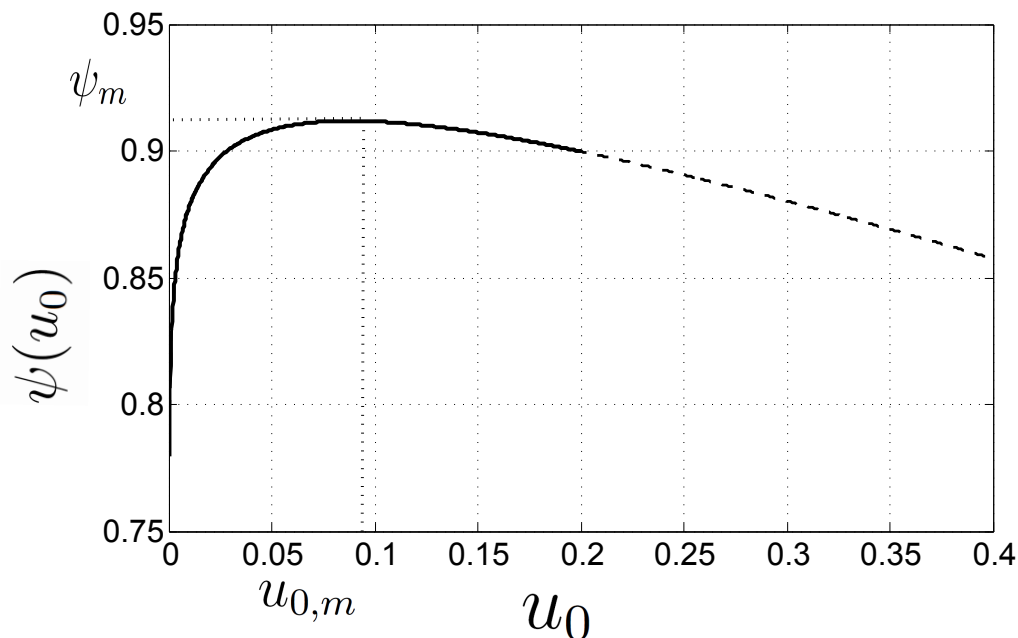


Figure 2.3: The variation of ψ with respect to u_0 . $l = 100\mu\text{m}$, $[M_d] = 200\mu\text{M}$, $[S_d] = 100\mu\text{M}$, $k_r = 0.5 \times 10^3 \text{M}^{-1}\text{s}^{-1}$ and $\Delta E = 1 \text{V}$.

in a more realistic 2D system using electrodes with less than perfect selectivity.

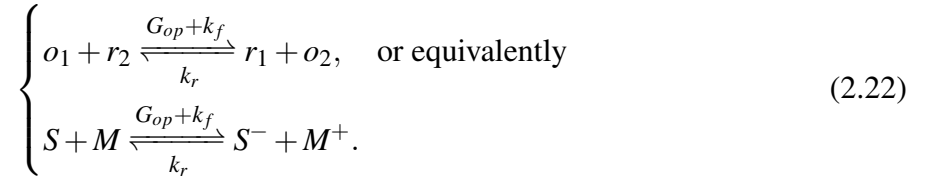
2.4 Simulation of the Photogalvanic Cell

Numerical simulation enables the major assumptions of analytical analysis to be relaxed. A depth dependent generation, variable mediator concentration and imperfectly selective electrodes are modeled which gives a more accurate device analysis. The photogalvanic cell was modeled in COMSOL Multiphysics software (COMSOL Inc., Palo Alto, CA) using a 2D geometry. COMSOL Multiphysics was chosen due to its ability to simultaneously solve several types of differential equations using the finite element method (FEM). The model includes two redox couples in the bulk and two selective electrodes with different reaction rates towards redox species. Bulk transport, generation-recombination and interaction on the electrodes were modeled using the *Transport of Diluted Species* solver in COMSOL. The Butler-Volmer equation was solved on the electrodes with the built in *ODE* solver and light absorption was modeled using the *general PDE* solver, all of which were solved self-consistently in COMSOL. Both

conventional and vertical photogalvanic cells were analyzed numerically first under optimum conditions and then with more readily available parameter values. The performance of the devices were compared for each scenario.

2.4.1 Equation Set

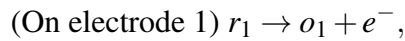
Reactions (2.1), (2.2), (2.3) and (2.4) describe the interactions happening in working photogalvanic cells. Below, the main bulk reaction is shown using both the notations used in the simulation and our analytical analysis,



A reaction-diffusion system of equations is set up to model the transport of species in the photogalvanic cell as shown in equation (2.23),

$$\left\{ \begin{array}{l} \frac{\partial c_i}{\partial t} + \nabla \cdot (-D_i \nabla c_i) = R_i \quad i = o_1, r_1, o_2, r_2, \\ R_{o_1} = R_{r_2} = k_r[r_1][o_2] - k_f[o_1][r_2] - G_{op}, \\ R_{r_1} = R_{o_2} = -k_r[r_1][o_2] + k_f[o_1][r_2] + G_{op}. \end{array} \right. \quad (2.23)$$

On the electrodes, reactions happen at different rates. The selectivity constraint requires that each electrode has fast kinetics with one couple and slow kinetics with the other one and the dominant reaction be that of equation (2.24). The Butler-Volmer equation is used to describe the electron transfer at the interfaces,



$$J/F = k_1^0 \left([o_1]e^{-\alpha f \eta_1} - [r_1]e^{(1-\alpha)f \eta_1} \right) + k_2^0 \left([o_2]e^{-\alpha f \eta_2} - [r_2]e^{(1-\alpha)f \eta_2} \right), \quad (2.25)$$

where η , the overpotential, is the difference between the electrode's potential and the standard potential of the redox couple ($\eta_a = E_{elec} - E_a^0$). α is the transfer coefficient and chosen to be 0.5 in this work which represents a symmetric energy barrier for electron transfer. k_1^0 and k_2^0 are standard rate constants of an electrode's interaction with redox couples [47].

The light absorption follows a Beer-Lambert law behavior in which the reduction in flux that happens in a layer with thickness dl containing species i with concentration c_i , is given by equation (2.26) where ϵ is the molar absorption coefficient,

$$d\phi = -(\epsilon \ln 10) c_d \phi dl. \quad (2.26)$$

The c_d term of 2.26 is the dye concentration in the relaxed state i.e. $[o_1]$. This links the two physics systems, light absorption and transport, together in the process of building a self consistent model.

The other linking variable is the generation term in equation (2.23). Assuming absorption to happen at a constant wavelength for simplicity, one can approximate the optical generation rate as

$$G_{op} \simeq \frac{\phi_{abs}}{\Delta z} \simeq \frac{d\phi}{dz} \left[\frac{mol}{m^3 s} \right], \quad (2.27)$$

where z can be the vertical or horizontal direction depending on the illumination direction. As can be seen in equations (2.26) and (2.27), the generation rate is proportional to the number of absorbed photons at each location which is non-linearly related to the concentration of light absorbers in the relaxed state. The equation system is implemented in COMSOL and the time dependent answer of the system was observed with initial conditions of $[S] = [S_d]$ and $[M] = [M^+]$. The steady state results were then extracted after the time dependent variables reach a plateau. These steady state values were taken as performance figures of the cell and compared for vertical and conventional cells in the next section.

2.4.2 Results

Photovoltaic devices traditionally use electrodes that lie in a plane that is ideally perpendicular to the direction of the incident light. One can extract most of the generated charges by putting the extracting electrode close to the absorbing section (junction). For the same reason, photogalvanic cells are illuminated through one transparent electrode while the other electrode is typically kept in the dark. This way, the peak generation happens very close to the collecting electrode. Despite Albery's initial analysis that showed 18 % efficiency [48], he concluded later that some practical restrictions limit the performance to 5 % [46]. He derived conditions for this 'optimal' cell as shown in Table 2.2. Simulations of the classic iron-thionine cell, and of Albery's 'optimal' cell integrated with a pair of selective electrodes were performed in our 2D model and the device optimization resulted in a power conversion efficiency of 0.45 % and 3.7 %. Thus it is not surprising that the best experimentally measured performance from the PGC is 1.62 % [19] (in which no significant selectivity is present). To understand the ultimate performance expected from these devices, the cell parameters were investigated again in the 2D model. The optimized traditional configuration cell, listed in Table 2.3, showed an efficiency of 2.07 %. Only the extreme case of completely selective electrodes raise the efficiency to 3.7 %.

It should be noted that even this low efficiency performance is impractical in reality. Some characteristics used in Table 2.3 to compute Albery's 'optimal' are incompatible with each other and some are simply hard to achieve. For example, very few redox couples and electrodes meet the very fast electrode kinetics requirement of equation 2.6b. Fast electrode kinetics, needed to produce high currents, are also incompatible with slow bulk reactions (needed to reduce recombination losses between mediators) according to Marcus theory [45]. The actual solubility of the dyes are much lower than those assumed here, which leads to poorer performances in practice compared to the theory.

In the suggested vertical configuration of Figure 2.1, light absorption and charge extraction lengths have been decoupled, therefore a smaller dye concentration can be utilized to reduce the

Table 2.3: Device parameters and performance of electrode illuminated photogalvanic devices. Efficiencies, η , are as computed using COMSOL.

	Albery's Optimal (Perfect Selectivity)	Albery's Optimal (Partial Selectivity) [32]	Iron-Thionine[46]	Explanation
E_S^0	E_S^0	E_S^0	0.462 V	dye standard potential
E_M^0	$E_S^0 + 1.4$ eV	$E_S^0 + 1.4$ eV	0.77 V	M/M^+ standard potential
E_{ph}	1.6 eV	1.6 eV	2.07 eV	dye band gap
$k_{L,1}$	10^{-3} m s ⁻¹	10^{-3} m s ⁻¹	10^{-5} m s ⁻¹	rate constant , fast redox
$k_{L,2}$	0 m/s	10^{-10} m s ⁻¹	10^{-12} m s ⁻¹	rate constant ,slow redox
k_r	5×10^2 M ⁻¹ s ⁻¹	5×10^2 M ⁻¹ s ⁻¹	5×10^2 M ⁻¹ s ⁻¹	bulk recombination rate
l	50 μ m	50 μ m	50 μ m	cell length
$[S_d]$	100 mM	100 mM	100 mM	dye concentration
I_0	1000 W m ⁻²	1000 W m ⁻²	1000 W m ⁻²	light intensity
η	3.7 %	2.07 %	0.45 %	efficiency

current density through the electrodes while not affecting the generated current per illuminated surface. Electrode kinetics need not to be particularly high if dye concentrations are low, and similarly diffusion lengths to electrodes can be relatively long (provided they are similar to or shorter than the recombination length). The selectivity level of each electrode - the difference in reaction rates towards the two redox couples - is investigated. The results show that a 6 to 7 order of magnitude difference in rate constants is enough to achieve an efficient cell.

The vertical cell is modeled in COMSOL, and shows improvement in performance. The efficiencies of the target and iron-thionine cells were found to be 12.9% and 6%, respectively for a 100 μ m cell length. Because of the partial selectivity of the electrodes and the concentration dependent optical generation that were neglected in the theoretical model, these values, achieved with parameters of Table 2.4, are smaller than the prediction of the analytical analysis. The parameters listed in Table 2.4 are chosen with physical feasibility in mind. It is desired to have as small a bulk recombination rate as possible, the suggested dye-mediator couple of the target case is assumed to have a recombination rate in the same range as the iron-thionine couple, which is one of the slower known bulk reaction rates. The value for iron-thionine couple is determined from the literature to be 5×10^2 M⁻¹ s⁻¹ [46]. The dye concentrations are limited

to sub-millimolar range and electrode kinetic rate is on the order of 10^{-5} ms^{-1} . For the target device, the effective band gap is assumed to be equal to the energy difference in HOMO and LUMO of the dye. Also, a 200 mV overpotential is assumed for the bulk homogeneous charge transfer between the dye and the mediator. This is reflected in the difference in dye band gap and M/M^+ standard potential in Tables 2.3 and 2.4.

Device characteristics of the target vertical cell are shown in Figures 2.4a and 2.4b. The low fill factor observed in the Current-Voltage characteristics is mainly due to bulk and electrode recombination losses. Dye concentration and cell depth were swept in value to find the optimum concentration and size which enables both the use of the slow kinetics electrode (by reducing the generation rate) and the full absorption of the incoming light. The light intensity, I , is plotted through the depth of the cell in Figure 2.4c. The horizontal locations where I goes to zero represents full absorption by the dye. In this graph there is small part where not all light is absorbed. The optimum dye concentration is $200 \mu\text{M}$, which is higher than the optimal theoretical value of the last section, because of the effect of bleaching on the surface that was previously ignored in the theoretical analysis. Despite the bleaching, most of the incoming light is absorbed by over a depth of 50 mm.

A comparison of the cell parameters in two configurations reveals the vertical cell to be less demanding. The required electrode kinetics is reduced by two orders of magnitude in the vertical structure and partial selectivity of seven order of magnitudes proves to be sufficient for efficient device performance. This is another advantage of the vertical cell since the 3.7% ultimate efficiency of the conventional cell was calculated based on complete selectivity and it drops to 2.07 % at a selectivity of 7 orders of magnitude. The concentration of the reduced dye, $[S^-]$, is plotted in 2.4d. It reaches zero on the dye-interacting electrode at maximum efficiency operation point, which agrees well with the theoretical prediction that the optimum load happens at very small value of $u_{0,m}$, equation 2.21.

As explained in the analytical section, electrode separation is inversely related to the performance. Figure 2.5 shows the efficiency of top and side illuminated cells for different cell

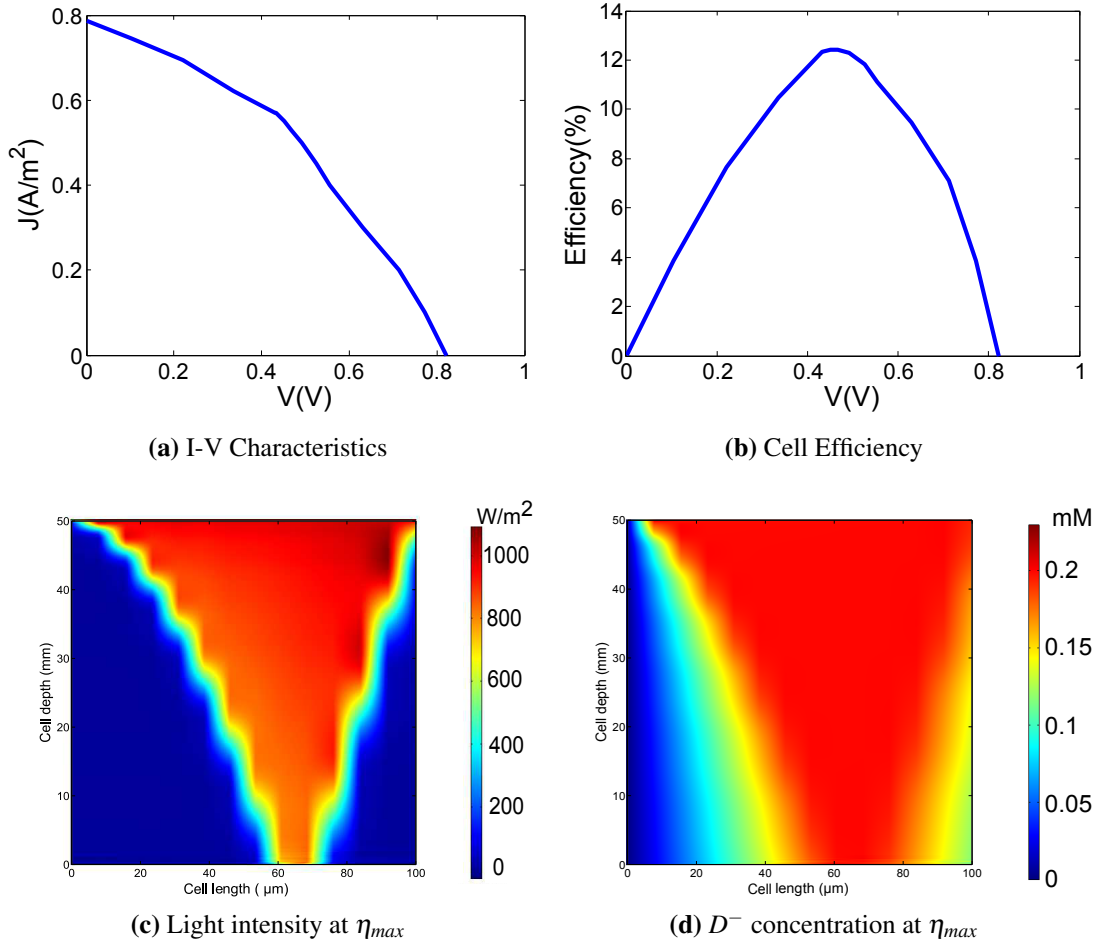


Figure 2.4: Simulation results of the target vertical PGC. $l = 100 \mu\text{m}$, $[M_d] = 500 \mu\text{M}$, $[S_d] = 200 \mu\text{M}$, $k_r = 0.5 \times 10^3 \text{ M}^{-1} \text{ s}^{-1}$ and $\Delta E = 1.4 \text{ V}$

lengths and electrode selectivities. Device performance is more sensitive to selectivity in vertical cell. Therefore, a pair of selective electrodes is crucial in making a practical vertical PGC. For the target cell, this length was set to $100 \mu\text{m}$ for practical reasons, however, as shown in Figure 2.5, efficiencies up to 20.2 % is achievable with thinner vertical cells. It can be seen that 12.9 % efficiency of the $100 \mu\text{m}$ vertical PGC is not achievable with any conventional PGC regardless of the geometry.

Overall, promising device performance is expected with physically feasible parameters which are close to the maximum we think can be achievable. Further research is required to find dye/mediator couples in order to improve these parameters. The fact that each cell is

Table 2.4: Device parameters and performance of vertical photogalvanic devices. Efficiencies, η , are as computed using COMSOL.

	Target vertical cell	Iron-Thionine vertical cell	Explanation
E_S^0	E_S^0	0.462 V	dye standard potential
E_M^0	$E_S^0 + 1.4$ eV	0.77 V	M/M^+ standard potential
E_{ph}	1.6 eV	2.07 eV	dye band gap
$k_{L,1}$	10^{-5} m s^{-1}	10^{-5} m s^{-1}	rate constant, fast redox
$k_{L,2}$	$10^{-10} \text{ m s}^{-1}$	$10^{-10} \text{ m s}^{-1}$	rate constant, slow redox
k_r	$5 \times 10^2 \text{ M}^{-1} \text{ s}^{-1}$	$5 \times 10^2 \text{ M}^{-1} \text{ s}^{-1}$	bulk recombination rate
l	100 μm	100 μm	cell length
$[S_d]$	200 μM	200 μM	dye concentration
t	50 mm	50 mm	cell depth
I_0	1000 W m^{-2}	1000 W m^{-2}	light intensity
η	12.9 %	6 %	efficiency

very thin means that multiple cells must be fabricated in series to cover large areas.

2.5 Conclusion

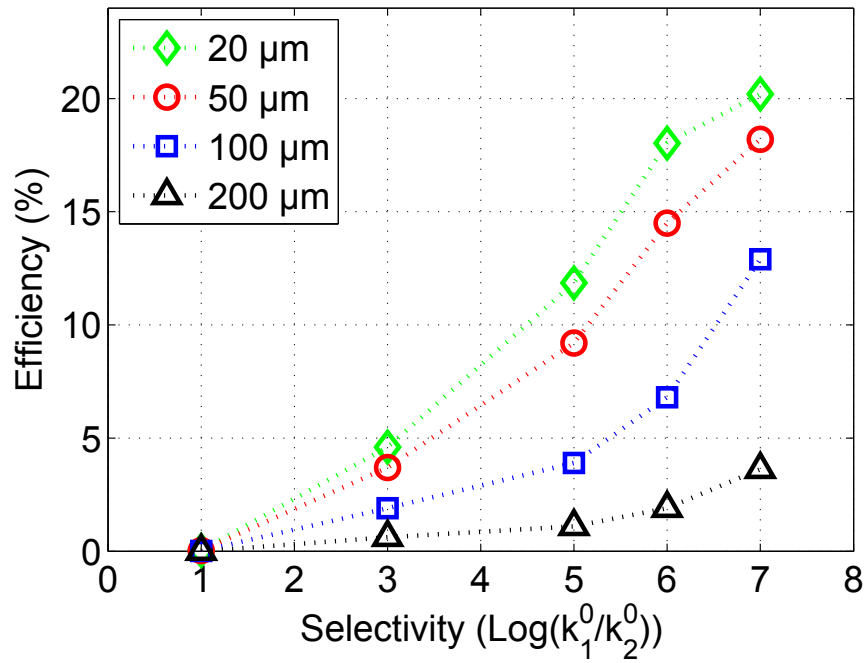
Vertical configuration photogalvanic cells are suggested and modeled. The analysis of an individual cell shows this configuration should result in higher efficiencies than where the illumination is through the electrode. To be effective, sub-millimolar dye concentrations and slow bulk recombination rates on the order of $10^3 \text{ M}^{-1} \text{ s}^{-1}$ are required, which is not easy to achieve but seemingly achievable (the iron-thionine recombination rate is half this number). Electrode kinetics should be reasonably fast, but extending the light absorption through a deep cell makes moderate electron transfer rate constants of 10^{-5} m s^{-1} sufficient, which is 100 times slower than the requirement for the traditional cell. The electrodes were assumed to be completely selective in the analytical section, but optimizing this parameter in the numerical analysis revealed a need for 6 to 7 orders of magnitude difference in rate constants.

Semiconductors are proposed as selective electrodes by our group [49] and so far, selectivity up to 3 orders was shown. The difference in kinetic rates comes from the band edge pinning that happens at a semiconductor-liquid interface. The theory and experimental work

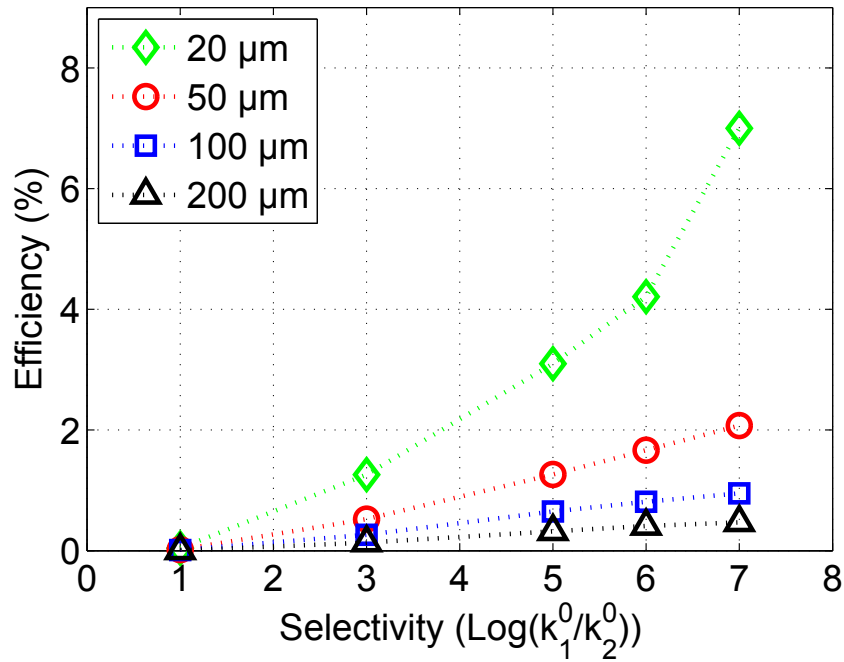
on this method is covered in Appendix B. Given the gap between the required and the obtained selectivity rates, further work needs to be done in this area.

A further challenge is to use this approach for energy storage. With typical recombination rate constants even as slow as $100 \text{ M}^{-1} \text{ s}^{-1}$, energy elevated redox couples recombine in hundreds of seconds in the bulk. Therefore, synthesis of dye/mediator pairs with slower bulk reaction rates are also required in order to achieve practical storage.

All in all, we believe vertical PGCs might be used as cheap, low maintenance solar cells assuming that an appropriate electrode-dye-mediator-electrode combination is found. Incorporation of energy storage for longer than minutes will be challenging. For solar cell and storage in the scale that is demanded by the goals of this work, we investigate a less demanding approach in the next chapter that is based on two relatively well established technologies: the redox flow battery and the dye-sensitized solar cell, as discussed in Chapter 3.



(a) Top illuminated cell



(b) Side illuminated cell

Figure 2.5: Effect of device length and electrode selectivity on cell efficiency for both top and side illuminated cells. The horizontal axis is the selectivity in orders of magnitudes. The effect is shown for different electrode separations as mentioned in the figure legends.

Chapter 3

Solar Redox Battery

In this chapter, an integrated solar energy conversion and storage system is presented using a dye sensitized electrode in a redox battery structure. The design enables independent scaling of the power and energy ratings of the system and thus it is potentially applicable for large scale grid connected storage purposes. A 35 times increase in energy density is observed compared to similar devices by choosing iodide/polysulfide as the pair of active materials matched with permeable porous electrodes. An areal energy density of $52 \mu\text{Whcm}^{-2}$, charge capacity of 1.2 Ah L^{-1} , energy efficiency of 78% and almost perfect Coulombic efficiency are observed for the integrated non-flow cell. The solar rechargeable battery system offers high savings on fabrication and installation costs and a higher round-trip efficiency compared to individual devices.

The chapter begins with a description of the motivation for the work and a review of related literature. Cell design considerations are then discussed, followed by a summary of the results. The chapter wraps up with a detailed presentation of experimental methods.

3.1 Introduction

The global concerns over the impact of conventional energy sources on the environment have resulted in a great interest in carbon-neutral energy generation. Solar energy is the only re-

newable source that can supply all the global energy demand projected in 2050 [5]. However, variability during daytime and intermittency as a result of atmospheric conditions are hindering its widespread use. Therefore, large-scale electrical energy storage systems are required to balance the grid during supply shortage. Compared to solid-electrode batteries, redox flow energy storage systems have several advantages for grid applications such as scalability and low self discharge [50]. These features are incorporated into a design of an integrated solar energy harvesting and storage system.

A solar power rechargeable battery could lead to cost and space efficiency and reduce the complexity of solar energy harvesting systems. Several attempts have been made to achieve such a device starting with back to back fabrication of the battery and solar cell [51, 52]. Although this method reduces some internal losses, it still involves two individual devices being fabricated and offers no material or fabrication cost benefits.

Being an electrochemical cell and having structures similar to batteries, DSSCs are good candidates to be integrated in a solar battery. The first DSSC device capable of energy storage is introduced by Miasaka *et al.* [53] in 2004. Their photocapacitor is based on two membrane separated activated carbon layers for charge storage. They used a platinum electrode on one side and a dye sensitized electrode with a solid hole conductor on the other side. A capacitance of 0.69 Fcm^{-2} , discharge capacity of 0.02 mAhcm^{-2} and charge state voltage of 0.45 V are observed from this device. The same group improved their work by adding a third electrode between the supercapacitor and the dye sensitized electrode to overcome the high internal resistance of the sensitized electrode for charge/discharge and also to prevent the contamination of the charge storage section with redox couples from the solar cell parts [54]. The areal energy density is improved from $9.3 \mu\text{Whcm}^{-2}$ to $47 \mu\text{Whcm}^{-2}$ and the voltage is increased to 0.8 V.

A pseudo-capacitor using tungsten oxide for energy storage is demonstrated by Saito *et al.* [55]. The work is continued by using interdigitated Nafion / polypyrrole-platinum electrodes [56]. The similar geometry of the device to a simple DSSC allows for its integration into the existing DSSC devices. A discharge capacity of $10.5 \mu\text{Ahcm}^{-2}$ is obtained in this

cell which is almost half of the value achieved from a mesh type three electrode setup with the same materials, mainly because of the smaller effective surface area, lower quality of PPy and leakage of I_3^- through the Nafion membrane. Yang *et al.* developed a flexible integrated device using films of free-standing and aligned carbon nanotubes for energy storage, and a dye sensitized electrode for charging. The photoelectric conversion efficiency and specific capacitance are measured to be 6.1 % and 48 F g^{-1} . The areal energy density of the device is measured to be $54 \mu\text{Ahcm}^{-2}$ [57]. Recently, a dye-sensitized photo-electrode was shown that is integrated into a lithium-oxygen battery for photo-assisted charging [58]. The maximum photocurrent density from this device is only $150 \mu\text{Acm}^{-2}$, however, the charging over-voltage of the battery dropped by up to 0.6 V with the assistance of the attached DSSC.

These efforts in the integration of DSSCs and batteries can be classified into two groups. First, the devices where the active energy storage and energy conversion materials are separated as shown in Figure 3.1a. The three electrode setup is achieved by using a bi-functional center electrode. These devices are in fact similar to back-to-back fabricated solar cell-battery structures and their working mechanism involves undergoing similar energy conversion steps as in the individual solar cells and batteries [53, 57, 58]. After the illumination, electrons are pumped into the TiO_2 conduction band, travel through the external circuitry and reduce the active materials at the end electrode. Meanwhile in the DSSC, redox species are oxidized on the photo-electrode and reduced at the center electrode. The latter electron transfer is balanced by the oxidation of the active material at the other side of the bi-functional electrode. This way, solar energy is practically stored in a separate device from the DSSC. In the second group, which is the goal of this work, some active parts are shared between the energy conversion and storage devices (Figure 3.1b) [55, 56]. The mechanism involves fewer energy conversion steps compared to two separate devices, which could lead to improvement in solar energy storage yield and the total device cost at the expense of a more complex structure. During the photo-charging, electrons flow through the external circuitry and reduce the active materials at the end electrode. The redox species are then oxidized on the photo-electrode and the solar energy

is readily stored.

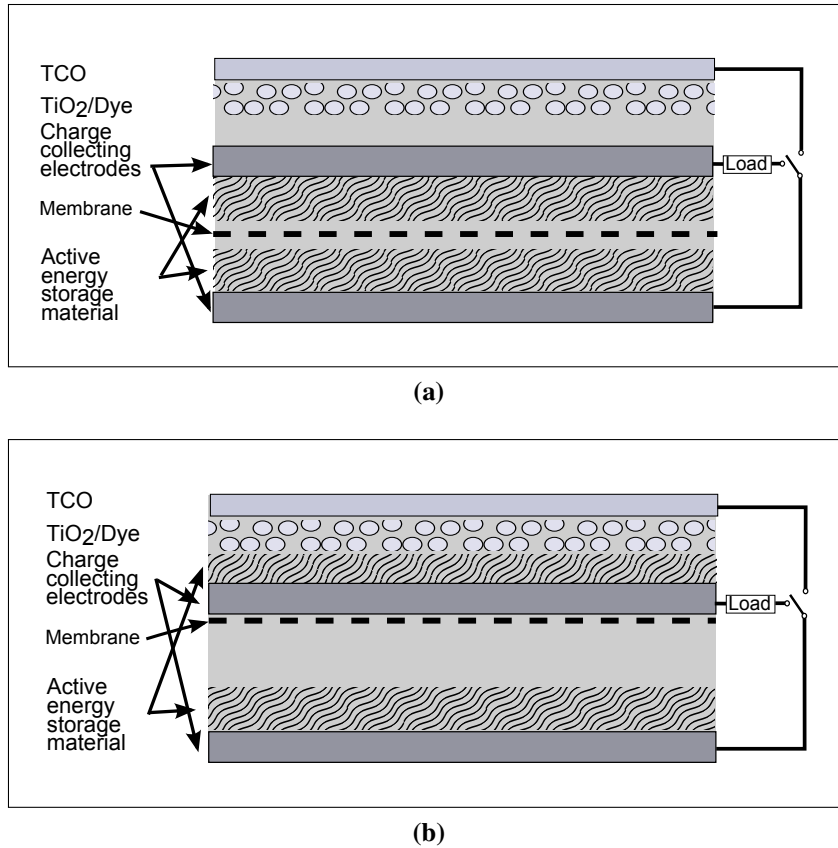


Figure 3.1: Schematic of different approaches towards the integrated solar battery. The operation mode is selected by the switch.(a) Back-to-back fabricated solar cell and battery. The middle electrode is shared between the two devices.(b) Integrated solar battery. Both half cells are active during energy capture and storage. Active energy storage materials are shared between the two operation modes.

Although these devices might be practical to cover for short term variations in sunlight, they still do not have enough capacity for overnight energy storage even if the high energy density of Li-Ion cells are to be achieved within an integrated solar cell. While an energy density per unit area of at least 20 mWh cm^{-2} is needed to store solar energy received in four hours of daylight even for a modest performance solar cell of 5% efficiency¹, the storage capacity of the aforementioned devices range from $0.1 \mu\text{Wh cm}^{-2}$ [53] to $47 \mu\text{Wh cm}^{-2}$ [54]. Considering the fundamental limitation of solid batteries, this work incorporates a technology that allows independent scaling of energy and power ratings, *i.e.* redox flow batteries (RFBs),

¹ $E_{4h} \simeq 1000 \text{ W m}^{-2} \times 5 \% \times 4 \text{ h} = 20 \text{ mWh cm}^{-2}$

in the proposed solar battery system.

Redox flow batteries are electrochemical cells with active materials stored separately from the power conversion electrodes. RFBs have two half-cells, separated by a membrane as depicted in Figure 1.7. The active material is typically a liquid containing redox active mediators such as the vanadium (V^{2+}/V^{3+}), or bromide/polysulfide couples that can be pumped through the cell. This segmentation results in an energy capacity, independent of the power generator size, which gives more freedom in the selection of the electrocatalyst and active materials. Increased electrode area provides more power, and increased storage volume enables a higher capacity. Porous electrodes are normally employed for charge extraction due to their permeability and high surface area. Increasing the size of reservoirs can allow the device to reach the theoretical capacity of its active material as the mass and volume of other parts becomes insignificant compared to that of active material. Currently installed RFB systems range from 10^2 up to 10^7 Wh capacity which is one order of magnitude larger than any Li-ion or lead acid battery system [13]. This size range is appropriate for industrial and grid scale applications.

This work presents a scalable approach towards the integration by utilizing RFB technology as the energy storage method while keeping the higher solar energy yield approach of shared active materials between solar cells and batteries (the second group explained above).

A cost analysis of single-cell solar batteries based on DSSC and RFB technologies compared to separate solar panel/Li-ion battery systems, shows a 30 % lower cost for the integrated system in large scale energy conversion and storage facilities. The calculations are summarized in Appendix C. The saving is expected to increase as the storage technology improves and its price drops. This way, the share of solar panels in the total cost increases and a saving in that segment is heightened.

The only integration of a dye-sensitized electrode in a RFB is reported by Yan *et al.* using aqueous Li_2WO_4 or quinoxaline as negative and LiI in organic electrolyte as positive half-cell electrolytes (in 2013 and 2014 [59, 60]). The schematic of such a device is depicted in Figure 3.2. This results in a DSSC-like half cell in a redox battery. During illumination and

photo-charging, Figure 3.2a, the sensitized electrode is connected to the reduction electrode in the other half cell via a switch, causing the oxidation of ions in the DSSC and reduction in the second half cell. A charge balancing ion (shown as \oplus) balances the charge across the two half cells by transport through the membrane. The stored energy can later be extracted through the two non-sensitized electrodes after changing the switch to discharge mode (Figure 3.2b). While the theoretical capacity of Yan's system is claimed to be 5.359 Ah L^{-1} , they only observed a charge density of 32.9 mAh L^{-1} and an energy density per electrode unit area of $\sim 3.5 \mu\text{Whcm}^{-2}$. They attributed this marginal utilization to several factors, including partial redox reactions in the working regime of the device, large internal resistance and high polarization losses at the electrodes. All these, indicate that major device optimization is required to improve the performance of solar redox batteries.

In this work, a solar redox battery with the highest reported charge density and energy capacity is independently developed as a solution for the solar-battery integration challenge based on iodide/polysulfide redox couples using electro-catalytic porous electrodes. The charge density of the proposed device is measured to be 1.2 Ah L^{-1} which is 35 times larger than that of Yan's work. An energy density per electrode area of $52 \mu\text{Whcm}^{-2}$ is achieved which is a 13 times improvement over the previous work on solar redox batteries.

The proposed device is demonstrated by showing the photocharge/discharge response of the cell. It involves identifying the proper redox couples and optimizing the physical parameters for efficient performance as both a solar cell and a battery. The complete cell is assembled in a sandwich structure and tested for efficiency, cycle life and energy capacity.

3.2 Design

In this section, the requirements for an efficient solar redox battery are discussed and materials are chosen for each part of the cell. The theoretical capacity of the proposed device is investigated and compared with the experimental data.

Redox couples and the electrodes. — The positive half-cell electrolyte should have max-

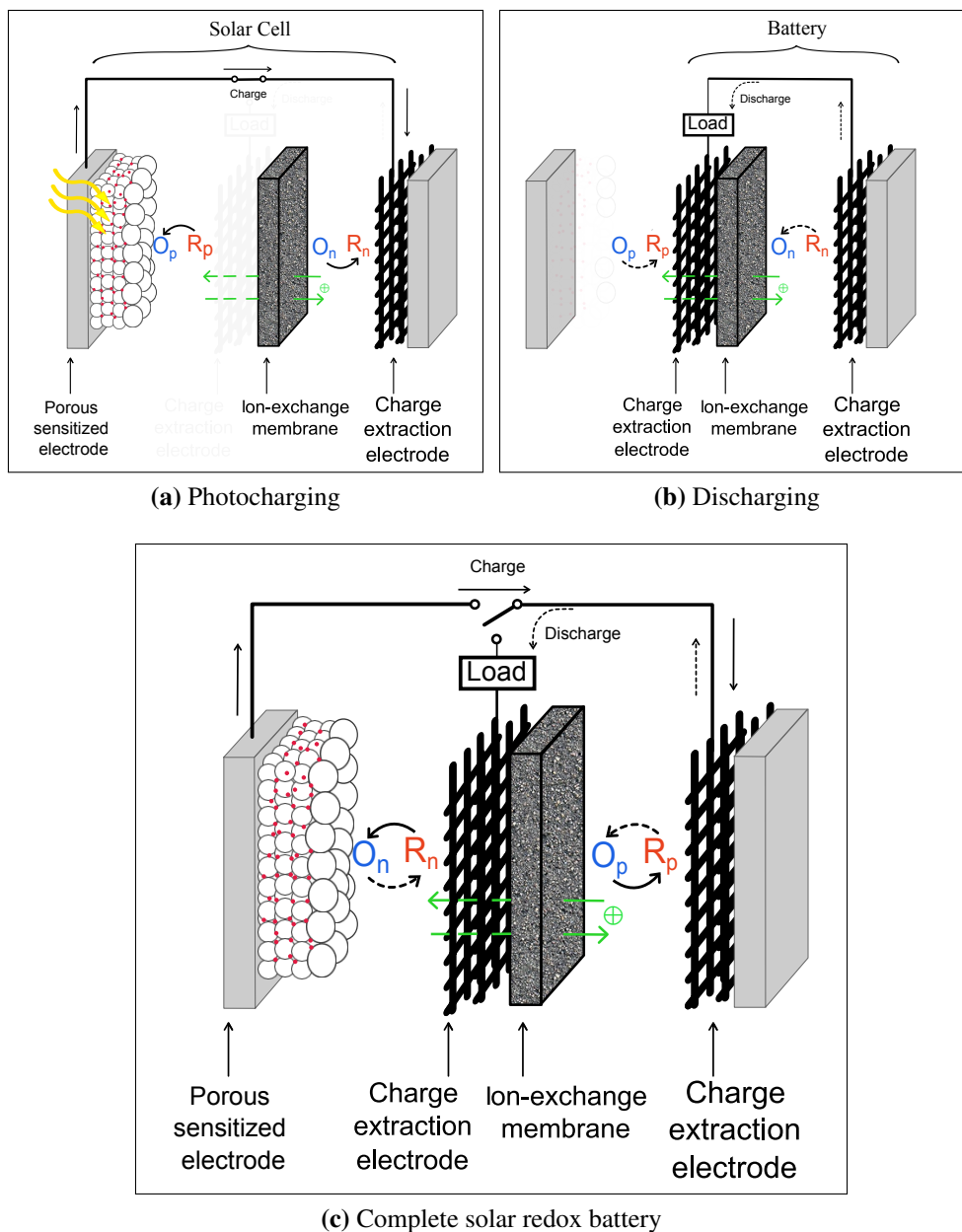


Figure 3.2: Schematic of a solar chargeable redox battery. Solid arrows show the electron flow direction during photocharging and dashed arrows represent the discharge. The inactive parts in each scenario are faded. (a) Photocharging. The sensitized electrode is connected to the charge extraction electrode in the other half cell. (b) Discharging through two porous electrodes. (c) Complete schematic of the cell.

imum compatibility with the sensitized electrode for solar energy conversion purposes. A review of the DSSC literature shows that only very few redox couples can be effectively used as mediators in a DSSC structure. In order to achieve a highly efficient DSSC, the redox mediator should have an electrochemical potential very close to the HOMO of the sensitizing dye, slow kinetics of electron transfer from TiO_2 , a fast kinetic rate with the current collector counter electrode, a high diffusion coefficient to minimize mass transport losses, low light absorption in order not to compete with the dye and good stability in the cell and in contact with the metal electrodes. Energy storage additionally requires the redox couple to be highly soluble in order to allow for high energy capacity, and be compatible with ion selective membranes to prevent leakage to the other half cell.

The iodide/triiodide couple is chosen as the active material of the positive electrolyte. It has been proven to be one of the very few effective mediators for DSSCs [61]. It also has higher solubility, and thus higher capacity, compared to cobalt based mediators, which are the other popular redox group used in DSSC fabrication.

The anodic redox couple should have the last two properties of the first mediator with a standard potential close to the TiO_2 conduction band. It is reasonable to look at the redox couples that have been shown to be practical in RFBs as they already satisfy most of the mentioned prerequisites. Some of these redox couples with feasible redox potentials are depicted in Figure 3.3. Among these, polysulfide ($\text{S}_4^{2-}/\text{S}_2^{2-}$) is selected because of its standard potential which is close to the conduction band edge in TiO_2 , its fast electron transfer rate, high solubility, its high stability and the fact that cross contamination can be avoided by using a cationic exchange membrane (CEM) if coupled with a (I_3^-/I^-) half cell. In fact, polysulfide has been widely used together with bromine, an element right above iodine in the periodic table, as a high energy density RFB [62].

While Pt is the default catalyst for I_3^-/I^- reaction, finding a current collecting electrode to interact with PS needs further experiments and comparison of the materials activity towards the PS redox couples. The activity is measured using a potentiodynamic sweep around the redox

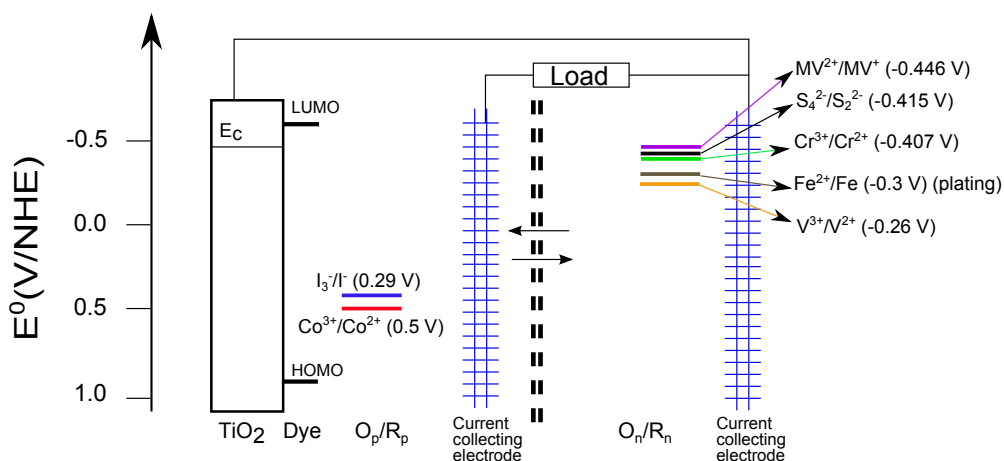


Figure 3.3: Energy diagram of Redox couples for the solar redox battery (SRB). The energy levels of the TiO_2 electrode, dye (HOMO and LUMO), and well established DSSC mediators are shown on the left hand side of the cell. On the right hand side of the membrane (vertical dashed line), candidate redox couples for completing the cell are shown with their respective standard potentials.

potential of the respective redox couple. It is assumed that in each experiment the electrode's current is Faradaic and is only sourced from the reaction with the active species. A reasonable design goal for energy conversion and storage applications is an electrode with current densities on the order of 10 mAcm^{-2} and an overpotential smaller than 100 mV [63]. The design of this work also requires the electrode to be permeable to the electrolyte. A literature survey shows that polysulfide electrolytes have been a candidate for several electrochemical cells such as the Na-S batteries [64], bromine-polysulfide redox flow batteries [62], semiconductor/liquid junction solar cells [65] and lithium-dissolved polysulfide batteries [66]. Materials such as MoS_2 , Ni, Co, NiS, PbS [67], WC[68], WS_2 [69] and a variety of carbons [70] have been suggested as highly catalytic electrodes for polysulfide. Based on their reported performance, it was decided to investigate Ni, NiS and Pt electrodes at the anode. The activities of these electrodes are investigated and depicted in Figure 3.4.

The highest activity is observed from the acid treated, sulfurated nickel foam electrode. A set of experiments is performed to maximize the electrocatalytic activity of this electrode by changing acid and polysulfide treatment times. The Tafel parameters of these electrodes are

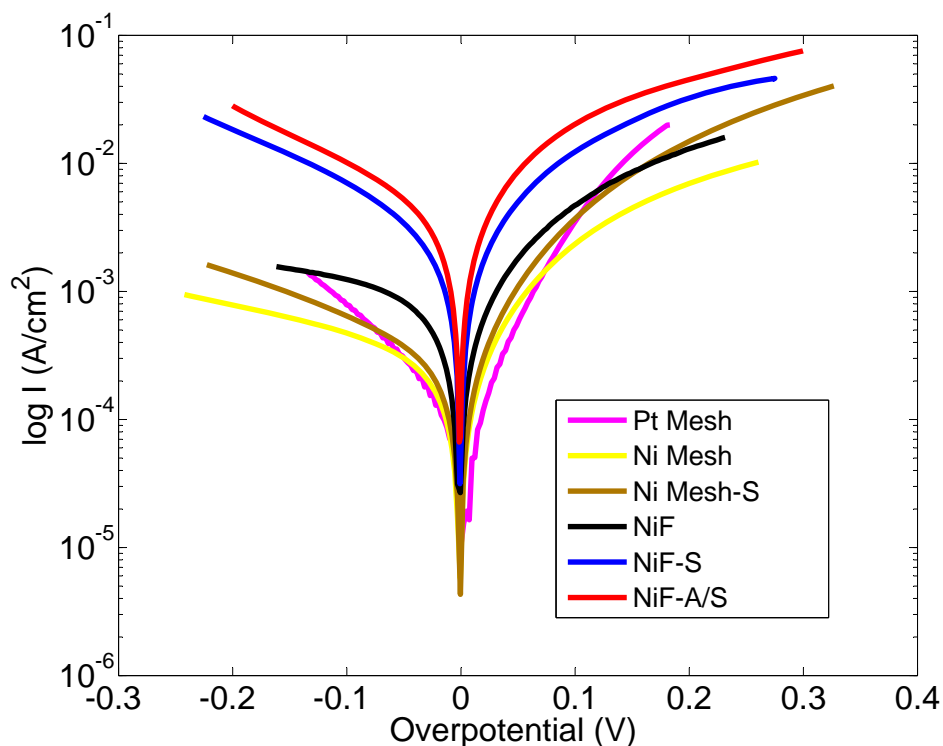
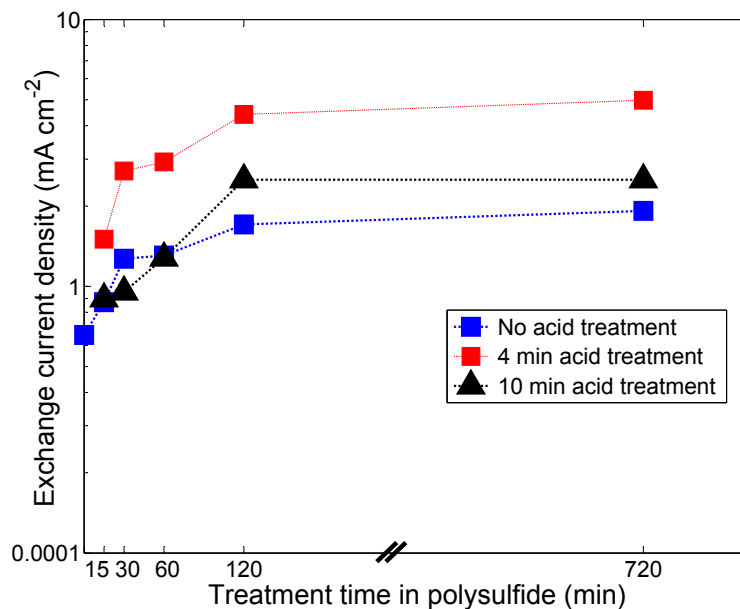


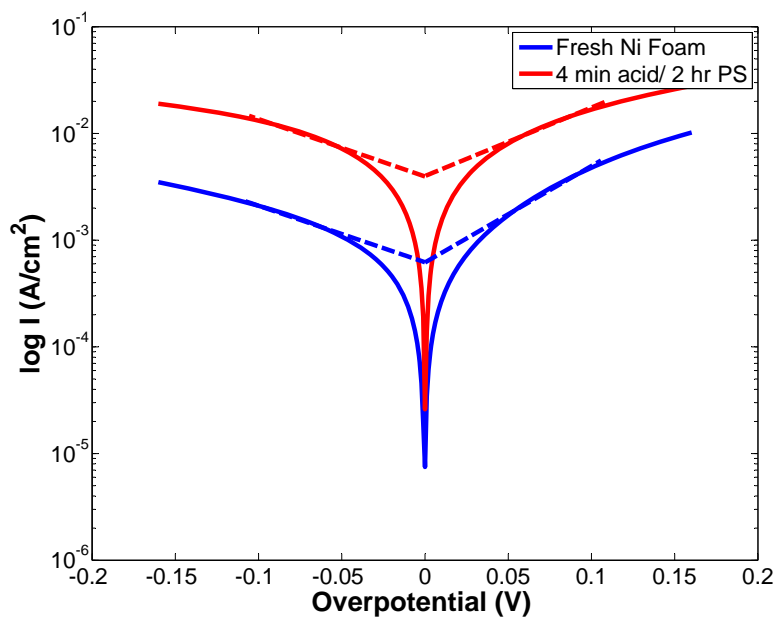
Figure 3.4: Tafel plots of several electrodes towards the polysulfide redox couples. The electrolyte is 1 M Na_2S_4 , 1 M NaClO_4 in AcN/THF (2:1 v/v). The scan rate is 10 mVs^{-1} . During solar charging a current of 10 mAcm^{-2} must be maintained with minimal potential drop. Nickel Foam (NiF) is seen to enable good current density with relatively small overpotential ($< 200 \text{ mV}$).

extracted by fitting the polarization data to the exponential Tafel behavior of the Butler-Volmer model, $i = i_0 \times 10^{\pm\eta/b}$, where i is the electrode current, i_0 is the exchange current density, η is the overpotential and b is the Tafel slope that could be different for anodic and cathodic branches. Average anodic and cathodic exchange current densities for Ni foam samples with different treatment times of acid and polysulfide are plotted in Figure 3.5a. The activity is increased with polysulfide treatment time up to 120 min and reaches a plateau around that time. It is also shown in 3.5a that long acid exposure time has an adverse effect on exchange current densities, mainly due to the corrosion of the porous metal.

The Tafel parameters of the Ni foam electrode with the best performance are compared to fresh Ni foam and listed in Table 3.1. With exchange current density of $\sim 4 \text{ mAcm}^{-2}$, this



(a)



(b)

Figure 3.5: (a) Average anodic and cathodic exchange current densities for Ni foam samples with different treatment times of acid and polysulfide. (b) Tafel plots of fresh vs. treated Ni foam electrodes. The electrolyte is 1 M Na_2S_4 , 1 M NaClO_4 in AcN/THF (2:1 v/v). The scan rate is 1 mV s^{-1} .

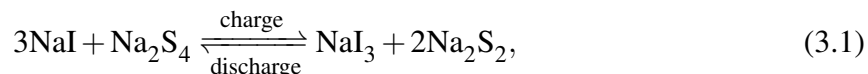
electrode is sufficient to handle the photo-generated current with insignificant polarization loss. At 100 mV overpotential, the activated electrode drives 17 mAcm^{-2} and 14 mAcm^{-2} anodic and cathodic currents respectively.

Table 3.1: Polarization of Ni foam electrodes in polysulfide electrolyte.

Electrode	i_0 (mAcm^{-2})	Anodic $b(\text{mV decade}^{-1})$	Cathodic $b(\text{mV decade}^{-1})$
Ni Foam, fresh	0.62	110	188
Ni Foam, acid/PS	4	155	185

Electrolyte solvent. — Another component that should be mutually compatible between the DSSC and the battery is the electrolyte solvent. Aqueous electrolytes are most commonly used for redox flow batteries and the use of non-aqueous electrolytes is normally limited to high voltage batteries where water electrolysis could disrupt device performance. However, water based DSSCs are not very promising at the moment because of dye detachment, formation of iodate, and decrease in lifetime of the photoexcited electrons [44]. Low viscosity, polar organic solvents such as acetonitrile (AcN), ethylene carbonate (EC), propylene carbonate (PC) and methoxypropionitrile (MPN) are typically used for ruthenium dye based DSSCs [61]. However, polysulfide solubility in PC, EC and MPN is reported to be less than 0.1 M [71] which is not practical for a redox battery because it results in a very low energy density. First, we tested AcN as solvent of an iodine/polysulfide redox battery but it showed very poor rechargeability characteristics. The reason is found to be the limited solubility of small chain polysulfide anions in AcN. Other than water, tetrahydrofuran (THF) [66], dimethoxy ethane (DME) and 1,3-dioxolane (DOL) (1:1 v/v) [72, 73] are reported to have high solubilities of polysulfides ($\sim 10 \text{ M}$). Although none of them has directly been utilized in a DSSC device, a mixture of THF in AcN is reported to have a positive effect on DSSC performance at up to a 30% volumetric ratio of THF in AcN [74]. An AcN/THF (2:1 v/v) mixture is used in this work to simultaneously address the high redox solubility need of a redox battery and low viscosity, high polarity requirements of DSSCs.

Considering all the design requirements, a material set suitable for an integrated DSSC-RFB are selected and listed in Table 3.2. The net reaction from this battery is represented by



which leads to a cell open circuit voltage close to the difference in electrochemical potentials of $\text{S}_4^{2-}/\text{S}_2^{2-}$ (-0.415 V vs. NHE [75]) and I_3^-/I^- (0.29 V vs. NHE [76]), *ca.* 0.7 V .

Theoretical charge density of a battery with these components, is estimated as

$$Q_V = n \times m \times F,$$

where n is the number of electrons exchanged in the charge/discharge process, m is the molar concentration of the redox and F is the Faraday constant which is equal to 26.8 Ah mol⁻¹. This capacity is calculated for both half cell and the smaller value is used as the limiting capacity. Cathodic and anodic charge densities are calculated based on 1 M solutions of iodide and polysulfide with $n_I = 2/3$ and $n_{PS} = 2$. The capacity of iodide and polysulfide half cells are 17.8 AhL⁻¹ and 53.6 AhL⁻¹ respectively. Therefore, the theoretical capacity of the I-PS redox battery is ~ 12.68 AhL⁻¹ after consideration of both half cells.

Performance is first investigated in an iodide-polysulfide redox battery structure without the inclusion of photocharging. Upon verification of reversible electrochemistry and the stability of electrolytes, the complete system is assembled and characterized. The results of these tests are presented in the next section. Details of the experimental procedures follow in section 3.5.

Table 3.2: List of materials for an efficient, high energy density solar redox battery.

Device part	Material
Photoelectrode	15 μm TiO ₂ sensitized with N719 dyes.
Cathode current collecting electrode	Pt Mesh
Positive electrolyte	1 M I ₂ , 0.1 M NaI, 1 M NaClO ₄ in AcN/THF (2:1 v/v)
Anode current collecting electrode	Ni Foam, acid/PS pre-treated
Negative electrolyte	1 M Na ₂ S, 3 M S, 1 M NaClO ₄ in AcN/THF (2:1 v/v)
Membrane	CMI-7000

3.3 Results

High energy density and Coulombic efficiency combined with device stability and cycle life are the prerequisites of any battery. A solar-battery should also have high energy conversion efficiency. These characteristics are first investigated in individual battery and solar cells and then in the solar redox battery.

Iodide-Polysulfide redox battery performance. — A redox battery is fabricated and tested using the materials listed in Table 3.2 in an H-type cell. The cell is charged/discharged (partially) for 10 cycles at a constant current density of 0.1 mAcm^{-2} to analyze the cycle life, as shown in Figures 3.6 and 3.7. A discharge voltage of 0.51 V and a charging voltage of 0.69 V are measured for the battery. The 0.18 V voltage difference is due to ohmic losses in the membrane and polarization losses on the electrodes.

The discharge capacity of the cell discharged to 0.1 V is 0.15 AhL^{-1} after the 10th cycle, which is only 1.2 % of the theoretical capacity. This low capacity can likely be attributed to the limited contact of the electrodes with the bulk electrolyte in the non-flow structure of the experiment, so that much of the electrolyte is left unaffected by the discharge, as ions have not reached the electrode. This will be improved in the combined solar/battery where the spacing between electrodes is small. Initial energy efficiency of 75% is observed during these partial cycles, which drops to 67% after the 10th cycle as depicted in Figure 3.7b. Considering the long cycle times (2 h / cycle) and open configuration of this battery, a gradual deterioration of the performance is expected as the volatile solvent evaporates.

DSSC performance. — The DSSC is tested using the positive electrolyte prescribed for the battery. The electrode separation is set to 0.3 mm to mimic that of the solar-battery structure. The IV characteristics and short circuit current are depicted in Figure 3.8. The drop in short circuit current from 7 mAcm^{-2} to 4 mAcm^{-2} over the 1000 s of this experiment, and the regaining of some of the current after resting for another 1000 s, suggest a mass transfer limited current. The bulk mass transport phenomenon has been previously studied in DSSCs and a

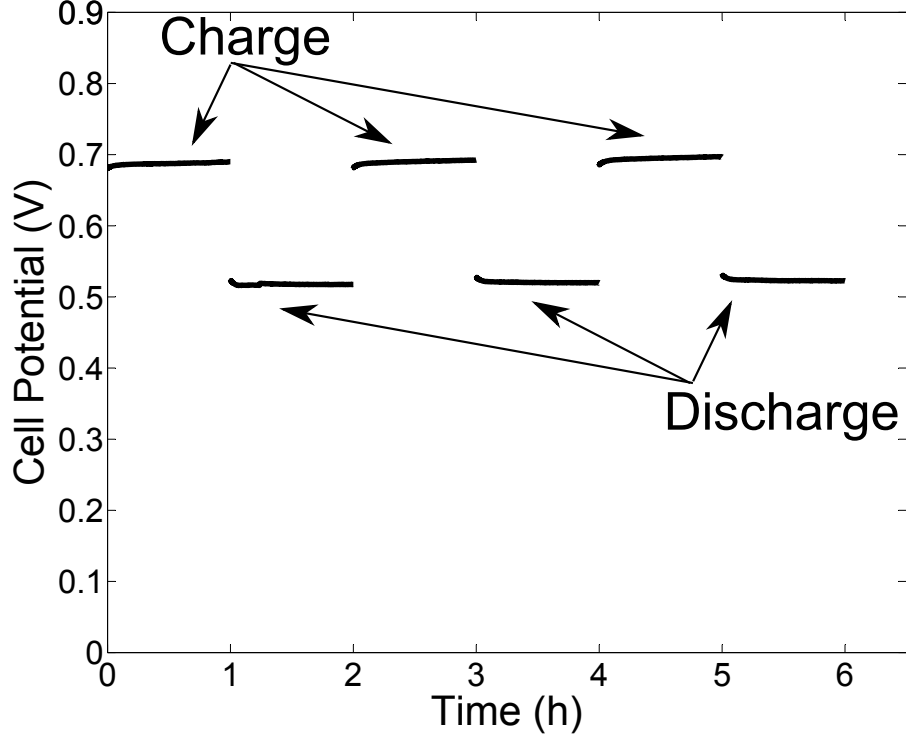
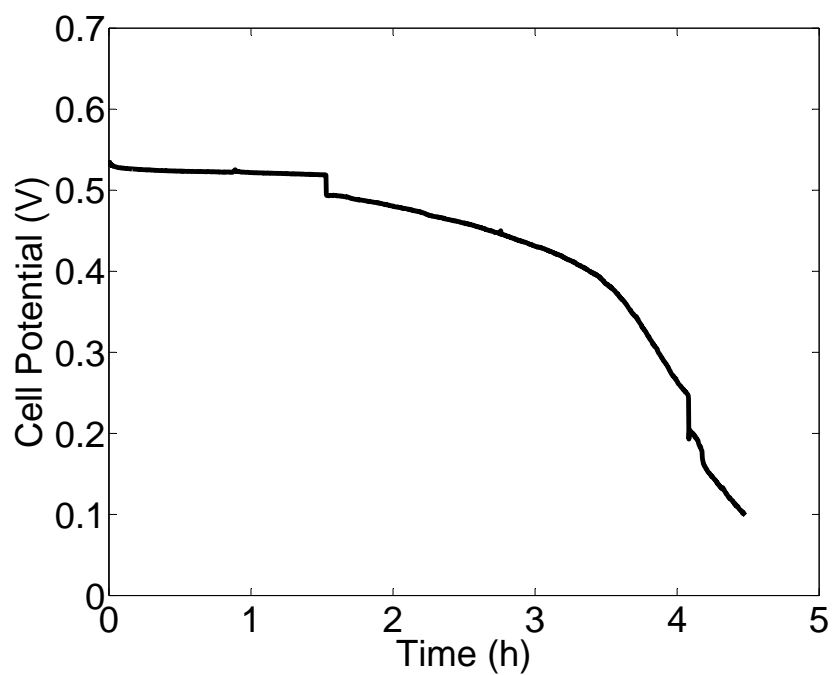


Figure 3.6: Charge/discharge characteristics of the iodide-polysulfide redox battery using parameters of Table 3.2. The charge and discharge are at 0.1 mAcm^{-2} constant current.

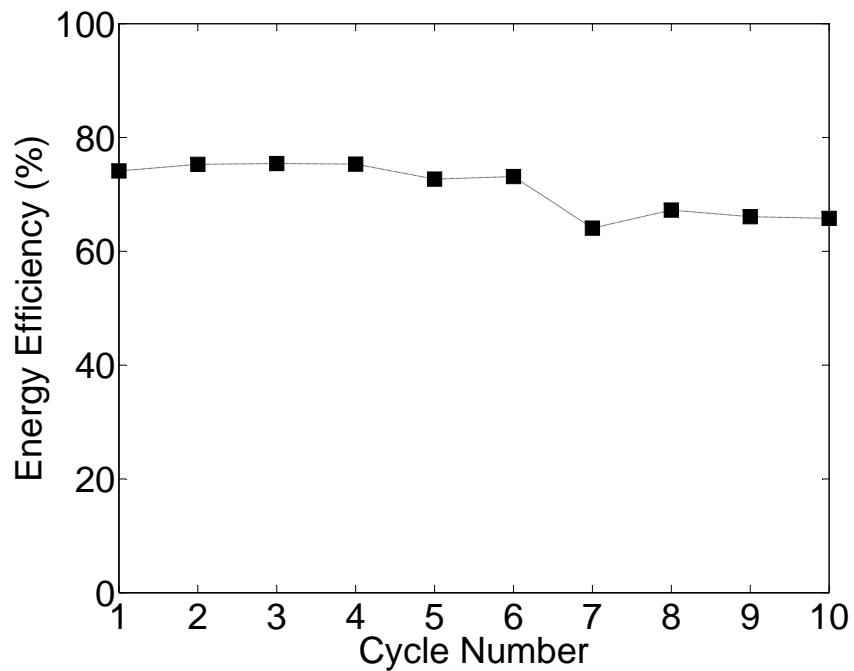
diffusion limited current ($I_{lim,b}$) is derived as a function of device parameters [77],

$$I_{lim,b} = I_{lim} \frac{1 + \frac{b}{l\epsilon_p}}{1 + 3\epsilon_p \frac{b}{l} + \frac{3}{2} \left(\frac{b}{l}\right)^2}, \quad (3.2)$$

where I_{lim} is the maximum photocurrent from cell, b is the bulk length, and l and ϵ_p are the thickness and the porosity of the porous TiO_2 layer. To minimize the mass transfer limitations, the separation length is traditionally limited to approximately $40 \mu\text{m}$, divided equally between the nanoporous photoanode and the bulk electrolyte. The current design of this work requires a much larger separation of electrodes to allow the storage of electrolytes and the membrane. The experiments have been performed with a bulk electrolyte that is $300 \mu\text{m}$ thick and a porous layer that is $15 \mu\text{m}$ thick. These values predict a current that is only $\sim 18\%$ of the maximum



(a)



(b)

Figure 3.7: (a) Complete discharge and (b) energy efficiency characteristics of the iodide-polysulfide redox battery using parameters of Table 3.2. The charge and discharge are at 0.1 mAcm^{-2} constant current.

value. This could be a limiting factor in the operation of the static SRB. However, after the implementation of the flow SRB, the current will no be diffusion limited and hence the drop of Figure 3.8a will be avoided.

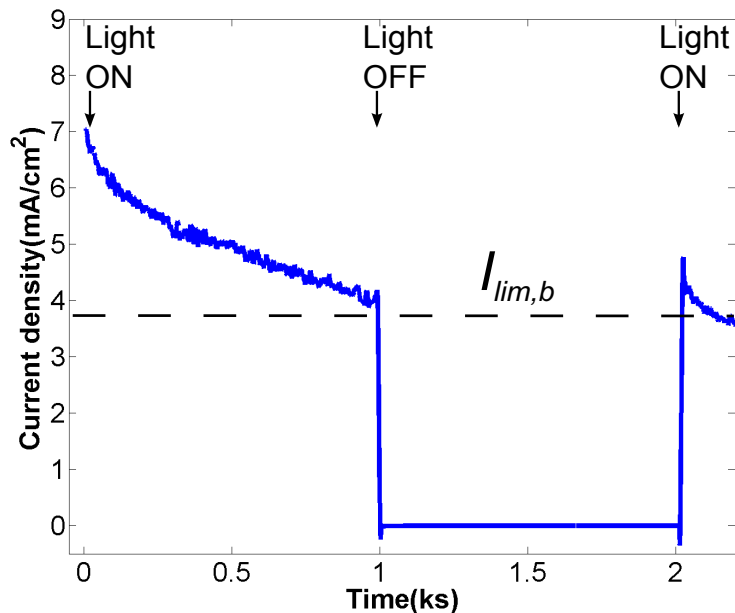
The efficiency of the DSSC is measured to be $\sim 1.7\%$. In future smaller spacings enabled by fabrication processes operating with higher tolerances should boost the efficiency by allowing a thinner bulk thickness.

Solar redox battery charge/discharge. — The solar rechargeable redox flow battery is assembled in a sandwich structure as shown in Figure 3.9 using the components demonstrated in the previous sections. The light window and the spacers openings are set to 1 cm^2 and the thickness of the spacers is set to be $300 \text{ }\mu\text{m}$.

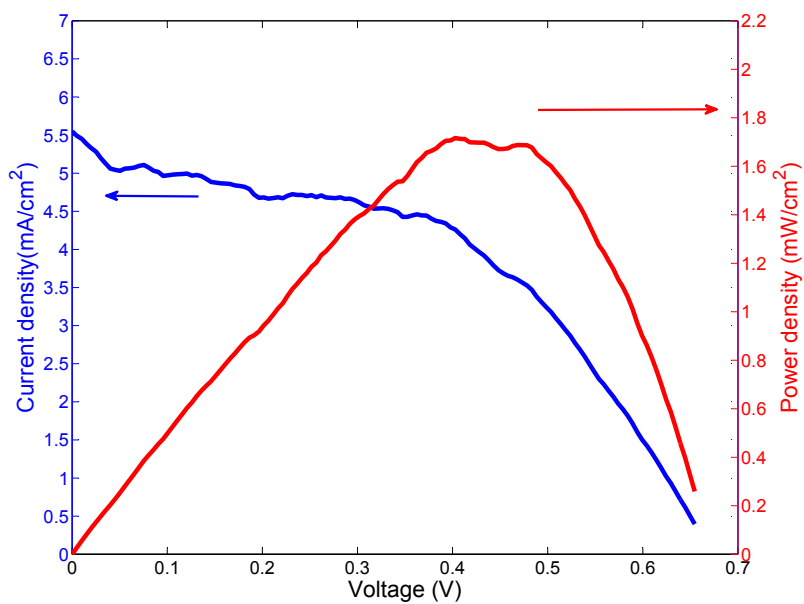
Photocharge/discharge characteristics of the SRB are shown in Figure 3.10a. The dependency of the cell potential to the discharge time can be explained by Nernst equation where the equilibrium voltage changes proportional to the logarithm of the ratio between oxidized and reduced species. The open circuit potential of the cell at each charge state should follow,

$$E_{eq} = \Delta E^0 - \frac{RT}{2F} \ln \frac{[S_4^{2-}][I^-]^3}{[S_2^{2-}]^2[I_3^-]} = \Delta E^0 - \frac{RT}{2F} \ln \frac{27(1 - SOC/3)(1 - SOC)^3}{2(SOC)^3}, \quad (3.3)$$

where ΔE^0 is the difference in the standard potentials of the two redox couples and the logarithmic term reflects the effect of ion concentration. SOC is the state of the charge and is defined as the portion of iodide ions that are in the oxidized state, $SOC = 3[I_3^-]/[I_{total}]$. For the non-equilibrium potential of the cell, the current dependent ohmic (IR_{ohmic}) and kinetic losses (η) should be considered as well, therefore $E = E_{eq} - \eta - I(R_{ohmic})$. At the onset of discharge, minute 10, the cell voltage drops instantly for 200 mV because of ohmic losses in the membrane and the electrodes. Throughout the discharge, as the SOC changes from 0.75 to 0.25 , the concentration dependent term of the voltage only decreases by 109 mV . This describes the relatively flat region in the cell voltage response. The fast drop at the end of the discharge occurs because of the large ratio of discharged species to the charged ones in the electrolyte as is



(a) Short circuit current



(b) I-V Characteristics

Figure 3.8: IV characteristics and short circuit current of DSSC using the solar-battery electrolyte (1 M I_2 , 0.1 M NaI, 1 M $NaClO_4$ in AcN/THF (2:1 v/v)). The illumination source is a 150 W Xenon lamp coupled with an AM 1.5D filter at power intensity of 100 mWcm^{-2} .

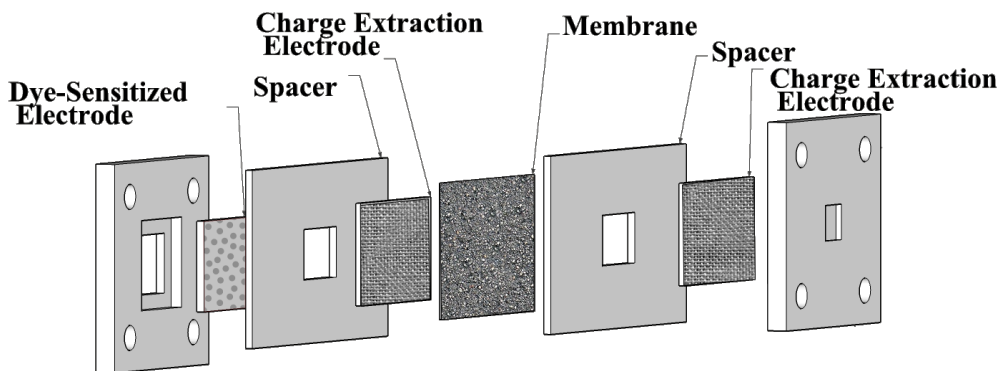


Figure 3.9: Solar redox battery sandwich structure

observed in equation 3.3. As the SOC approaches zero, the term inside the logarithm increases proportional to $1/(SOC)^3$ which translates to a fast increase in the logarithm term.

At this stage, unlike a RFB, the cell is not connected to external reservoirs. Therefore, the capacity of the battery is limited to the amount of active material in the thin half cells. The full discharge revealed a 1.2 Ah L^{-1} charge capacity which is 35 times larger than that of the previous work on solar redox flow battery by Yan *et al.* [60]. An energy density per electrode area of $52 \mu\text{Whcm}^{-2}$ is achieved which is a 13 times improvement over Yan's work. It should be noted that the theoretical capacity of Yan's solar battery is only 1 Ah L^{-1} based on single electron transfer of quinoxaline and 0.1 M concentrations of iodide and quinoxaline that have been used in that cell². Although the high solubility of quinoxaline should allow a higher capacity in a more concentrated cell, even with the current target value the measured capacity is still lower than expected. This could be because of the low surface area of the electrodes (Pt coated Ti mesh) and the incomplete electrode-electrolyte interactions.

A comparison of the results of the SRB of this work with the previous DSSC-based solar battery devices is presented in Table 3.3. It is noteworthy that even without consideration of the flow, this work presents the highest areal energy density among solar batteries. Figure 3.10b shows the cell energy efficiency, which started at more than 98% and gradually dropped to

²This value is not directly reported in [60] and is calculated based on the information given in that publication.

78% after 10 cycles mainly because of solvent loss. This should be avoided in a sealed device using common approaches in the redox flow industry. For separate PV panels and batteries, the electrical energy storage efficiency is $\sim 40\text{-}56\%$ for AC output and $\sim 49\text{-}62\%$ for DC output power [78]. Comparison of the latter value with the efficiency of this work supports our initial expectation about reduction of energy conversion losses in an integrated solar cell-battery device.

Table 3.3: Performance comparison of DSSC-based solar batteries.

Q_V^a (mAh L ⁻¹)	E_A^b (μWhcm^{-2})	Q_A^c (μAhcm^{-2})	V^d (V)	η^e (%)	Roundtrip efficiency (%)	Coulombic efficiency (%)	Ref
	9.3	76.38	0.45			80	[53]
	47	130.5	0.75			42	[54]
	31	149	0.7			36	[55]
	2.68	10.5	0.55	3.21		30	[56]
	0.1	0.3	0.68	0.1			[79]
	21	54	0.75	6.10	84	~ 100	[57]
32.9	3.5	8.3	0.6				[60]
1.2×10^3	52	99	0.6	1.7	78	~ 100	This work

^a Volumetric discharge capacity.

^b Areal energy density.

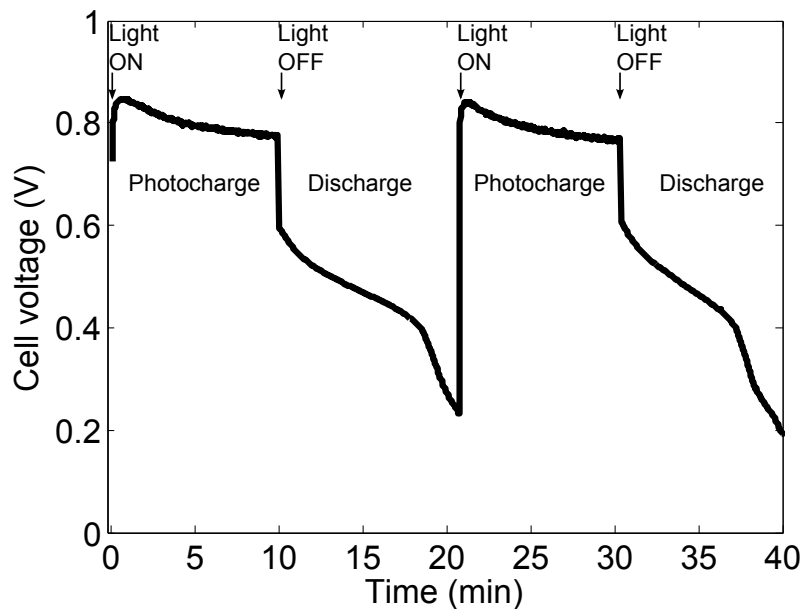
^c Areal discharge density.

^d Initial discharge voltage.

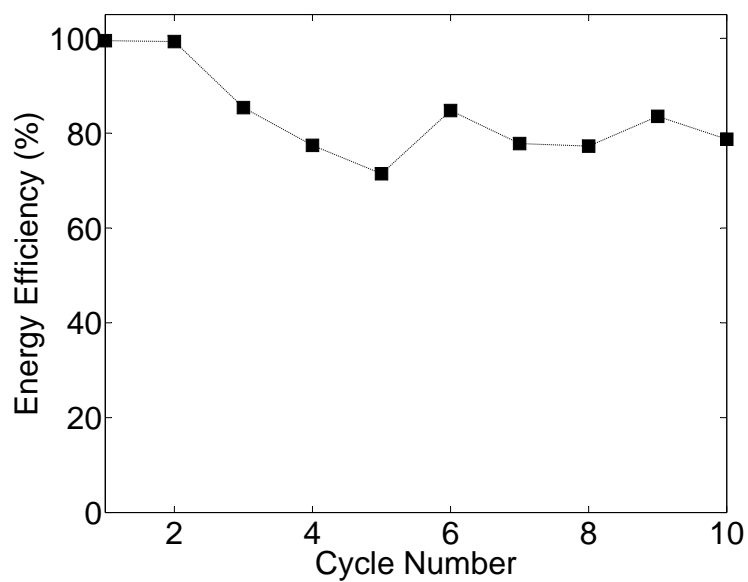
^e Photo-conversion efficiency.

3.4 Conclusion

A solar rechargeable redox battery is demonstrated. A set of materials is proposed for achieving an efficient device and the device is demonstrated. It shows the highest performance yet achieved in any integrated DSSC-based energy storage device. Significant improvement in the areal and volumetric capacity is observed compared to the only other combined solar rechargeable redox battery demonstrated to date. The tests suggest the cell-thickness dependency of DSSC performance as the main factor limiting performance. This effect will be greatly depreciated in a flow cell when the supply of iodide to the photoelectrode is provided by convection



(a)



(b)

Figure 3.10: (a)Photocharge/ Discharge of the solar redox battery. (b)Energy efficiency during charge/discharge cycles. For charging the photoelectrode and anode are directly connected and the discharging is through a 1 k Ω resistor between the two discharge electrodes.

from external sources rather than diffusion. Further improvement of the photoelectrode, membrane and current collecting electrodes should result in more efficient performance.

Suggested future work is described in Chapter 4, following is a detailed description of the experimental procedure.

3.5 Experimental

Electrochemical cell preparations.— Sodium sulfide nonahydrate, ($\text{Na}_2\text{S} \cdot 9\text{H}_2\text{O}$, 98.0 %), sulfur, sublimed (S, 99.5.0%), iodine, resublimed (I_2 , 99.5.0%), sodium iodide (NaI), sodium hydroxide pellets (NaOH, 97%) are purchased from Fisher Scientific. Sodium perchlorate (NaClO_4 , 98%), acetonitrile anhydrous (CH_3CN , 99.8%) are supplied from Sigma Aldrich. Tetrahydrofuran ($\text{C}_4\text{H}_8\text{O}$, 99.99%) is obtained from EMD Millipore Chemicals. Nickel Foam (Ni) is purchased readily from MTI Corporation. Ion exchange membrane of CMI-7000 is supplied by Membrane International.

The conductive glass of the sensitized electrode is fluorine doped tin oxide coated with resistance of $8\ \Omega/\text{sq}$ and is purchased from Solaronix. The sensitizing dye, Ruthenizer 535 bis-TBA dye (N719) is purchased from Dyesol.

The electrochemical glassware is washed with 2 % Extran 3000 in water solution followed sonication in ethyl alcohol and acetone. The aqueous experiments are performed using deionized (DI) water, purified with a Milipore water system.

The DSSC/positive half-cell electrolyte is prepared by dissolving appropriate weights of materials for a 1 M NaI, 0.1 M I_2 and 1 M NaClO_4 solution in AcN/THF (2:1 v/v). The mixture is stirred for 2 h.

In order to prepare the negative electrolyte, first 3 M sodium sulfide is dissolved in THF by stirring and warming the solution to $40\ ^\circ\text{C}$. Sulfur is then added in three times the concentration of Na_2S . The mixture is heated to $50\ ^\circ\text{C}$ and stirred at 400 RPM for 2 h before it changes color from a light yellow to brownish red. The color change process of polysulfide solution is shown in Figure 3.11. After a uniform solution is achieved, additional solvent is added to maintain 3

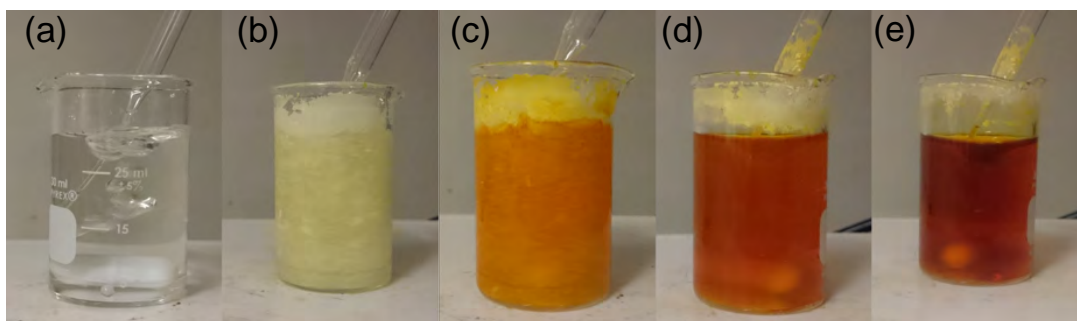


Figure 3.11: Color change of sodium sulfide as it changes from colorless Na_2S (a) to dark red Na_2S_4 (e).

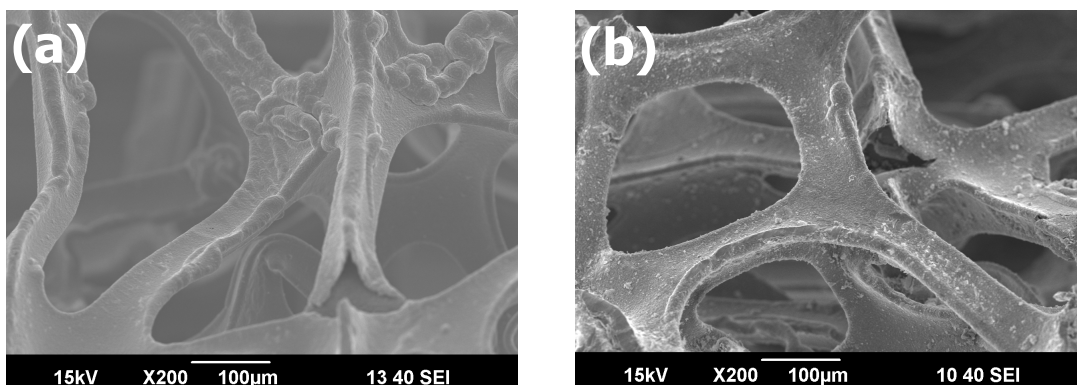


Figure 3.12: SEM images of the nickel foam before (a), and after treatment with acid and polysulfide (b).

M solution on Na_2S_4 . Then (NaClO_4) is added in 3 M concentration. Finally, the solution is diluted with AcN to produce a 1 M solution of Na_2S_4 in AcN/THF (2:1 v/v).

The pre-treated Ni foam electrode are prepared by first immersing a piece of Ni foam in a clean (1:1 v/v) sulfuric acid/water solution for 4 min. After rinsing with DI water, the electrode is boiled in DI water for 1 min and then is boiled in 1 M aqueous solution of Na_2S_4 (prepared similar to the negative half-cell electrolyte) for 2 h. The electrodes are boiled in DI water for another 1 min and then dried under vacuum at 60°C . SEM images of the fresh and activated Ni foam are shown in Figure 3.12. NiS layer is shown as clusters on the smooth surface of Ni.

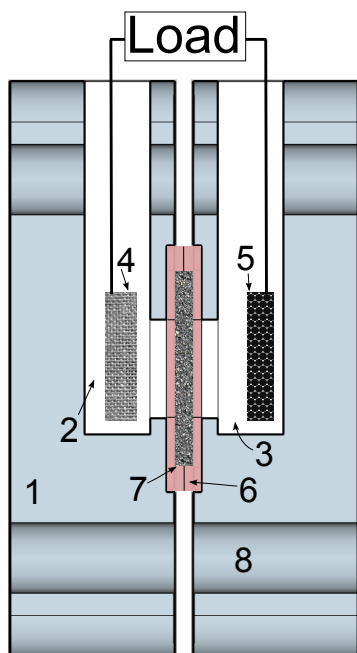
In order to adjust the membrane for the non-aqueous solvent, it is immersed in 1 M Na_2ClO_4 in AcN/THF (2:1 v/v). The container is then held under vacuum to enforce the substitution of air with the solvent. The membranes is then stored in the same electrolyte for 24 h. An EIS study of the membranes showed an ionic resistance of $240 \Omega/\text{cm}^2$. Another CEM from Fu-

matech GmbH (FKB PK130) is also tested because of previous reports on its application in non-aqueous RFBs [80]. The latter, however, showed a much higher ionic resistance in the solvent in this work (AcN/THF (2:1 v/v)) compared to CMI-7000 which is used in these experiments.

For the photoelectrode, the technique explained by Ito *et al.* [81] is followed for most of the electrode preparation. First, two holes are drilled in FTO coated glass electrodes using two sacrificial glass layers on top and bottom to avoid chipping the glass surface during the drilling. Then the FTO coated glass electrodes are cleaned in a sonicator bath using a 2 % Extran 3000 solution in DI water. Then the electrodes are rinsed with ethanol and DI water and treated under a UV lamp (Mineralight UVS-54,UVP, LLC) for 18 min. A thin layer of TiO_2 is deposited on the FTO surface by immersing the electrodes in 40 mM aqueous solution of TiCl_4 kept at 70°C and stirred on a hot plate. After 30 min, 15 μm of TiO_2 paste is doctor bladed over the FTO coated glass followed by an ethanol-vapor bath treatment for 3 min. The electrodes are slowly heated to 400°C on a hot plate at $2.5^\circ\text{C}/\text{min}$ until became transparent. After another TiCl_4 treatment for 30 min, the electrodes are heated again at 400°C for 30 min. The cooled electrodes are sensitized in 0.2 mM solution of N719 in ethanol for 24 h.

Electrochemical and Photoelectrochemical measurements. — All the cyclic voltametries and I-V characteristics are carried out using a PGSTAT101 Autolab potentiostat in a 2 electrode setup. The redox battery is tested in a H-type cell as depicted in Figure 3.13. The SRB is tested in the sandwich cell of Figure 3.9. For charging, the photoelectrode and anode are directly connected while the discharging happened through a $1\text{ k}\Omega$ resistor between two discharge electrodes.

The light source is a Newport 150 W Xenon arc lamp coupled to a filter (AM 1.5D), driven by a Newport 69907 power supply (Newport Inc., Irvine CA). The output power is measured using a Newport 818-SL photodetector and is adjusted at 100 mWcm^{-2} . The setup for photoelectrochemical experiments is shown in Figure 3.14.

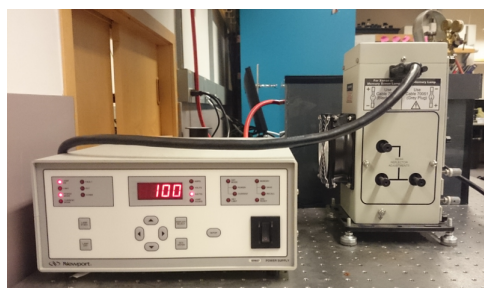


(a) Schematic of the H-type cell

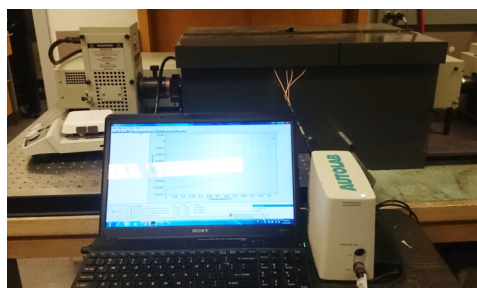


(b) Image of the redox battery

Figure 3.13: Schematic (a) and the image (b) of the H-type cell used for the battery test. The parts are marked as: body(1), half cells (2,3), Pt mesh cathode (4), Ni foam anode (5), silicone sealant (6), ion exchange membrane (7) and the screw housing(8).



(a)



(b)

Figure 3.14: Images of the (a) light source and (b) the potentiostat setup.

Chapter 4

Conclusions and Future Work

The main conclusions and contributions derived from this work are summarized in this chapter. The approaches to explore the presented devices further are introduced next.

4.1 Conclusions

Widespread application of renewable energy sources faces challenges including the high cost of external storage systems needed to for grid stability. Investigation of new materials for more efficient, less expensive solar cells and batteries is an important avenue to overcome the storage challenge. Optimization, redesign and reconfiguration of existing technologies is another approach. This work follows the latter path, demonstrating two novel configurations of solar energy conversion and storage devices.

The vertical photogalvanic cells (VPGCs) developed in the course of this thesis work overcome challenges associated with traditional photogalvanic cells. In these devices improvement in performance is suggested by having light travel into the device parallel to electrodes rather than perpendicular (and through a transparent electrode). This has several advantages including higher efficiency and device compatibility with less soluble dyes and electrodes with slower kinetics. They may be effective as cheap, low maintenance solar cells upon realization of the now-less-demanding electrode-dye-mediator-electrode combination. It is unlikely though, that

the storage promise of photogalvanic cells will be fulfilled due to the high bulk recombination tendency of energy elevated species.

The integrated solar redox battery (SRB) of this work shows that higher solar energy storage yields are achievable with a combined device compared to a system composed of separate solar cells and batteries. Novelty is in the structure, with a redox battery combined with a dye-sensitized solar cell. Although another example of such an integrated cell was reported during the course of this thesis work, its performance is limited. Here, with careful consideration of the electrodes and redox couples, we are able to show a capacity of 1.2 Ah L^{-1} . For the non-flow system of this work, the integration does not severely affect the storage capacity of the battery but the photo conversion performance is inferior compared to a standalone dye sensitized solar cell. This difficulty is rooted in diffusion of the species in the electrolyte and may be overcome by the convection in a flow configuration.

Having a grid scale facility of solar redox battery causes important safety concerns. The large reservoirs of organic solvents are health hazards since acetonitrile and tetrahydrofuran have health hazard rating of 2 (could cause temporary incapacitation). Both have a flammability rating of 3 and can be ignited even at low temperatures. These issues mean the assembly of these devices is more costly than aqueous RFBs because of more expensive fabrication procedure and more costly packaging materials. Research in the aqueous DSSCs is constantly improving the performance of such devices [82–86]. A safer solar-redox battery could use aqueous solvents in both half cells - upon the realization of the water-based solar cells.

Another difficulty in the development of SRBs is maintaining the flow over a large number of solar-batteries. These devices should be installed in a solar farm and all the electronic and fluidic parts should be connected. It is unlikely that the electrolyte flow could be maintained in hundreds of panel using a centralized pumping station. Therefore a distributed pumping system should be designed which further increases the cost of SRBs compared to RFBs.

The advantages of the integration, namely saving on the amount of cell material and fabrication steps as well as higher storage yield, should be compared to the limitations due to more

complex design of the whole system and potential safety concerns before this technology is considered for commercial applications.

4.2 Contributions

In Chapter 2, a vertical configuration for photogalvanic cells (PGCs) is proposed and analyzed for the first time. In the new structure light absorption and hence electron generation is spread through the depth of the device. All the incoming photons can be captured effectively even with low solubility dyes by adjusting the depth according to the dye concentration. Because of the distributed electron generation, unreasonably fast electrode kinetics are no longer required. To be efficient, the new structure requires 100 times slower electrode kinetics than conventional PGC designs. The optimum dye concentration in conventional PGCs is ~ 100 mM which is relaxed by 3 orders of magnitudes in the proposed design. Therefore two major challenges in fabrication of efficient PGCs as cheap, low maintenance solar cells are removed.

The effect of device bulk recombination rate, electrode kinetic rate constant, electrode selectivity and device geometry are studied for the vertical photogalvanic cells and optimum values are listed as a guideline for future experimental work.

Chapter 3 describes the work on solar cell-redox flow battery integration in a solar redox battery (SRB) device. The aim of the system is ultimately to offer savings on materials, fabrication and installation costs compared to two separate devices. Most solar batteries to date employ solid electrodes, while in the SRB the storage capacity can be scaled by increasing the size of the electrolyte reservoir. The integration of a combination of a dye-sensitized solar cell and a redox flow battery was recently reported for the first time by Yan *et al.* [59, 60], using lithium tungsten oxide (Li_2WO_4) and then quinoxaline electrolytes. The work of this thesis demonstrates dramatically improved cell performance through the careful consideration and selection of electrolytes, electrodes and cell geometry. A material set for the solar battery system is proposed that results in the highest storage and efficiency reported for a solar-battery. The charge density of the proposed solar battery is measured to be 1.2 Ah L^{-1} which is 35

times larger than the work by Yan *et al.* [60]. The areal energy density per electrode area of $47 \mu\text{Whcm}^{-2}$ is achieved which is a 13 times improvement over the previous work. The reason for this improvement is the combination of higher theoretical capacity of the electrolyte and higher kinetic rates of electrodes. These properties offer hope for scalability of the technology, as discussed in future work section below.

Even without the consideration of scalability offered by using flow (which still remains to be implemented) and only comparing the capacity of the conversion cell, this work still presents the highest areal energy density among solar batteries, exceeding the best performance to date, reported by Murakamiet *et al.* [54].

4.3 Future Work

The vertical photogalvanic cell proposed in this work removed several obstacles from realization of an efficient PGC, namely, the requirement of very fast electrode kinetics and highly soluble dyes. Work still needs to be done to satisfy other unfulfilled aspects, particularly the selective electrode. Initial research on semiconductor electrochemistry showed their potential for this role as briefly explained in Appendix B [49, 87]. However, the behavior of the semiconductor-liquid interface varies significantly with crystallinity, doping and surface finish. One aspect to expand this work in to explore a large variety of wide band gap semiconductors for employment in VPGCs.

So far the best selectivity achieved using semiconducting electrodes is 1000 [49], and similar values are obtained using selective self-assembled monolayers¹. This selectivity needs to be increased by a factor of 1000 to make these cells truly effective.

The effect of optical properties of the electrodes on the performance of the device could be studied as an extension to the current model. While a reflective surface would not alter the results significantly, the absorbing properties of the semiconducting electrodes result in a mixed photoelectrochemical-photogalvanic mechanism for electricity generation.

¹unpublished work by Dr. Joanna Slota-Newson

Although careful considerations are taken for the design of the solar redox battery of this work, there still exist some aspects that can benefit from more in depth analysis. One major limitation of DSSC-based solar batteries is the inverse relationship between electrode spacing and photo-conversion efficiency of the cell. Solar batteries with one solid state half cell solely rely on the capacity of redox mediators in the photosensitive half cell and therefore require large spacing between electrodes for any significant storage to be achieved. This bulk size can reduce the photo-current efficiency as explained by Papageorgiou *et al.* [77]. The mass transfer limited current of a DSSC results from the lag in back transfer of reduced mediators from the counter electrode. However, the adverse effect could be much weaker than the prediction of equation (3.2) due to the thermal convection in bulk of the device.

The redox flow system of this work also requires some extra spacing compared to a DSSC to make room for electrolyte flow. Therefore, analysis of this mass transfer is vital for improvement of these devices. In fact, the photo-charging operation of the solar redox battery is slightly different from the photo conversion of DSSCs and this limitation might not be directly applicable. In the solar redox battery the regeneration of the dyes happens as a result of their reduction with always-freshly-provided mediators from external reservoirs and is not limited to the diffusion of the recycled mediators from the counter electrode as in a DSSC. Therefore, it is believed that this limitation could be alleviated by a flow of the electrolyte tuned to the consumption rate of redox species at the photo-electrode.

A numerical analysis of the solar redox battery could clarify this issue. Such model could be implemented in COMSOL MULTIPHYSICS software as a follow up project of this work.

The flow rate of the electrolytes should be adjusted with respect to the light intensity, so that the redox species efficiently capture the photo-generated charges. This is similar to the maximum power point tracking (MPPT) system used in separate solar panel-battery systems. The optimum flow rate at each light intensity and the control mechanism of this rate can also be studied in the complete cell model. The numerical analysis also gives guidelines for optimum cell geometry and electrolyte parameters.

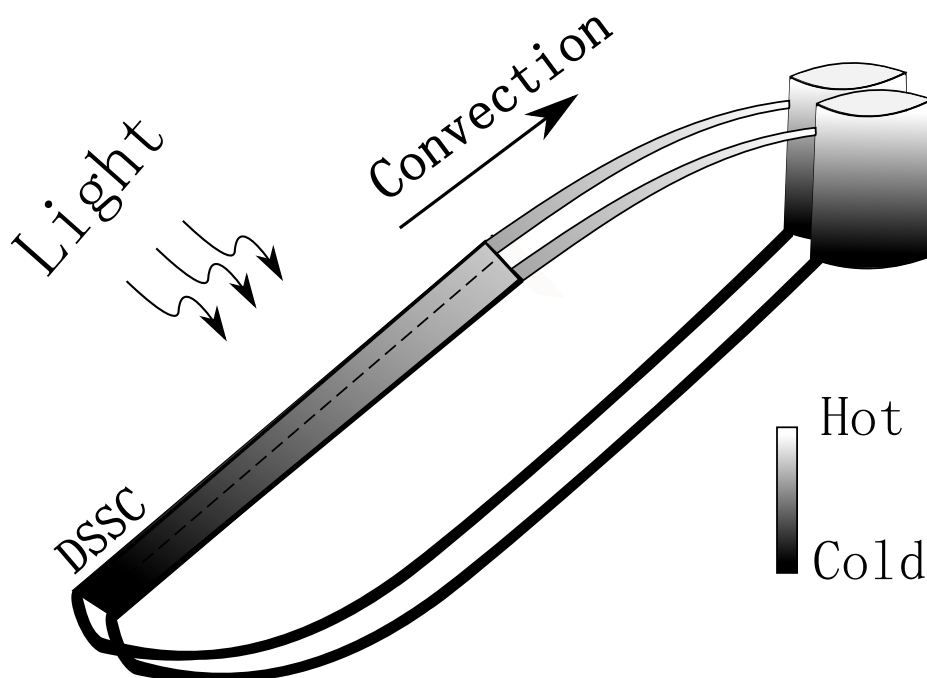


Figure 4.1: Utilization of thermal convection for electrolyte circulation in solar redox batteries.

Using solar thermosiphon effect to enhance ion circulation is one way to increase the utilization of solar energy by reducing the need for pumping. This way thermal convection of the electrolyte is used to flow the ions to the tanks as is depicted in Figure 4.1. Because of the lack of control over the flow rate, a lower efficiency is expected and this method should be limited to a trimmed-down version of the device where simplicity has priority over performance. The feasibility and cost effectiveness of this method can also be evaluated through the numerical model.

Development of organic materials as active redox couples could significantly add to the flexibility of the solar battery since normally fine tuning of electrochemical potentials is possible through the synthesis of organic materials. Such an approach has been shown very effective in RFBs [88]. Therefore, synthesis and incorporation of organic redox couples for SRBs is another aspect of this work that can be expanded with collaboration of a synthetic chemistry group.

The round-trip energy efficiency of the device could be further enhanced by reducing potential drops in the device. One major source of such loss is the potential drop over the membrane. High ionic conductivity membranes should be developed based on the charge balancing ions, active species and the electrolyte solvent used in the design of SRB.

Stability of dye-based devices is currently under research by several groups. While some of the most commonly used dyes like N749 and N719 lack long term stability under illumination or high temperatures, there are other stable dyes such as Z907, K19 and K77 at 80 °C in dark and at 60 °C under illumination[89]. These properties should be investigated for the utilized dyes in the electrolyte selected for the VPG or SRB devices. Such studies are vital before any movement towards the commercialization.

Bibliography

- [1] *Energy Technology Perspectives 2014: Harnessing Electricity's Potential*. International Energy Agency, May 2014. → pages 2
- [2] “Human development index (HDI),” UNITED NATIONS DEVELOPMENT PROGRAMME, Tech. Rep., May 2014. → pages 2
- [3] *Key World Energy Statistics*. International Energy Agency, 2014. → pages 2
- [4] T. R. Cook, D. K. Dogutan, S. Y. Reece, Y. Surendranath, T. S. Teets, and D. G. Nocera, “Solar energy supply and storage for the legacy and nonlegacy worlds,” *Chemical Reviews*, vol. 110, no. 11, pp. 6474–6502, Nov. 2010. → pages 2
- [5] N. S. Lewis, “Powering the planet,” *MRS Bulletin*, vol. 32, no. 10, pp. 808–820, 2007. → pages 3, 42
- [6] C. Schroder, “Instability in power grid comes at high cost for german industry,” *Spiegel Online*, Aug. 2012. <http://www.spiegel.de/international/germany/instability-in-power-grid-comes-at-high-cost-for-german-industry-a-850419.html>[Accessed:2015-02-01] → pages 3
- [7] P. Denholm and M. Hand, “Grid flexibility and storage required to achieve very high penetration of variable renewable electricity,” *Energy Policy*, vol. 39, no. 3, pp. 1817–1830, Mar. 2011. → pages 3
- [8] A. A. Akhil, G. Huff, A. B. Currier, B. C. Kaun, D. M. Rastler, S. B. Chen, A. L. Cotter, D. T. Bradshaw, and W. D. Gauntlett, “DOE/EPRI 2013 electricity storage handbook in collaboration with NRECA,” Sandia National Laboratories, SANDIA REPORT, Jul. 2013. → pages 4, 90
- [9] B. Dunn, H. Kamath, and J.-M. Tarascon, “Electrical energy storage for the grid: A battery of choices,” *Science*, vol. 334, no. 6058, pp. 928–935, Nov. 2011. → pages 4, 5
- [10] W. F. Pickard, N. J. Hansing, and A. Q. Shen, “Can large-scale advanced-adiabatic compressed air energy storage be justified economically in an age of sustainable energy?” *Journal of Renewable and Sustainable Energy*, vol. 1, no. 3, p. 033102, May 2009. → pages 5

- [11] “World premiere: the first industrial-scale power-to-gas plant,” Oct. 2013.
http://www.audi.com/com/brand/en/vorsprung_durch_technik/content/2013/10/energy-turnaround-in-the-tank.html[Accessed:2015-02-01] → pages 5
- [12] B. Zakeri and S. Syri, “Electrical energy storage systems: A comparative life cycle cost analysis,” *Renewable and Sustainable Energy Reviews*, vol. 42, pp. 569–596, Feb. 2015.
 → pages 5, 13
- [13] P. Alotto, M. Guarnieri, and F. Moro, “Redox flow batteries for the storage of renewable energy: A review,” *Renewable and Sustainable Energy Reviews*, vol. 29, pp. 325–335, Apr. 2014. → pages 5, 13, 45
- [14] A. Takshi, J. D. Madden, A. Mahmoudzadeh, R. Saer, and J. T. Beatty, “A photovoltaic device using an electrolyte containing photosynthetic reaction centers,” *Energies*, vol. 3, no. 11, pp. 1721–1727, Oct. 2010. → pages 6
- [15] A. Mahmoudzadeh, R. Saer, D. Jun, S. M. Mirvakili, A. Takshi, B. Iranpour, E. Ouellet, E. T. Lagally, J. D. W. Madden, and J. T. Beatty, “Photocurrent generation by direct electron transfer using photosynthetic reaction centres,” *Smart Materials and Structures*, vol. 20, p. 094019, Sep. 2011. → pages
- [16] S. M. Mirvakili, J. E. Slota, A. R. Usgaocar, A. Mahmoudzadeh, D. Jun, M. N. Mirvakili, J. T. Beatty, and J. D. W. Madden, “Photoactive electrodes incorporating electrosprayed bacterial reaction centers,” *Advanced Functional Materials*, vol. 24, no. 30, pp. 4789–4794, Aug. 2014. → pages 6
- [17] G. Feher, J. P. Allen, M. Y. Okamura, and D. C. Rees, “Structure and function of bacterial photosynthetic reaction centres,” *Nature*, vol. 339, no. 6220, pp. 111–116, May 1989. → pages 6
- [18] W. J. Albery and M. D. Archer, “Photogalvanic cells: Part 3. the maximum power obtainable from a thin layer photogalvanic concentration cell with identical electrodes,” *Journal of Electroanalytical Chemistry and Interfacial Electrochemistry*, vol. 86, no. 1, pp. 1–18, Jan. 1978. → pages 9, 20, 22, 25
- [19] M. K. Bhimwal and K. Gangotri, “A comparative study on the performance of photogalvanic cells with different photosensitizers for solar energy conversion and storage: D-xylose-NaLS systems,” *Energy*, vol. 36, no. 2, pp. 1324–1331, Feb. 2011. → pages 9, 20, 34
- [20] K. R. Genwa, A. Kumar, and A. Sonel, “Photogalvanic solar energy conversion: Study with photosensitizers toluidine blue and malachite green in presence of NaLS,” *Applied Energy*, vol. 86, no. 9, pp. 1431–1436, Sep. 2009. → pages 9
- [21] K. Genwa and M. Genwa, “Photogalvanic cell: A new approach for green and sustainable chemistry,” *Solar Energy Materials and Solar Cells*, vol. 92, no. 5, pp. 522–529, May 2008. → pages 9, 20

- [22] K. Gangotri and V. Indora, "Studies in the photogalvanic effect in mixed reductants system for solar energy conversion and storage: Dextrose and ethylenediaminetetraacetic acidAzur a system," *Solar Energy*, vol. 84, no. 2, pp. 271–276, Feb. 2010. → pages 9, 20
- [23] V. Viswanathan, A. Crawford, D. Stephenson, S. Kim, W. Wang, B. Li, G. Coffey, E. Thomsen, G. Graff, P. Balducci, M. Kintner-Meyer, and V. Sprenkle, "Cost and performance model for redox flow batteries," *Journal of Power Sources*, vol. 247, pp. 1040–1051, Feb. 2014. → pages 13
- [24] M. Gratzel, "Photoelectrochemical cells," *Nature*, vol. 414, no. 6861, pp. 338–344, Nov. 2001. → pages 14
- [25] H. Gerischer, M. Michel-Beyerle, F. Reberstrost, and H. Tributsch, "Sensitization of charge injection into semiconductors with large band gap," *Electrochimica Acta*, vol. 13, no. 6, pp. 1509–1515, Jun. 1968. → pages 14, 20
- [26] B. O'Regan and M. Gratzel, "A low-cost, high-efficiency solar cell based on dye-sensitized colloidal TiO₂ films," *Nature*, vol. 353, no. 6346, pp. 737–740, Oct. 1991. → pages 14, 20
- [27] N. R. Neale, N. Kopidakis, J. van de Lagemaat, M. Grtzel, and A. J. Frank, "Effect of a coadsorbent on the performance of dye-sensitized TiO₂ solar cells: shielding versus band-edge movement," *The Journal of Physical Chemistry B*, vol. 109, no. 49, pp. 23 183–23 189, Nov. 2005. → pages 14
- [28] A. Z. Weber, M. M. Mench, J. P. Meyers, P. N. Ross, J. T. Gostick, and Q. Liu, "Redox flow batteries: a review," *Journal of Applied Electrochemistry*, vol. 41, no. 10, pp. 1137–1164, Oct. 2011. → pages 15
- [29] E. K. Rideal and D. C. Williams, "Photogalvanic effect," *J. Chem. Soc*, vol. 127, p. 258, 1925. → pages 20
- [30] E. Rabinowitch, "The photogalvanic effect i. the photochemical properties of the thionine-iron system," *The Journal of Chemical Physics*, vol. 8, p. 551, 1940. → pages 20
- [31] R. Gomer, "Photogalvanic cells," *Electrochimica Acta*, vol. 20, no. 1, pp. 13–20, Jan. 1975. → pages 20, 83
- [32] W. John Albery and A. W. Foulds, "Photogalvanic cells," *Journal of Photochemistry*, vol. 10, no. 1, pp. 41–57, 1979. → pages 21, 23, 24, 35, 83
- [33] T. Sakata, Y. Suda, J. Tanaka, and H. Tsubomura, "Photogalvanic effect in the thionine-iron system," *The Journal of Physical Chemistry*, vol. 81, no. 6, pp. 537–542, Mar. 1977. → pages
- [34] Y. Suda, Y. Shimoura, T. Sakata, and H. Tsubomura, "Photogalvanic effect in the thionine-iron system at semiconductor electrodes," *The Journal of Physical Chemistry*, vol. 82, no. 3, pp. 268–271, Feb. 1978. → pages

- [35] M. I. C. Ferreira and A. Harriman, "Photoredox reactions of thionine," *Journal of the Chemical Society, Faraday Transactions 1: Physical Chemistry in Condensed Phases*, vol. 73, pp. 1085–1092, Jan. 1977. → pages 20
- [36] H. Gerischer, "Electrochemical behavior of semiconductors under illumination," *Journal of The Electrochemical Society*, vol. 113, no. 11, pp. 1174–1182, Jan. 1966. → pages 20
- [37] A. J. Nozik, "Photoelectrochemistry: Applications to solar energy conversion," *Annual Review of Physical Chemistry*, vol. 29, no. 1, pp. 189–222, Oct. 1978. → pages 20
- [38] M. Gratzel, *Energy Resources through Photochemistry and Catalysis*. Elsevier, Oct. 1983. → pages 20
- [39] E. J. J. Groenen, M. S. De Groot, R. De Ruiter, and N. De Wit, "Triton x-100 micelles in the ferrous/thionine photogalvanic cell," *The Journal of Physical Chemistry*, vol. 88, no. 7, pp. 1449–1454, Mar. 1984. → pages 20
- [40] K. Gangotri, O. P. Regar, C. Lal, P. Kalla, K. R. Genwa, and R. Meena, "Use of tergitol-7 in photogalvanic cell for solar energy conversion and storage: Toluidine blue-glucose system," *International Journal of Energy Research*, vol. 20, no. 7, pp. 581–585, 1996. → pages 20
- [41] K. M. Gangotri and O. P. Regar, "Use of azine dye as a photosensitizer in solar cells: different reductant-safranin systems," *International Journal of Energy Research*, vol. 21, no. 14, pp. 1345–1350, 1997. → pages
- [42] K. M. Gangotri and C. Lal, "Studies in photogalvanic effect and mixed dyes system: EDTA-methylene blue + toluidine blue system," *International Journal of Energy Research*, vol. 24, no. 4, pp. 365–371, 2000. → pages 20
- [43] K. R. Genwa and N. C. Khatri, "Comparative study of photosensitizing dyes in photogalvanic cells for solar energy conversion and storage: Brij-35-Diethylenetriamine pentaacetic acid (DTPA) system," *Energy & Fuels*, vol. 23, no. 2, pp. 1024–1031, Feb. 2009. → pages 20
- [44] C. Lal, "Use of mixed dyes in a photogalvanic cell for solar energy conversion and storage: EDTA-thionine-azur-B system," *Journal of Power Sources*, vol. 164, no. 2, pp. 926–930, Feb. 2007. → pages 20, 52
- [45] R. A. Marcus, "On the theory of Electron Transfer reactions. VI. unified treatment for homogeneous and electrode reactions," *The Journal of Chemical Physics*, vol. 43, no. 2, pp. 679–701, Jul. 1965. → pages 24, 34
- [46] W. J. Albery, "Development of photogalvanic cells for solar energy conservation," *Accounts of Chemical Research*, vol. 15, no. 5, pp. 142–148, May 1982. → pages 24, 34, 35
- [47] A. J. Bard and L. R. Faulkner, *Electrochemical methods: fundamentals and applications*. New York: Wiley, 2001. → pages 33

- [48] W. John Albery and M. D. Archer, "Photogalvanic cells: Part 4. the maximum power from a thin layer cell with differential electrode kinetics," *Journal of Electroanalytical Chemistry and Interfacial Electrochemistry*, vol. 86, no. 1, pp. 19–34, Jan. 1978. → pages 34
- [49] A. R. Usugaocar, L. Wang, A. Mahmoudzadeh, S. M. Mirvakili, J. E. Slota-Newson, J. D. Madden, J. T. Beatty, and A. Takshi, "Semiconductors as selective electrodes for bio-photovoltaic cells," *Meeting Abstracts*, vol. MA2013-01, no. 4, pp. 282–282, Mar. 2013. → pages 38, 69, 87
- [50] W. Wang, Q. Luo, B. Li, X. Wei, L. Li, and Z. Yang, "Recent progress in redox flow battery research and development," *Advanced Functional Materials*, vol. 23, no. 8, pp. 970–986, Feb. 2013. → pages 42
- [51] G. Dennler, S. Bereznev, D. Fichou, K. Holl, D. Ilic, R. Koeppel, M. Krebs, A. Labouret, C. Lungenschmied, A. Marchenko, D. Meissner, E. Mellikov, J. Mot, A. Meyer, T. Meyer, H. Neugebauer, A. pik, N. S. Sariciftci, S. Taillemite, and T. Whrle, "A self-rechargeable and flexible polymer solar battery," *Solar Energy*, vol. 81, no. 8, pp. 947–957, Aug. 2007. → pages 42
- [52] G. Wee, T. Salim, Y. M. Lam, S. G. Mhaisalkar, and M. Srinivasan, "Printable photo-supercapacitor using single-walled carbon nanotubes," *Energy & Environmental Science*, vol. 4, no. 2, pp. 413–416, Feb. 2011. → pages 42
- [53] T. Miyasaka and T. N. Murakami, "The photocapacitor: An efficient self-charging capacitor for direct storage of solar energy," *Applied Physics Letters*, vol. 85, no. 17, pp. 3932–3934, Oct. 2004. → pages 42, 43, 44, 60
- [54] T. N. Murakami, N. Kawashima, and T. Miyasaka, "A high-voltage dye-sensitized photocapacitor of a three-electrode system," *Chemical Communications*, no. 26, pp. 3346–3348, Jun. 2005. → pages 42, 44, 60, 69
- [55] Y. Saito, S. Uchida, T. Kubo, and H. Segawa, "Energy-storable dye-sensitized solar cells with tungsten oxide charge-storage electrode," *ECS Transactions*, vol. 16, no. 25, pp. 27–34, Mar. 2009. → pages 42, 43, 60
- [56] Y. Saito, A. Ogawa, S. Uchida, T. Kubo, and H. Segawa, "Energy-storable dye-sensitized solar cells with interdigitated nafion/polypyrrole comb-like electrodes," *Chemistry Letters*, vol. 39, no. 5, pp. 488–489, Apr. 2010. → pages 42, 43, 60
- [57] Z. Yang, L. Li, Y. Luo, R. He, L. Qiu, H. Lin, and H. Peng, "An integrated device for both photoelectric conversion and energy storage based on free-standing and aligned carbon nanotube film," *Journal of Materials Chemistry A*, vol. 1, no. 3, pp. 954–958, Dec. 2012. → pages 43, 60
- [58] M. Yu, X. Ren, L. Ma, and Y. Wu, "Integrating a redox-coupled dye-sensitized photoelectrode into a lithium-oxygen battery for photoassisted charging," *Nature Communications*, vol. 5, Oct. 2014. → pages 43

- [59] N. F. Yan, G. R. Li, and X. P. Gao, "Solar rechargeable redox flow battery based on $\text{Li}_2\text{WO}_4/\text{LiI}$ couples in dual-phase electrolytes," *Journal of Materials Chemistry A*, vol. 1, no. 24, pp. 7012–7015, May 2013. → pages 45, 68
- [60] N. Yan, G. R. Li, and X. Gao, "Electroactive organic compounds as anode-active materials for solar rechargeable redox flow battery in dual-phase electrolytes," *Journal of The Electrochemical Society*, vol. 161, no. 5, pp. A736–A741, Jan. 2014. → pages 45, 59, 60, 68, 69
- [61] S. Feldt, "Alternative redox couples for dye-sensitized solar cells," dissertation, Uppsala University, 2013. → pages 48, 52
- [62] "Ion selective membrane separate anolyte and catholyte," U.S. Patent US4 485 154 A, Nov., 1984. → pages 48, 49
- [63] P. M. Lessner, F. R. McLarnon, J. Winnick, and E. J. Cairns, "Aqueous polysulphide flow-through electrodes: Effects of electrocatalyst and electrolyte composition on performance," *Journal of Applied Electrochemistry*, vol. 22, no. 10, pp. 927–934, Oct. 1992. → pages 49
- [64] K. M. Abraham, R. D. Rauh, and S. B. Brummer, "A low temperature Na-S battery incorporating a soluble S cathode," *Electrochimica Acta*, vol. 23, no. 6, pp. 501–507, Jun. 1978. → pages 49
- [65] S. Licht, R. Tenne, H. Flaisher, and J. Manassen, "Cation effects on the electrochemistry of anions in polysulfide photoelectrochemical cells," *Journal of The Electrochemical Society*, vol. 133, no. 1, pp. 52–59, Jan. 1986. → pages 49
- [66] R. D. Rauh, K. M. Abraham, G. F. Pearson, J. K. Surprenant, and S. B. Brummer, "A lithium/dissolved sulfur battery with an organic electrolyte," *Journal of The Electrochemical Society*, vol. 126, no. 4, pp. 523–527, Apr. 1979. → pages 49, 52
- [67] Z. Tachan, M. Shalom, I. Hod, S. Ruhle, S. Tirosh, and A. Zaban, "PbS as a highly catalytic counter electrode for polysulfide-based quantum dot solar cells," *The Journal of Physical Chemistry C*, vol. 115, no. 13, pp. 6162–6166, Apr. 2011. → pages 49
- [68] D. V. Esposito, K. D. Dobson, B. E. McCandless, R. W. Birkmire, and J. G. Chen, "Comparative study of tungsten monocarbide and platinum as counter electrodes in polysulfide-based photoelectrochemical solar cells," *Journal of The Electrochemical Society*, vol. 156, no. 8, pp. B962–B969, Aug. 2009. → pages 49
- [69] I. E. L. Stephens, C. Ducati, and D. J. Fray, "Correlating microstructure and activity for polysulfide reduction and oxidation at WS₂ electrocatalysts," *Journal of The Electrochemical Society*, vol. 160, no. 6, pp. A757–A768, Jan. 2013. → pages 49
- [70] H. Zhou, H. Zhang, P. Zhao, and B. Yi, "A comparative study of carbon felt and activated carbon based electrodes for sodium polysulfide/bromine redox flow battery," *Electrochimica Acta*, vol. 51, no. 28, pp. 6304–6312, Sep. 2006. → pages 49

- [71] R. D. Rauh, F. S. Shuker, J. M. Marston, and S. B. Brummer, "Formation of lithium polysulfides in aprotic media," *Journal of Inorganic and Nuclear Chemistry*, vol. 39, no. 10, pp. 1761–1766, Oct. 1977. → pages 52
- [72] Y. Fu, Y. S. Su, and A. Manthiram, "Highly reversible lithium/dissolved polysulfide batteries with carbon nanotube electrodes," *Angewandte Chemie International Edition*, vol. 52, no. 27, pp. 6930–6935, Jul. 2013. → pages 52
- [73] Y. Yang, G. Zheng, and Y. Cui, "A membrane-free lithium/polysulfide semi-liquid battery for large-scale energy storage," *Energy & Environmental Science*, vol. 6, no. 5, pp. 1552–1558, Apr. 2013. → pages 52
- [74] A. Fukui, R. Komiya, R. Yamanaka, A. Islam, and L. Han, "Effect of a redox electrolyte in mixed solvents on the photovoltaic performance of a dye-sensitized solar cell," *Solar Energy Materials and Solar Cells*, vol. 90, no. 5, pp. 649–658, Mar. 2006. → pages 52
- [75] N. S. A. Manan, L. Aldous, Y. Alias, P. Murray, L. J. Yellowlees, M. C. Lagunas, and C. Hardacre, "Electrochemistry of sulfur and polysulfides in ionic liquids," *The Journal of Physical Chemistry B*, vol. 115, no. 47, pp. 13 873–13 879, Dec. 2011. → pages 53
- [76] G. Boschloo and A. Hagfeldt, "Characteristics of the iodide/triiodide redox mediator in dye-sensitized solar cells," *Accounts of Chemical Research*, vol. 42, no. 11, pp. 1819–1826, Oct. 2009. → pages 53
- [77] N. Papageorgiou, M. Gratzel, and P. P. Infelta, "On the relevance of mass transport in thin layer nanocrystalline photoelectrochemical solar cells," *Solar Energy Materials and Solar Cells*, vol. 44, no. 4, pp. 405–438, Dec. 1996. → pages 55, 70
- [78] V. C. Nelson, *Introduction to Renewable Energy*, 1st ed. Boca Raton, FL: CRC Press, Apr. 2011. → pages 60
- [79] P. Liu, H. Yang, X. Ai, G. Li, and X. Gao, "A solar rechargeable battery based on polymeric charge storage electrodes," *Electrochemistry Communications*, vol. 16, no. 1, pp. 69–72, Mar. 2012. → pages 60
- [80] S.-H. Shin, S.-H. Yun, and S.-H. Moon, "A review of current developments in non-aqueous redox flow batteries: characterization of their membranes for design perspective," *RSC Adv.*, vol. 3, pp. 9095–9116, 2013. → pages 64
- [81] S. Ito, P. Chen, P. Comte, M. K. Nazeeruddin, P. Liska, P. Pchy, and M. Grtzel, "Fabrication of screen-printing pastes from TiO₂ powders for dye-sensitised solar cells," *Progress in Photovoltaics: Research and Applications*, vol. 15, no. 7, pp. 603–612, May 2007. → pages 64
- [82] C. Law, S. C. Pathirana, X. Li, A. Y. Anderson, P. R. F. Barnes, A. Listorti, T. H. Ghaddar, and B. C. O'Regan, "Water-based electrolytes for dye-sensitized solar cells," *Advanced Materials*, vol. 22, no. 40, pp. 4505–4509, Aug. 2010. → pages 67

- [83] T. Daeneke, Y. Uemura, N. W. Duffy, A. J. Mozer, N. Koumura, U. Bach, and L. Spiccia, "Aqueous dye-sensitized solar cell electrolytes based on the ferricyanide/ferrocyanide redox couple," *Advanced Materials*, vol. 24, no. 9, pp. 1222–1225, Jan. 2012. → pages
- [84] W. Xiang, F. Huang, Y.-B. Cheng, U. Bach, and L. Spiccia, "Aqueous dye-sensitized solar cell electrolytes based on the cobalt(II)/(III) tris(bipyridine) redox couple," *Energy & Environmental Science*, vol. 6, no. 1, pp. 121–127, Dec. 2012. → pages
- [85] H. Choi, B.-S. Jeong, K. Do, M. J. Ju, K. Song, and J. Ko, "Aqueous electrolyte based dye-sensitized solar cells using organic sensitizers," *New Journal of Chemistry*, vol. 37, no. 2, pp. 329–336, Jan. 2013. → pages
- [86] V. Leandri, H. Ellis, E. Gabrielsson, L. Sun, G. Boschloo, and A. Hagfeldt, "An organic hydrophilic dye for water-based dye-sensitized solar cells," *Physical Chemistry Chemical Physics*, vol. 16, no. 37, pp. 19964–19971, Aug. 2014. → pages 67
- [87] A. Takshi, H. Yaghoubi, D. Jun, R. Saer, A. Mahmoudzadeh, J. D. Madden, and J. T. Beatty, "Application of wide band gap semiconductors to increase photocurrent in a protein-based photovoltaic device," *MRS Online Proceedings Library*, vol. 1414, pp. mrsf11-1414-hh07-01, Oct. 2010. → pages 69
- [88] B. Huskinson, M. P. Marshak, C. Suh, S. Er, M. R. Gerhardt, C. J. Galvin, X. Chen, A. Aspuru-Guzik, R. G. Gordon, and M. J. Aziz, "A metal-free organic-inorganic aqueous flow battery," *Nature*, vol. 505, no. 7482, pp. 195–198, Jan. 2014. → pages 71
- [89] M. I. Asghar, K. Miettunen, J. Halme, P. Vahermaa, M. Toivola, K. Aitola, and P. Lund, "Review of stability for advanced dye solar cells," *Energy & Environmental Science*, vol. 3, no. 4, pp. 418–426, Mar. 2010. → pages 72
- [90] H. Gerischer, "The impact of semiconductors on the concepts of electrochemistry," *Electrochimica Acta*, vol. 35, no. 11-12, pp. 1677–1699, Nov. 1990. → pages 84, 85
- [91] I. Muegge, P. X. Qi, A. J. Wand, Z. T. Chu, and A. Warshel, "The reorganization energy of cytochrome c revisited," *The Journal of Physical Chemistry B*, vol. 101, no. 5, pp. 825–836, Jan. 1997. → pages 85
- [92] "Electric power annual 2012," U.S. Energy Information Administration (EIA), Tech. Rep., Dec. 2013. → pages 90
- [93] G. Hashmi, K. Miettunen, T. Peltola, J. Halme, I. Asghar, K. Aitola, M. Toivola, and P. Lund, "Review of materials and manufacturing options for large area flexible dye solar cells," *Renewable and Sustainable Energy Reviews*, vol. 15, no. 8, pp. 3717–3732, Oct. 2011. → pages 90

Appendix A

Publications Not Included in the Thesis

Journal papers

- Mirvakili S.M, Slota J., Usgaocar A., **Mahmoudzadeh A.**, Jun D., Mirvakili M., Beatty J.T., Madden J.D.W.(2014) "*Photoactive Electrodes Incorporating Electrospayed Bacterial Reaction Centers*", *Advanced Functional Materials*, Vol 24, Issue 30, 47894794
- **Mahmoudzadeh A.**, Saer R., Jun D, Mirvakili S.M., Takshi A., Iranpour B., Ouellet E., Lagally E.T., Madden J.D.W., Beatty J.T. (2011) "*Photocurrent generation by direct electron transfer using photosynthetic reaction centres*", *Smart Materials and Structures*, vol 20, issue 9, 094019.
- Yoo D.S., **Mahmoudzadeh A.**, Fok E.C.W., Walus K., Madden J.D.W. (2011) "*Multiple time constant modelling of a printed conducting polymer electrode*", *Electrochimica Acta*. vol 56 issue 13, 47116.
- Takshi A., Madden J.D.W., **Mahmoudzadeh A.**, Saer R., Beatty J.T. (2010) "*A Photovoltaic Device Using an Electrolyte Containing Photosynthetic Reaction Centers*", *Energies* vol 3 issue 11, 1721-1727.

Presentations

- **Mahmoudzadeh A.**, Usgaocar A.R., Slota-Newson J., Wang L., Iranpour B., Jun D., Saer R., Yaghoubi H., Mirvakili S.M., Madden J.D.W., Takshi A., Beatty J.T. (2013) "*Electrical Energy from Photo-synthetic Proteins*", The 7th World Congress on Biomimetics, Artificial Muscles and Nano-Bio.
- Slota, J.E., Christensen P., Jun D. Usgaocar, A.R., **Mahmoudzadeh A.**, Wolf M.O., Beatty J.T., Madden J.D.W.(2013) "*Selective self-assembled monolayer functionalised electrodes for photogalvanic cells*", Natl. Meet. -Am. Chem. Soc., Div. Coll. 2013, 246, Coll 17.
- Usgaocar A.R., Wang L., **Mahmoudzadeh A.**, Mirvakili S.M., Slota-Newson J.E., Madden J.D., Beatty J.T., Takshi A. (2013) "*Semiconductors as Selective Electrodes for Bio-Photovoltaic Cells*", Meet Abstr.MA2013-01(4),282.

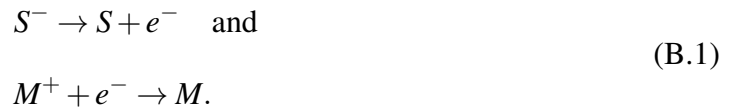
Appendix B

Semiconductors as Selective Electrodes

Electron transfer between electrode and electrolyte is the key process in any electrochemical cell. The vertical photogalvanic cell configuration needs selective electron transfer (ET) between each redox system and the corresponding electrode. This behavior is achievable with semiconducting electrodes. The theory behind this behavior is presented in this section followed by our experimental work to achieve such selectivity.

B.1 Introduction

The first part of this dissertation covers the guidelines for fabrication of an efficient photogalvanic cell. The reactions on the electrodes in a PGC are summarized at:



If both reactions happen reversibly on the two electrodes, no photovoltage is induced in the cell [32]. However, a selective electrode could result in an electrochemical potential up to $E = \Delta E^0 + \frac{RT}{F} \ln \frac{[S^-]}{[S]} \frac{[M^+]}{[M]}$ between electrodes, where ΔE^0 is the difference in standard potentials of the two redox couples [31]. The redox electrode interaction can be explained by Gerischer

model. In this model, a reduction reaction takes place by an electron transfer from an occupied state in electrode to an empty state in redox ions at a constant energy (occupied and empty states of a redox system can be interpreted as reduced and oxidized ions). As a result, the electron transfer rate is proportional to the overlap between the occupied density of energy states in solid and empty energy states of oxidants in electrolyte. A similar discussion is valid for an oxidation reaction. This process could be quantitatively evaluated which suggests a selective behavior of semiconductors towards different redox couples. The thermal fluctuation model suggests a Gaussian distribution for the redox states in an electrolyte [90] as shown in Figure B.1.

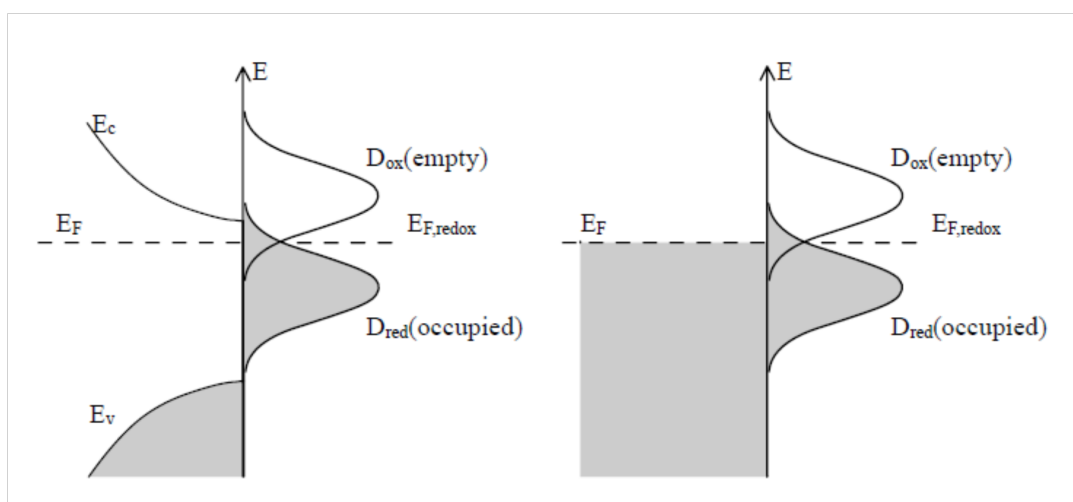


Figure B.1: Distribution of energy states in semiconductor (left) and metal (right)-electrolyte interface. The overlap between filled and empty states on two sides determines the reaction rate.

B.2 The Gerischer Model

Gerischer described the electron transfer (ET) in terms of energy levels of filled and empty states in electrode and liquid. In a redox system, occupied and empty states are interpreted as reduced and oxidized species respectively. The Gaussian distribution function of the states that

was explained above can be described by

$$W_{ox} = W_0 \cdot \exp\left[-\frac{(E - E_{F,redox}^0 + \lambda)^2}{4kT\lambda}\right] \quad (\text{B.2})$$

$$W_{red} = W_0 \cdot \exp\left[-\frac{(E - E_{F,redox}^0 - \lambda)^2}{4kT\lambda}\right] \quad (\text{B.3})$$

where W is the distribution function, λ is the reorganization energy, T is the temperature, k is the Boltzmann constant and W_0 is the normalization factor and is calculated to be

$$W_0 = (4kT\lambda)^{-1/2}.$$

The half width of the distribution, $\Delta E_{1/2}$ is equal $0.53\lambda^{1/2}eV$. A typical value for $\Delta E_{1/2}$ is about 0.5 eV considering a reorganization energy of 1 eV [90, 91]. In order to get the actual density of states in the system, one need to include the concentration of reduced (c_{red}) and oxidized species (c_{ox}) as well. The total distribution is given by

$$D_{ox}(E) = c_{ox}W_{ox} \quad \text{and} \quad D_{red}(E) = c_{red}W_{red} \quad (\text{B.4})$$

The electron transfer rate is determined by the density of states on both sides e.g., for conduction band, the cathodic current, it is given by

$$j_c^- = ek \int_{E_c}^{\infty} f(E)\rho(E)c_{ox}W_{ox}(E)dE = \frac{ekc_{ox}}{(4kT\lambda)^{1/2}} \int_{E_c}^{\infty} n_s \exp\left[-\frac{(E - E_{F,redox}^0 + \lambda)^2}{4kT\lambda}\right]dE. \quad (\text{B.5})$$

in which the $f(E)\rho(E)$ term is the distribution of occupied states in the semiconductor and is replaced by density of carriers at surface, $n_s(E)$, in the right hand side. Since having a considerable density of states on both sides of the interface is essential for having current, most of the electron transfer happens at the band where the overlap of two distribution occurs (depending on the band locations and redox Fermi level, ET can happen via conduction or

valence band, both or neither of them). Since the redox distribution function has a exponential dependency on E^2 , most of the times the overlap between energy states of two sides of the interface is limited to a small energy range around band edges (C.A. 1 kt). One can approximate the integral of Equation B.5 by its linear approximation using $dE = 1 kT$ as below

$$j_c^- \simeq ek_0 n_s \exp\left[-\frac{(E_c^s - E_{F,redox}^0 + \lambda)^2}{4kT\lambda}\right], \quad (B.6)$$

where n_s can be described by Boltzmann distribution function as $n_s = n_0 \exp(-\frac{eV_{sc}}{kT})$ and k_0 is accumulative of all the other terms on the left side of the integral in Equation (B.5). Since the applied potential entirely drops on space charge region, cathodic current is exponentially dependent on applied potential via n_s .

Electron transfer from filled states of redox system (reductants) to semiconductor's conduction band leads to an anodic current of

$$j_c^+ \simeq ek_0(1 - f(E_c))\rho(E = E_c)c_{red} \exp\left[-\frac{(E_c^s - E_{F,redox}^0 - \lambda)^2}{4kT\lambda}\right], \quad (B.7)$$

where the density of states in the semiconductor at the edge of conduction band $\rho(E - E_c)$, is equal to N_c and since most of the states are empty in conduction band, $(1 - f) \simeq 1$. Therefore the anodic current can be simplified to

$$j_c^+ \simeq ek_0 N_c c_{red} \exp\left[-\frac{(E_c^s - E_{F,redox}^0 - \lambda)^2}{4kT\lambda}\right]. \quad (B.8)$$

The equation can be simplified even more by collecting all the constant terms in above equation and the potential independent exponential term in one rate constant,

$$j_c^- = ek_c^- n_s c_{ox} \quad \text{where} \quad k_c^- = k_{c,max}^- \exp\left[-\frac{(E_c^s - E_{F,redox}^0 + \lambda)^2}{4kT\lambda}\right], \quad (B.9)$$

$$j_c^+ = ek_c^+ N_c c_{red} \quad \text{where} \quad k_c^+ = k_{c,max}^+ \exp\left[-\frac{(E_c^s - E_{F,redox}^0 - \lambda)^2}{4kT\lambda}\right]. \quad (B.10)$$

Similarly, electron transfer at valence band can be described as below

$$j_v^- = ek_v^- N_v c_{ox} \text{ where } k_v^- = k_{v,max}^- \exp\left[-\frac{(E_v^s - E_{F,redox}^0 + \lambda)^2}{4kT\lambda}\right] \quad (\text{B.11})$$

$$j_v^+ = ek_v^+ p_s c_{red} \text{ where } k_v^+ = k_{v,max}^+ \exp\left[-\frac{(E_v^s - E_{F,redox}^0 - \lambda)^2}{4kT\lambda}\right]. \quad (\text{B.12})$$

Measurements of space charge capacity of several semiconductor electrodes in aqueous solutions indicates that position of band edges at the surface of a semiconductor are usually constant even for samples with different doping densities. The band edges also stay pinned after addition of redox system due to stronger interaction with water than redox. This pinned location results the potential independent rate constants of equations B.9 to B.12 be intrinsic features of each semiconductor-redox pair that do not change with secondary factors such as concentration or charged state. Therefore, large and small ET rates is expected based on relative position of band edges and redox potential. Finding semiconductors that have much larger rate constant with only one of the redox couples in a PGC could be a solution to the selectivity challenge in PGCs.

B.3 Experimental Measurement of the Selectivity

The hypothesis is tested in a series of experiments on fluorine doped tin oxide (FTO), copper(II) oxide (CuO) and nickel oxide (NiO) as wide band gap semiconducting electrodes [49]. Methyl viologen (MV^{2+}/MV^+), ferrocyanide ($Fe(CN)_6^{3-}/Fe(CN)_6^{4-}$) and ferrous (Fe^{3+}/Fe^{2+}) are used as the reacting redox couples. The former has standard redox potential close to FTO conduction band edge and the latter has standard potential close to CuO valence band edge.

Sampled current voltammetry is used to measure the electron transfer rate between semiconducting electrodes and redox couples. Negative overpotentials of different values are applied to the electrode and the transient current is monitored. The measure current value after 12 seconds is saved as the current response to that overpotential. The reason for the delay is to avoid the double-layer capacitance charging and to only compare the Faradaic response. The

best selectivity is observed with the FTO electrode. Figure B.2 shows the cyclic voltammetry and sampled electron voltammetry results for this electrode.

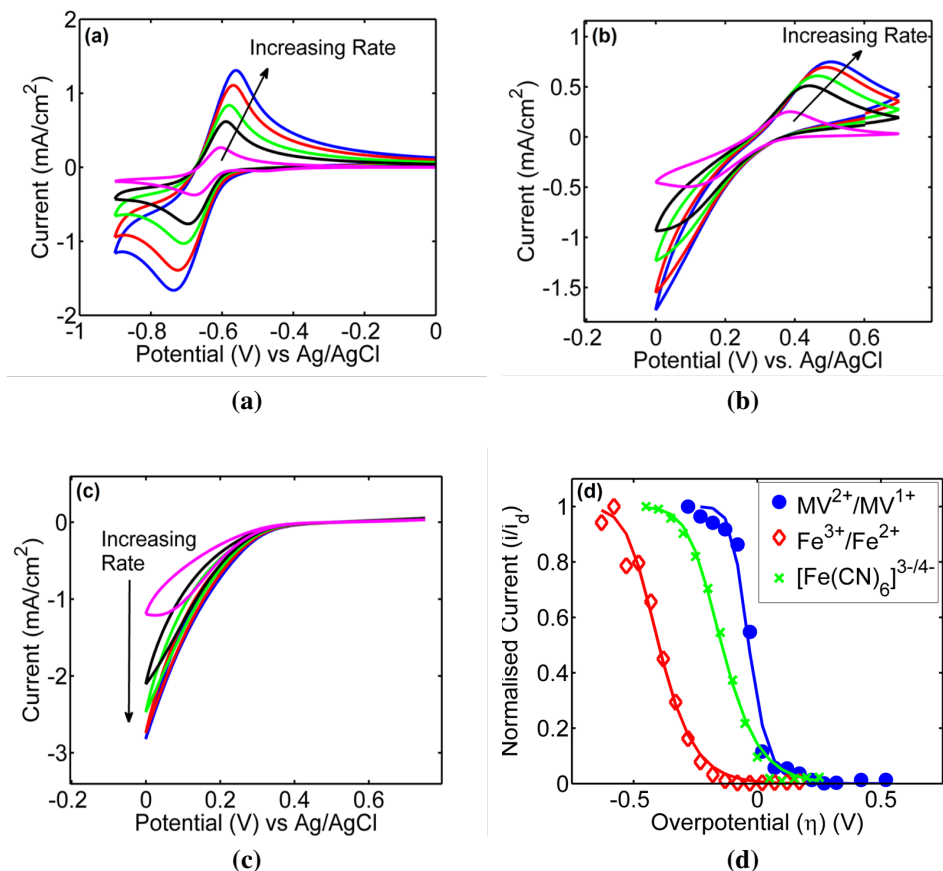


Figure B.2: Cyclic voltammetry of (a) methyl viologen (b) ferri/ferrocyanide and (c) ferric/ferrous on FTO electrode. (d) Sampled current voltammetry data measured at 12 s after the voltage application. The concentrations are 10 mM in aqueous 1 M KCl. The CVs are measured at 300, 200, 100, 50 and 10 mV s⁻¹.

The cyclic voltammograms indicate that while methyl viologen has quasi-reversible kinetics on the FTO electrode, ferricyanide/ferrocyanide only shows onsets of cathodic peaks for extremely slow scan rates with clear anodic peaks for all scan rates. This reflects the faster reaction rate of methyl viologen compared to ferricyanide/ferrocyanide. The absence of the anodic and cathodic peaks in the ferric/ferrous couple CVs shows a very slow kinetic rate of this ion on FTO.

The reaction rates are derived by mapping the sampled current voltammetry data of Fig-

ure B.2d to a quasi reversible reaction model. Two orders of magnitude difference in rate constants are observed due to the relative locations of semiconductor band edge and the redox standard potential as shown in Table B.1.

Table B.1: Standard heterogeneous rate constants of redox couples on FTO. E^o is the redox standard potential, k_o is the reaction rate constant and R^2 represents the fit quality.

Mediator	E^o (V vs Ag/AgCl)	$E_c - E^o$ (V)	k_o (cm s ⁻¹)	R^2
(MV ₂ ⁺ /MV ⁺)	-0.62	-0.18	2.8×10^{-4}	0.9895
Fe(CN) ₆ ³⁻ /Fe(CN) ₆ ⁴⁻	0.25	0.65	1.4×10^{-4}	0.9953
(Fe ³⁺ /Fe ²⁺)	0.48	1.08	5.7×10^{-6}	0.9906

It is important to note that any significant selectivity occurs only at large differences in standard potentials (~ 1 V). This effect is predictable from Gerischer model as well since the reorganization energy of the species is in the same order (~ 1 eV). Therefore, any use of semiconductor selectivity is only applicable for dye/mediator pairs of large standard potential separation. All in all, this study demonstrates the eligibility of semiconductor electrodes for selective action in photogalvanic cells.

Appendix C

Solar Redox Battery Cost Analysis

The integration of solar cell and battery has significant effects on manufacturing and operating cost of the utilization of the solar energy. While it is understood that system level alterations in RFBs might be required after the integration, an analysis based on modifications limited to the energy conversion modules is presented in this chapter. The effect of system scaling is shown by calculating system cost for three system sizes. These three segments are defined as residential(10 kW/100 kWh), industrial (100 kW/1 MWh) and grid backup (1 MW/10 MWh) based on average energy and power ratings in each category [92].

Based on current date expenses of Vanadium RFBs (the most expensive yet reliable RFB technology) and Li-ion batteries, the cost of integrated and separate solar cell batteries are compared in Table C.1. The energy storage cost for these scenarios are extracted from a recent report by Sandia National Laboratories based on vendors input [8].

The first two rows reflects the three energy storage scale scenarios. The energy storage cost is shown in row 3. RFB shows significant cost advantage over LIB in larger scales and almost on par performance in residential scale applications. Next, the cost of solar panel installation equal to the power rating of each sector is added. DSSC cost breakdown is reported by Hashmi *et al.* [93]. They reported that the encapsulation and counter electrode adds up to half of the solar cell cost. These elements are shared with the RFB therefore the total cost is estimated to

Table C.1: Comparison of energy conversion and storage costs for combined and separated systems.

1	Energy rating	100 kWh	1 MWh	10 MWh	
2	Application	Residential	Industrial	Grid Connected	
3	Capital cost \$ / kWh	Li-ion Battery	1000	900	800 ^a
		Redox Flow	1000	800	600
4	Average power consumption	10 kW	100 kW	1 MW	
5	Total Cost of solar panels (\$)	Separate (3,2.5,2 \$/W)	30 k	250 k	2 M
		Integrated (1 \$/W)	10 k	100 k	1 M
6	Cost of solar panels (\$/kWh of power plant)	Separate	300	250	200
		Integrated	100	100	100
7	Cost of complete solution (\$/kWh)	Li-ion + PV	1300	1150	1000
		Integrated RFB	1100	900	700

^a Projected value.

be the cost of RFB plus the cost of the remaining elements of a DSSC. As a result the added cost is 1 \$/W as opposed to 2 \$/W of a complete solar cell (row 5). The normalized cost of the solar panels to the energy rating of the facility is shown in row 6. Overall, an integrated solar redox battery shows an economic advantage relative to Li-ion storage at all application scales as is seen in row 7.

It can be seen that because of the high cost of electrochemical energy storage in general, 2/3 of the cost advantage relative to Li-ion is because of the storage unit, *i.e.*, RFB, rather than the integration. In other words, 200 dollars in cost savings relative to Li-ion battery is thanks to the use of redox flow system and a further 100 dollars comes from the sharing of parts with the solar cell bringing the total cost of an integrated 10 MWh harvesting and storage system to 700 \$/kWh. With further price drop to batteries, the share of the latter section is expected to increase. Some further cost saving is possible because of the elimination of the DC-DC converter and the maximum power tracker between solar cell and the battery. It is noteworthy that the design requirements of an integrated system might change these values and a more accurate estimate requires a finalized design and implementation of the solar redox facility.